AD-A133 679 NON-LTE RADIATION FROM AN ARGON SEEDED MICROBALLOON IMPLOSION II(U) NAVAL RESEARCH LAB WASHINGTON DC P C KEPPLE ET AL. 15 SEP 83 NRL-MR-5182 SBI-AD-E000 547 1/1

UNCLASSIFIED DE-AI08-79-DT-40092 F/G 20/9 NL

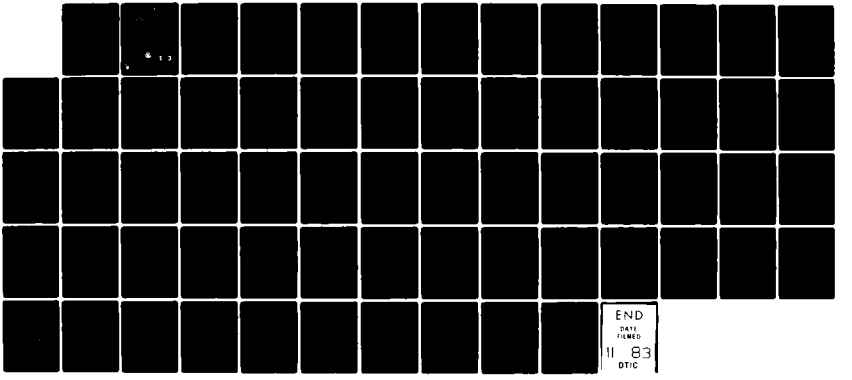

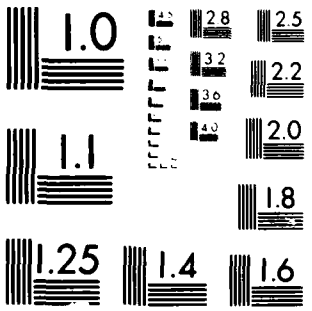


MICROCOPY RESOLUTION TEST CHART
NATIONAL BUREAU OF STANDARDS-1963-A

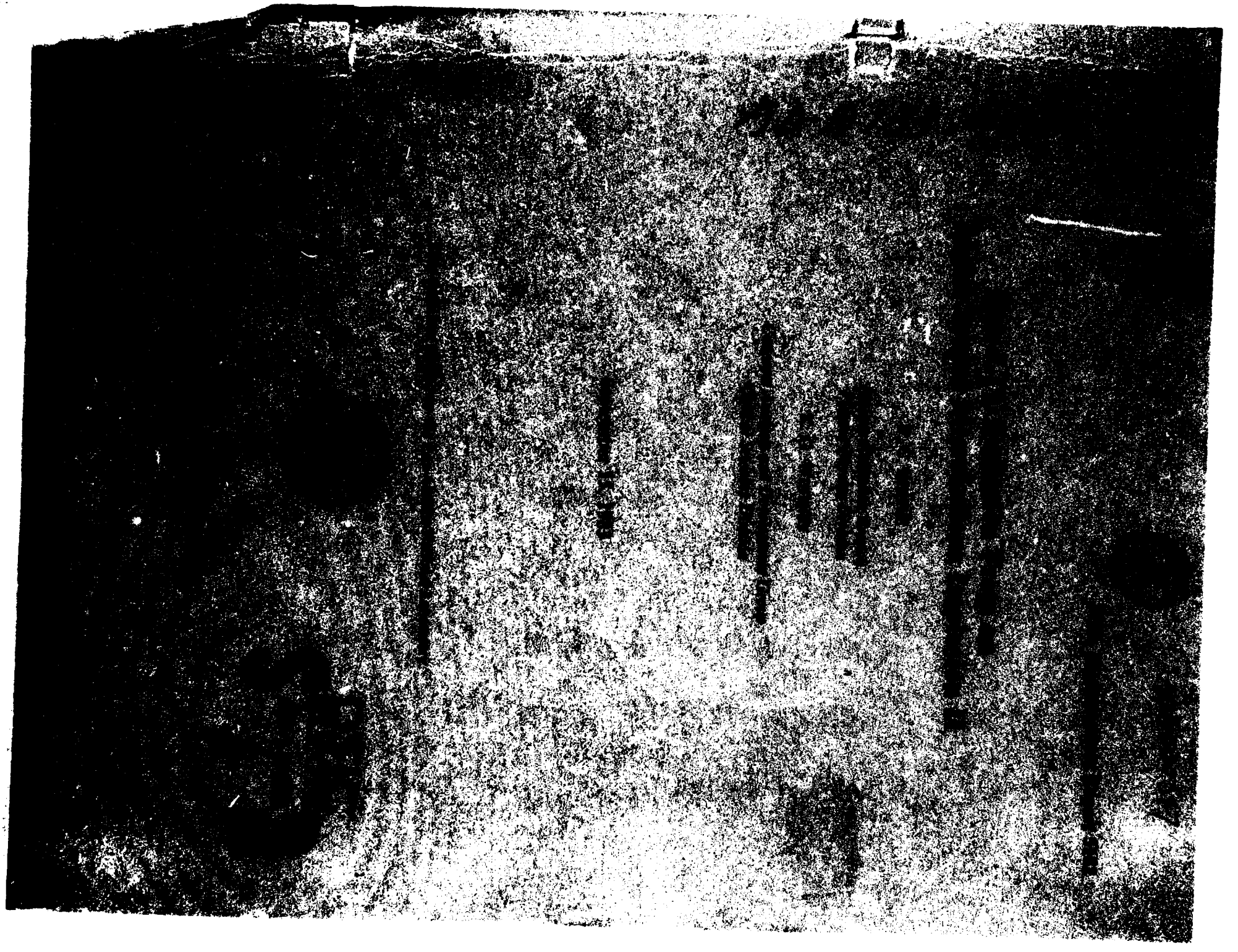

SECURITY CLASSIFICATION OF THIS PAGE (When Data Entered)

| REPORT DOCUMENTATION PAGE | READ INSTRUCTIONS BEFORE COMPLETING FORM |
|---|---|
| 1. REPORT NUMBER: NRL Memorandum Report 5182 | 2. GOVT ACCESSION NO.: AD-A133679 |
| 3. RECIPIENT'S CATALOG NUMBER | |
| 4. TITLE (and Subtitle): NON-LTE RADIATION FROM AN ARGON SEEDED MICROBALLOON IMPLOSION II | 5. TYPE OF REPORT & PERIOD COVERED: Final report |
| 6. PERFORMING ORG. REPORT NUMBER | |
| 7. AUTHOR(s): P. C. Kepple and K. G. Whitney | 8. CONTRACT OR GRANT NUMBER(s) |
| 9. PERFORMING ORGANIZATION NAME AND ADDRESS: Naval Research Laboratory, Washington, DC 20375 | 10. PROGRAM ELEMENT, PROJECT, TASK AREA & WORK UNIT NUMBERS: DE-AI08-79-DT-40092; Mod. No. A006; 47-0858-0-2 |
| 11. CONTROLLING OFFICE NAME AND ADDRESS: Los Alamos National Laboratory, Los Alamos, New Mexico 87545 | 12. REPORT DATE: September 15, 1983 |
| | 13. NUMBER OF PAGES: 63 |
| 14. MONITORING AGENCY NAME & ADDRESS(if different from Controlling Office) | 15. SECURITY CLASS. (of this report): UNCLASSIFIED |
| | 15a. DECLASSIFICATION/DOWNGRADING SCHEDULE |

16. DISTRIBUTION STATEMENT (of this Report)

Approved for public release; distribution unlimited.

17. DISTRIBUTION STATEMENT (of the abstract entered in Block 20, if different from Report)

18. SUPPLEMENTARY NOTES

This work was funded by the Los Alamos National Laboratory.

19. KEY WORDS (Continue on reverse side if necessary and identify by block number)

Stark broadening
Non-LTE radiation
Microballoon implosions

20. ABSTRACT (Continue on reverse side if necessary and identify by block number)

The results of three LASNEX simulations of Argon seeded DT filled microballoon implosions in which the details of the hot electron preheat have been varied are post analyzed with a full collisional radiative model. The resulting simulated spectra are compared. A similar calculation is performed on a pure argon microballoon implosion. Some features of the average atom model used by LASNEX are compared to those calculated by the collisional radiative model.

DD FORM 1 JAN 73 1473 EDITION OF 1 NOV 65 IS OBSOLETE
S/N 0102-014-6601

SECURITY CLASSIFICATION OF THIS PAGE (When Data Entered)

Contents


I. Introduction..... 1

II. Argon/DT Post-Analysis..... 2

III. Excitation/Ionization Comparisons..... 5

IV. Pure Argon Post-Analysis..... 7

V. Summary and Conclusions..... 8

VI. Acknowledgments..... 9



DTIC
SELECTE
OCT 1 3 1983
B

Accession For
NTIS GRA&I
DTIC TAB
Unannounced
Justification
By
Distribution/
Availability Codes
Dist | Avail and/or Special
A




PRECEDING PAGE BLANK-NOT FILMED

# NON-LTE RADIATION FROM AN ARGON SEEDED MICROBALLOON IMPLOSION II

## I. INTRODUCTION

In a previous NRL Memorandum Report Number 4565[1], a physics program to predict the K-shell spectral output from $CO_2$ driven, argon/DT filled microballoons was described. LASNEX hydrodynamics data giving the Lagrangian coordinates, temperature, density, and charge state of the argon/DT region were used as input to a detailed collisional-radiative (CR) model of argon. This model was used in conjunction with a set of 8 Stark profiles that could be calculated as functions of temperature and density for the $L_\alpha$, $L_\beta$, $L_\gamma$, and $L_\delta$ - like lines in Ar XVII and Ar XVIII. One objective of the program this year was to determine how accurately the experimental line spectra obtained in a number of argon/DT microballoon experiments at Los Alamos National Laboratory could be replicated. In the process, several issues had to be addressed. For example, improvements were made in the Stark profile calculations to include effects such as fine structure, ion motion, and electron cloud correlations. The effect of different implosion dynamics, due to different amounts of suprathermal electron preheat, on the computed spectrum and calorimetry was investigated. Diagnostic problems in using time integrated spectra to infer plasma conditions were also explored through the comparison of power spectra at the times of peak temperature, density, and emission against the time integrated spectra. Some further comparisons of the average ion method used in LASNEX with the results of the CR calculations were also made. Finally, a post-analysis of a microballoon implosion containing 47 ngm of a pure argon fill was carried out in order to illustrate the large contrasts in ionization and emission behavior that are expected to occur between pure and mixed argon fill cases.

The main purpose of this final report is to present the results of the argon K-series emission spectrum calculations obtained by analyzing three LASNEX tapes that are labeled NRL 21, 22, and 23 respectively in all of the following figures. It is our understanding that the differences in the three LASNEX simulations are primarily due to different assumptions on hot electron production and resulting fuel pre-heat. In all cases, however, it is assumed that the hot electrons have been thermalized (at least in the fuel region) by the time the CRE simulation is begun. The report is divided into three parts. In the first part, identical sets of results

Manuscript approved July 11, 1983.

that are derived from processing the three tapes over the same time interval are presented. The time interval was chosen to overlap with all three emission pulses encompassing the line spectrum of interest, in the 3.0 keV to 4.1 keV region. In the second part, some comparisons of average ion with the CR population and electron densities are made. In the third part we present some preliminary calculations based on a LASNEX simulation of an implosion of a microballoon filled with pure argon.

Since we are only trying to synthesize the K-shell spectrum, the CRE model has structure (excited states) only in the hydrogen-like, helium-like and lithium-like stages of the argon ions. The structure is indicated in Figure 1. Note that there are excited states up to n=10 in the hydrogen-like and helium-like stages and up to n=6 in the lithium-like stage. The five doubly excited states were not adequate, as yet, to calculate the satellites to H-$L_\alpha$ and He-$L_\alpha$, in the CR model used; thus, they were ignored in these calculations.

## II. Argon/DT Post-Analysis

A visualization of the implosion dynamics in the argon/DT region, which consisted of 11 hydrodynamic cells, can be obtained from graphs of each of these cell's radius, electron temperature, and argon ion density as a function of time. The radii of the 11 cells used in the calculations are plotted in Figs. 2, 12, and 22 for NRL 21, NRL 22, and NRL 23 respectively. The electron temperatures are shown in Figs. 3, 13 and 23. The cell radii, the electron temperature, the electron density, and Z, which is the average charge state in each cell, are direct outputs of the LASNEX simulation. From these quantities the argon ion density is calculated from

$$N_{AR} = N_e / [(2\alpha + 1)]$$

where $\alpha = 50$ is the (molecular) ratio of DT to argon in the microballoon. The argon number density is shown in Figs. 4, 14 and 24.

To verify that the time from 0.55 to 1.2 nsec contains all the K-shell radiation, we plot the total of all line plus continuum radiation as predicted by the CRE model using the structure of Fig. 1. These results as well as the contribution in various spectral bands that sum up to the total

emission are plotted in Figs. 6, 16 and 26. One can clearly see that the K-shell emission ($h\nu > 3KeV$) is well bounded by these times. These implosion and calorimetry figures show that implosions NRL 21 and NRL 22 are quite similar, but that time resolved calorimeter measurements could distinquish the important difference in timing of the NRL 23 implosion from NRL 21 and 22.

The opacity of a line depends on the line profile. The first four resonance line profiles of the hydrogen-and helium-like stages are obtained from detailed Stark profiles calculations. The profiles of all other lines are approximated by Voigt profiles. In addition to the Stark profile the H-$L_\alpha$ and He-$L_\alpha$ lines were convolved with a Gaussian whose width is the sum of the Doppler and an equivalent ion dynamic width[2], and in the case of H-$L_\alpha$ includes the fine structure splitting.* The other Stark profiles should be convolved with similar Doppler Gaussians, but the lines are so wide that the convolution adds or modifies little. The total opacity at line center of the H-$L_\alpha$ and He-$L_\alpha$ lines is shown on Figs. 5, 15 and 25. It is evident that opacity is significant for the two resonance lines, H-$L_\alpha$ and He-$L_\alpha$. Thus we see from these figures that opacity will play an important role in determining both the degree of CRE excitation in the argon, and the shape of its K-series emission spectrum.

A common feature of each of these LASNEX simulations is that the time of "peak temperature"** precede the time of "peak compression". Although emission is a nonlinear function of both temperature and density, it follows that the time of peak emission falls between that of peak temperature and density. We have made plots of the instantaneously emitted

* Adding a fine structure contribution to the width of a line as a Gaussian convolution is acceptable if there is some other source of broadening that is larger than the fine structure splitting in order to remove the details of the fine structure from the composite profiles. In the case of H-$L_\alpha$, only the source broadening is large enough to justify this convolution treatment.

**All of the LASNEX simulations show a shock penetrating the plasma well before the time of the main compression. The temperature associated with this shock sometimes exceeds that of the main compression, however the density at this early time is so low that there is little radiation generated by this early shock. Thus we pick the second or main heating pulse as the "peak temperature".

power spectra at the times of peak temperature, peak emission and peak compression in each of the three cases. These are shown in Figs. 7-9, 17-19 and 27-29. In addition we have calculated the time integrated spectra which are shown in Figs. 10, 20 and 30. For comparison we have plotted, in Figs. 11, 21 and 31, the time integrated spectrum without the source broadening. Comparing the time integrated spectra without instrumental and source broadening (Figs. 11, 21 and 31) to the corresponding broadened spectra (Figs. 10, 20 and 30) one can see that extremely narrow and intense intercombination line has been lowered (widened out) to a degree which makes it look much more normal when compared to the He-$L_\alpha$ line. One further notes that the detailed structure of the Stark profiles of He-$L_\beta$, $L_\gamma$, and $L_\delta$ and of the H-$L_\beta$ have been completely smeared out.

The spectral plots are scaled such that if one ignores the numbers along the ordinate they can be interpreted as relative intensity plots. If one overlays Figs. 10 and 20, one finds that the helium-like lines match surprisingly well while a small difference in the hydrogen-like lines is evident. Since the hydrogen-like lines on NRL 22 are stronger one can say 22 is a hotter implosion than 21. (It would be more correct to state that the temperature and density profiles overlap more on one shot than another rather than call one hotter than the other.) Comparison of the scale on the ordinate confirms this conclusion. Overlaying Figs. 20 and 30 (i.e. NRL 22 and 23) is even more interesting since now an interpretation as relative intensities reveals no significant difference yet the scale on the ordinate shows that 22 radiates almost 80% more than NRL 23. Since the line ratios are approximately the same it follows that calorimetry must be used to distinguish the implosions, i.e. Absolute measures of the line intensities and time resolved measures of the emission pulse width and peak.

A density diagnostic is provided by the comparison of Stark widths. The opacity of He-$L_\alpha$, the fine structure splitting of H-$L_\alpha$, the overlap of H-$L_\beta$ and He-$L_\delta$ all render these lines undesirable as density diagnostics. The He-$L_\beta$ and $L_\gamma$ remain as candidates with $L_\beta$ being preferable since it has no unshifted component and it is generally a strong line in the spectrum. If one compares the width (full width at half intensity) of the He $L_\beta$ on Figs. 8, 9 and 10 one finds that the width at time of peak compression is about 33% larger than at peak emission or than in the time

integrated spectrum. Thus a density determination from time integrated spectra would underestimate the true peak density by about 20%. Similar conclusions would be reached from analysis of NRL 22 or NRL 23. This discrepency is a general feature of implosions with a significant time difference between the temperature and density maxima.

A broadband spectrum from NRL 23 is plotted in Fig. 32. On the same figure the blackbody spectrum for a plasma at the temperature of the outside cell is also plotted. Except for some of the lines, the actual spectrum is several orders of magnitude below the blackbody.

## III. Excitation/Ionization Comparisons

In NRL Memorandum Report 4565[1] we calculated the n=1 (n=2) occupation in CRE as a function of time in the implosion; that is, the mean number of bound electrons per nucleus with principal quantum number = 1 (2). The details of the transformation from the CRE microstate populations to the average atom (AA) macro-occupation used in the LASNEX calculation was given in that report, and will not be repeated here. The important point is that a comparison of n=1 and n=2 occupation numbers derived from the CRE results to those calculated by the LASNEX AA subroutine showed some important differences. Was that an isolated case or are such differences typical? To address this question we again calculated the CRE n=1 and n=2 occupation numbers for the NRL 21, 22 and 23 LASNEX simulations and plotted the results along with those obtained from the LASNEX calculation. These are shown in Figs. 33-38. For the n=1 case differences in excess of 30% persist. While for n=2, even larger differences persist.

Further evidence of differences are provided by Figs. 39-41 where a comparison of electron densities (due to the argon ionization) as calculated by the AA and CRE methods are shown.

The quantity plotted is

$$\frac{100\ |n_e(AA) - n_e(CRE)|}{n_e(CRE) - 2\alpha\, n_i}$$

The most striking feature of these plots is that the difference in electron density grows systematically with time. One further notes that the difference is largest in the outside cell. The outside cell is the

coolest, has the highest density, and since it has a photon flux only from one side, it is also the cell most affected by the asymmetric nature of the radiative energy intensity pattern.

To check the CRE calculation for convergence we made a well converged calculation starting rather late in the implosion and taking a large number very small time steps. The electron density and population results were identical to those of the full calculation, from which we conclude that the CRE calculation was essentially free from (lack of) convergence problems. The LASNEX calculation are time dependent while the CRE assumes adiabatically changing steady states. Since the difference is largest for the outside cell, which, as we already noted, is coolest, then recombination processes are dominant. The ground state 3-body recombination coefficients for H → He, He → Li, Li → Be and Be → B are all of the order of $10^{-37}$. Thus

$$\frac{dN_i}{dt} \simeq N_i \, n_e^{\,2} \, 10^{-37} \, f_c \quad \text{or}$$

$$\tilde{\tau} \approx \frac{N_i}{\frac{dN_i}{dt}} = \frac{f_c}{n_e^{\,2} \, 10^{-37}}$$

and since $n_e \sim 3 \times 20^{23}$, $\tilde{\tau} \approx 10^{-10} \, f_c$ sec., where $f_c$ is a factor that describes the relative importance of direct to cascade (through excited states) recombination processes. For these implosions, $f_c \approx 10^{-2}$; that is, the population density in any one of these ionization stages e-folds in 1 psec. Examination of these number densities show that for times up to a nanosecond in the implosions the ground state number densities in the outside cell do not change faster than this time scale, thus for times up to a nanosecond no large error has been committed by invoking the steady state approximation. Even after 1 nsec the error is not apt to be as large as the differences shown in Fig. 39-41. We note that the CRE model was developed to study K-shell radiation. Thus, as we have already stated, the model has structure only in the hydrogen, helium, and lithium-like stages. It follows that the model is accurate only over a limited temperature range, which is itself density dependent, i.e., when L-shell occupation below lithium-like argon is negligible.

## IV. Pure Argon Post-Analysis

In this section we present the results of some preliminary calculations on a pure argon filled microballoon implosion containing 47 ngm of argon. Since there is no DT $\alpha$ (the DT to argon ratio) is zero. By comparing Fig. 44 to Fig. 24 we see that the peak ion density of the pure argon implosion is comparable to the peak total ion density of NRL 23. Comparing Figs. 42 and 44 to 22 and 24 one can see that the pure argon implosion arrived at peak density a bit sooner and stayed near peak density longer than the argon + DT (NRL 23) case. A first glance at Fig. 43 would indicate that the pure argon implosion achieves a peak temperature comparable to that of the argon + DT (NRL 23), however, when Fig. 43 is overlaid on Fig. 44 one sees that the peak temperature occured so early in the implosion that the density at that time was quite low. Thus the effective peak temperature of the pure argon implosion is seen to be much lower, of the order of 500 eV. This misstiming of the temperature and density maxima will be manifest several times in the discussion of the radiation emitted by the pure argon implosion. The optical depth of several K lines is shown in Fig. 45. The increased number of argon ions results in an increased optical depth, except for that of Ar XVIII late in the implosion. Since the temperature at this time is low the abundance of Ar XVIII is low and thus the optical depth of hydrogen like lines is also low. The radiation emitted in two bands is plotted in Fig. 46. Since the pure argon implosion has more argon ions one would expect it to radiate more than the argon + DT (NRL 23). This expectation is fulfilled in the case of the 1-3 KeV band. On the other hand, it is this prodigious radiation which cools the pure argon plasma and thus insures that (relatively) little radiation is emitted in the 3-4 KeV band. The time integrated spectrum is shown in Fig. 47 while the instantaneous spectrum at the time of true peak temperature is shown in Fig. 48. Note that, for the pure argon calculations, the model has been improved to allow calculation of the satellites to the H-$L_\alpha$ line, and the instrumental and source broadening has been reduced to 4 mA. A comparison of the ground state populations as calculated in CRE and LTE for both pure argon and argon + DT for the conditions in the inner and outer shells are shown in Figs. 49-52. It is clear that LTE is an adequate approximation only late in the implosions.

## V. Summary and Conclusions

The differences in initial and suprathermal dynamic conditions that were used to generate the three LASNEX runs were not made known to us. However, post-analysis of the LASNEX tapes has shown that the implosion dynamics of the argon/DT region for tapes, NRL 21 and NRL 22, are nearly identical; NRL 22 was a slightly hotter, denser compression. The qualitative differences between the NRL 23 compression and NRL 21 and 22 were significantly greater, although a comparison of cell temperature and density trajectories shows that all three implosions reached relatively the same peaks in temperature and densities - the main difference between NRL 23 and NRL 21 and 22 was that the heating and compression process was faster.

Remarkably, when all LASNEX tapes were processed in identically the same way, they all produced qualitatively the same time-integrated line spectrum - the major difference between them was quantitative, i.e. there were important differences in the calorimetry and less strongly in the spectroscopy per se. NRL 22, being the hottest, densest, and a relatively slow compression, produced the most intense K-shell emission. NRL 23, being a rapid compression, produced the narrowest emission pulse and the least intense spectrum. There are in each of the three cases, however, discernible and, no doubt, measurable differences in the H-$L_\alpha$ to He-$L_\alpha$ line ratio. The important conclusion to be drawn in the post-analysis of these cases is that to have meaningful comparisons between LASNEX simulations and experiment, it is necessary to make simultaneous time-resolved, broad and narrow band, calorimetry as well as time-integrated spectral measurements.

Comparisons were also made between the argon electron and ion population densities obtained in the LASNEX calculations and in the detailed CRE calculations. Generally speaking the two calculations agreed fairly well. However, it was noted that the difference between the two computed electron densities tended to grow systematically with time so that this difference was largest at the end of each calculation. The reason for such behavior in the two calculations is not known, although it was

verified in one case, that in the CRE calculation, the ionization state computed in the time evolving calculation at one point late in time could be reproduced in a time independent, well converged snapshot calculation.

## ACKNOWLEDGMENTS

We would like to thank Allan Hauer and Eldon Linnebur for providing the LASNEX simulation data which was analyzed in this report. We would also like to acknowledge many profitable discussions with Hans Griem on the subject of Stark broadening. Last, but certainly not least, we would acknowledge the extensive contributions of J. Davis and Dwight Duston to the collisional model.

This work was supported by the Los Alamos National Laboratory.

## References


1. P. C. Kepple and K. G. Whitney, NRL Memorandum Report 4565 (1981).

2. Hans R. Griem, Milan Blaha and Paul C. Kepple, "Stark-Profile Calculations for Lyman-series Lines of One-Electron Ions in Dense Plasmas", Phys. Rev. A, 19, 2421, 1979.


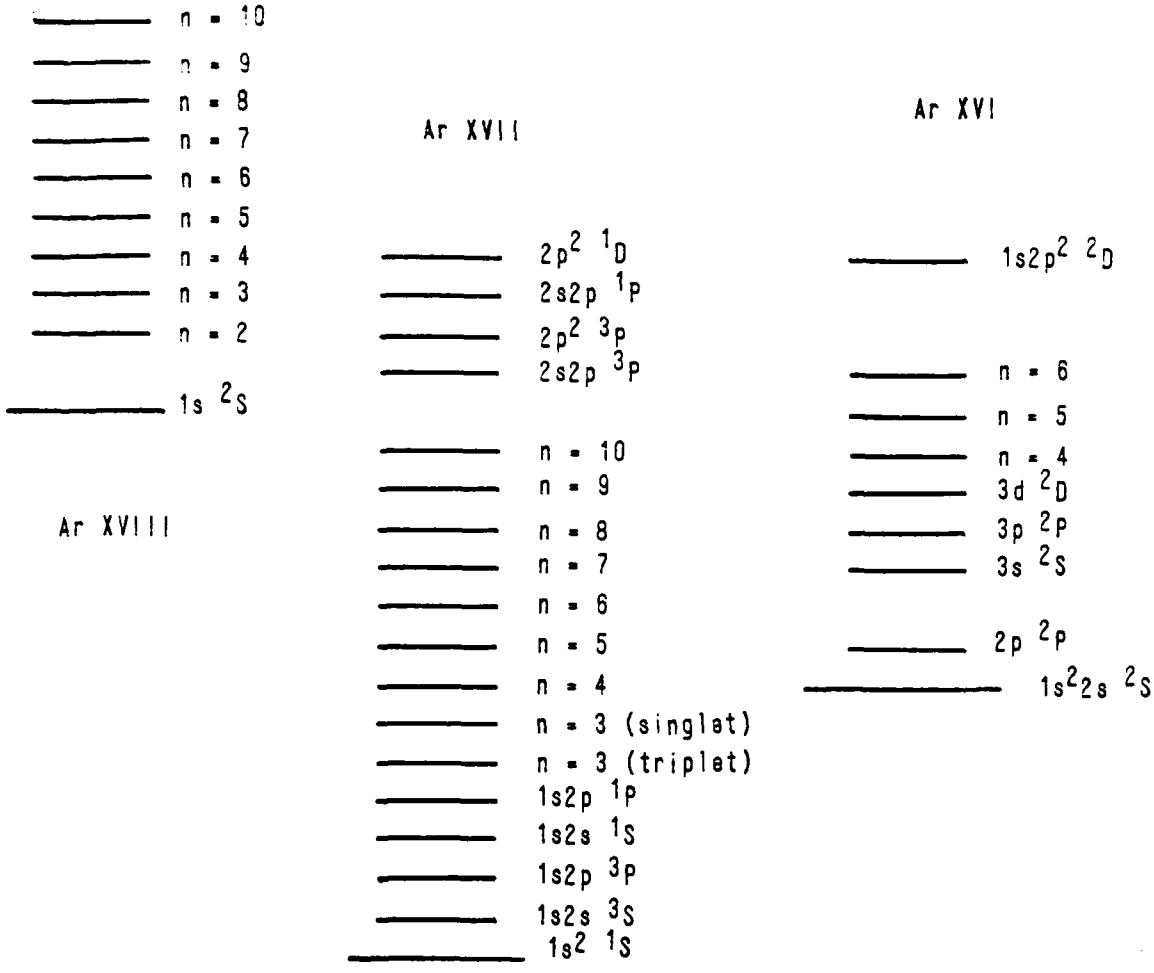


Fig. 1 Energy level diagram for the excited states included in the model.

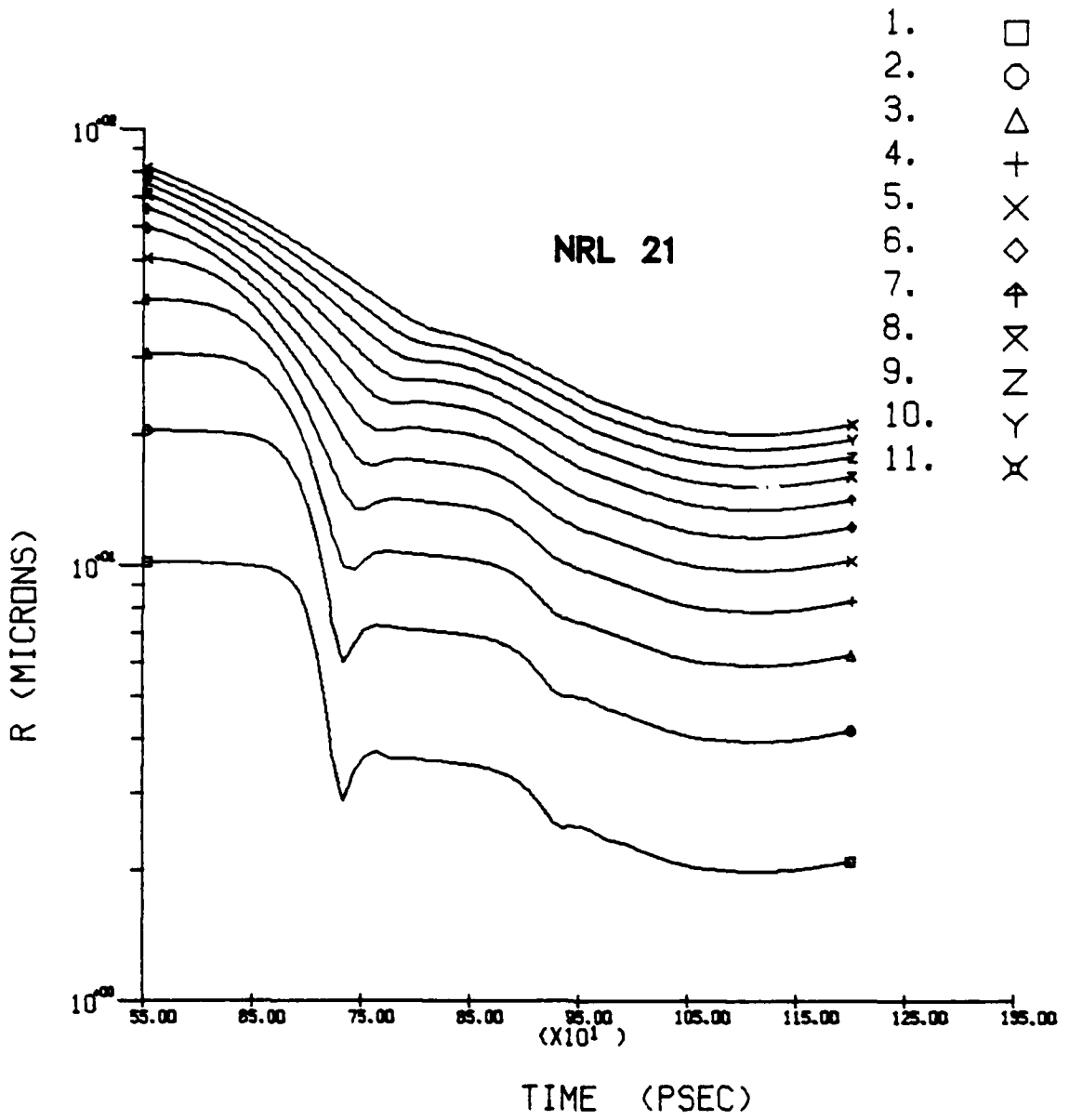


Fig. 2 Radius of cell centers vs time for NRL 21.

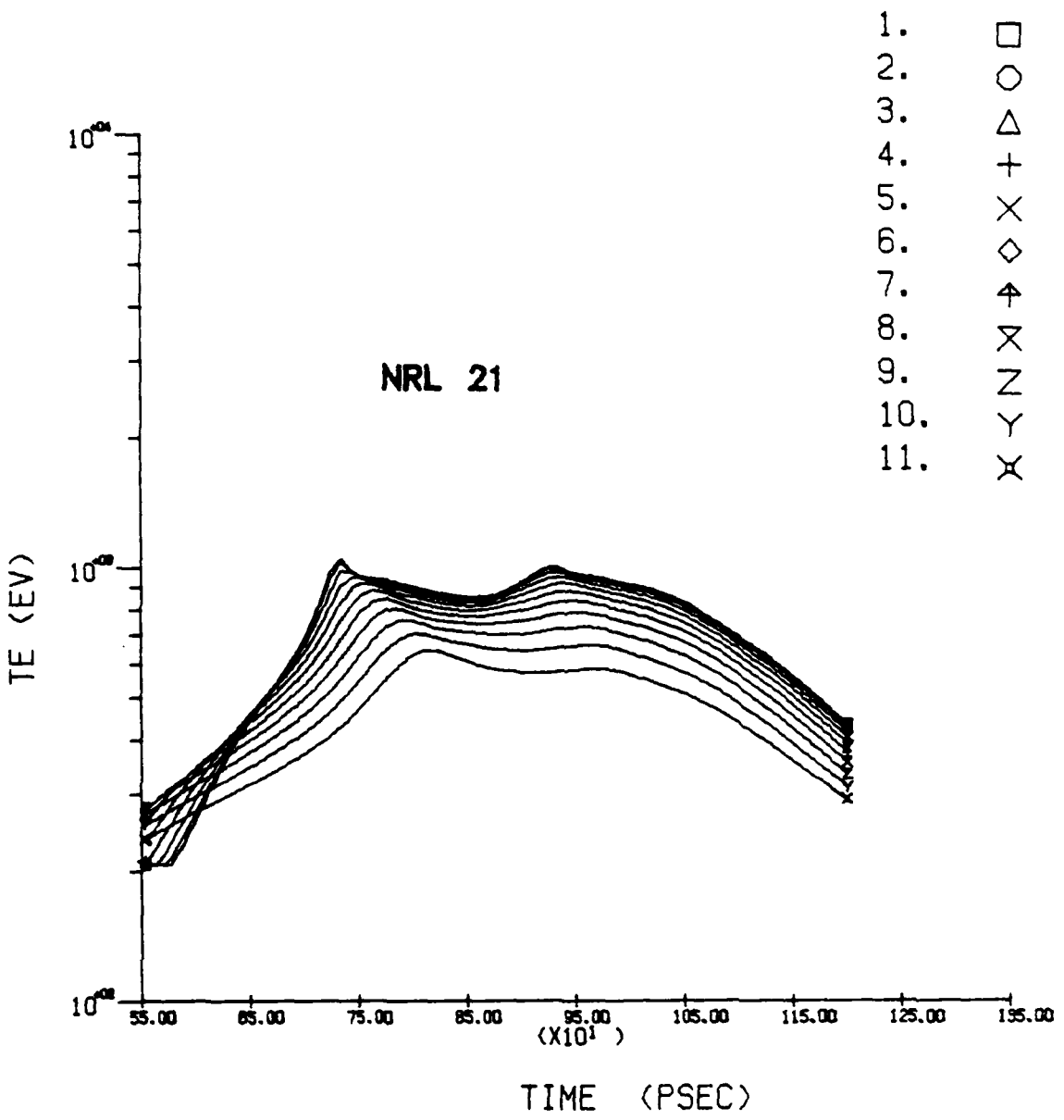


Fig. 3 Electron temperature vs time for NRL 21.

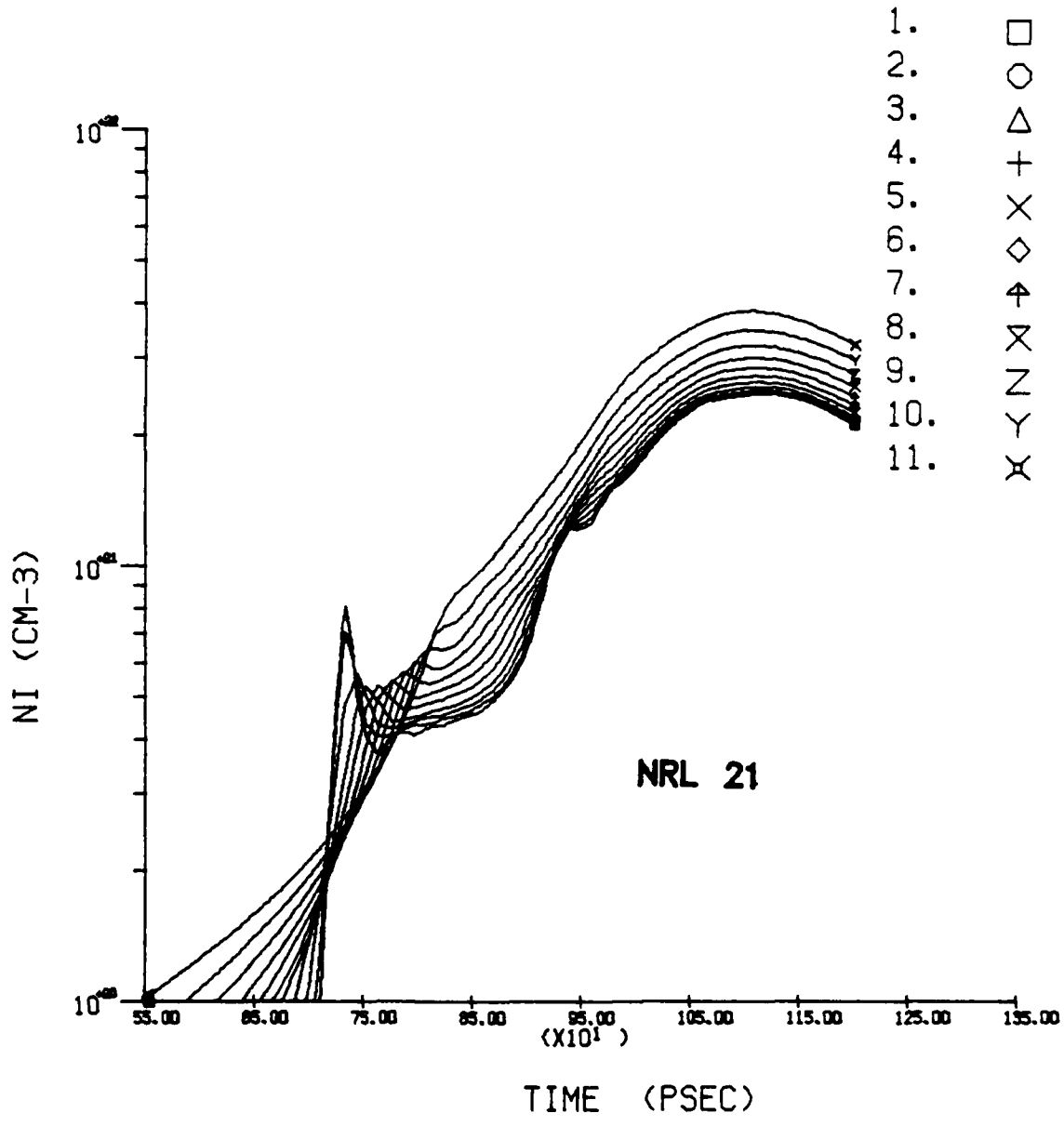


Fig. 4 Argon number density vs time for NRL 21.

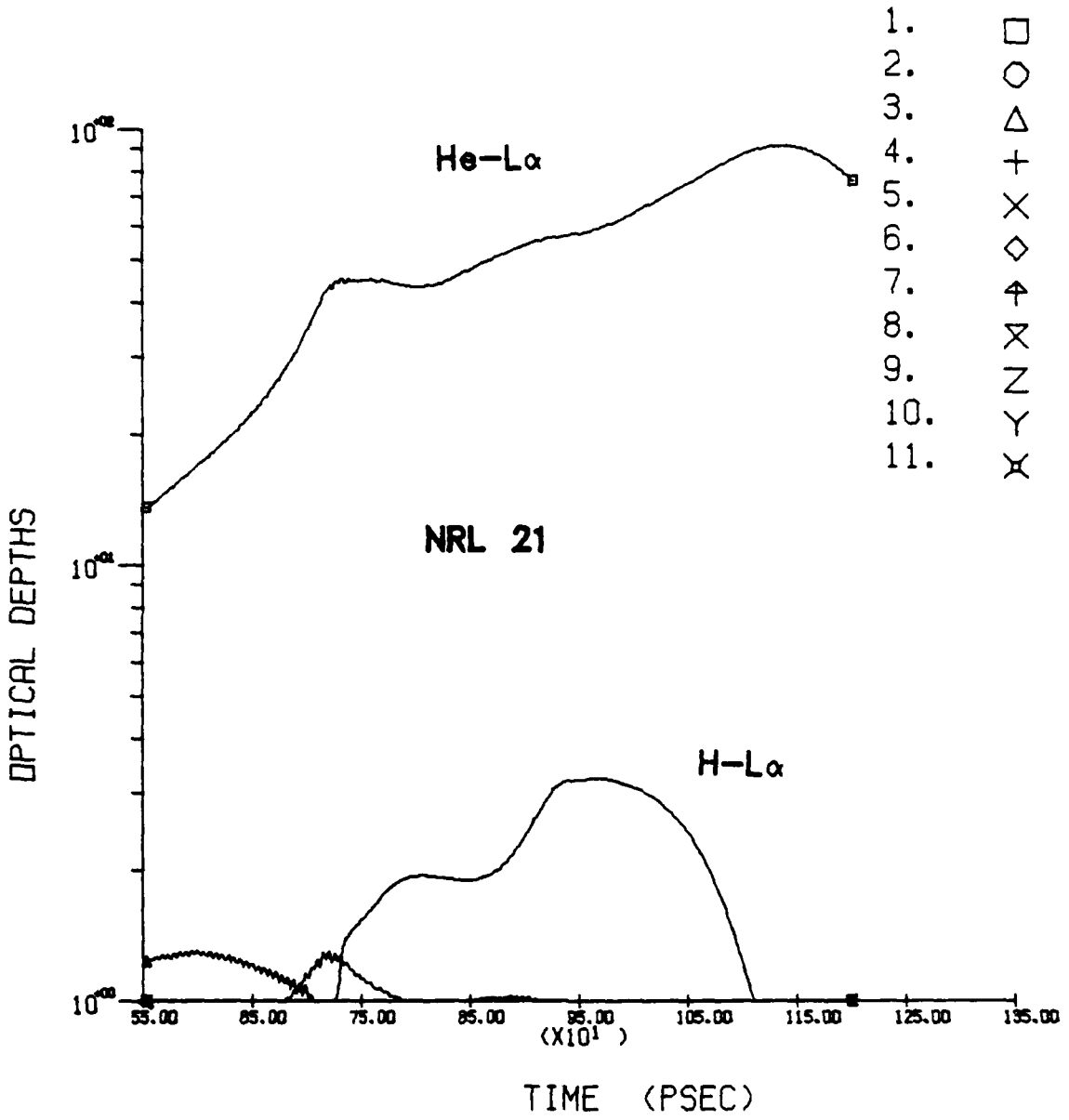


Fig. 5 Line opacity vs time for NRL 21.

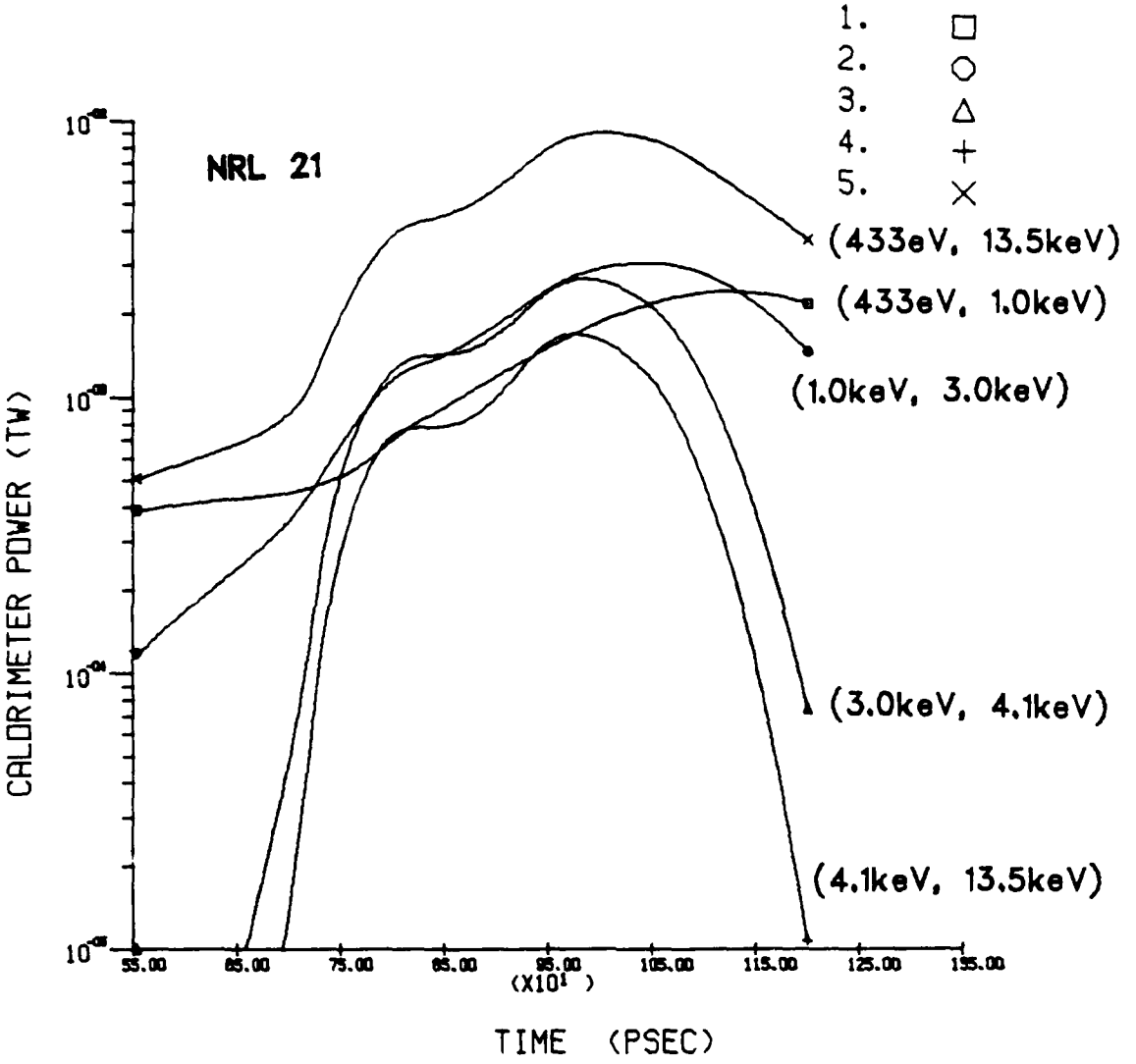


Fig. 6 Radiative energy in various spectral bands vs time for NRL 21.

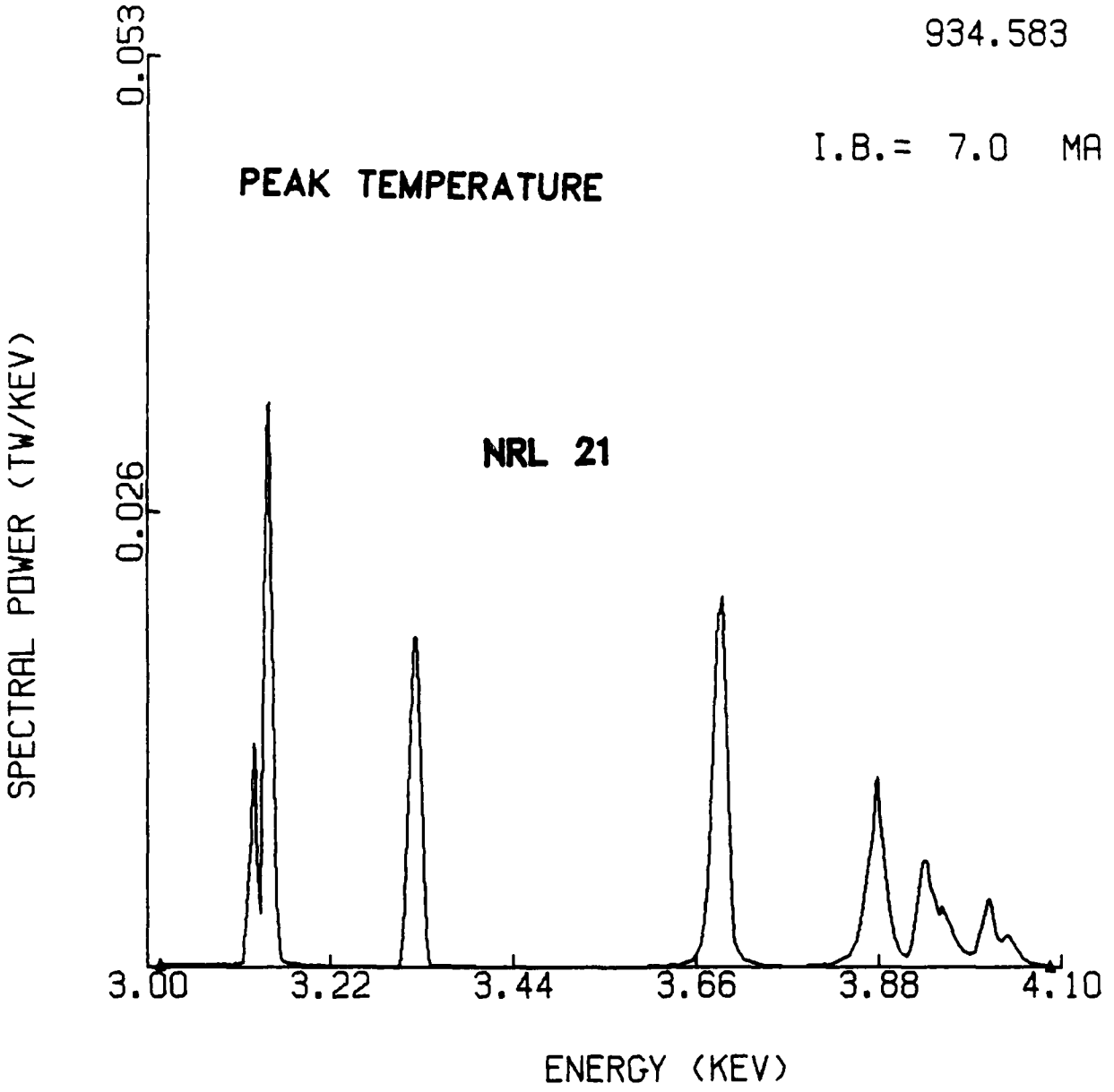


Fig. 7 Spectrum at time of peak temperature including source broadening for NRL 21.

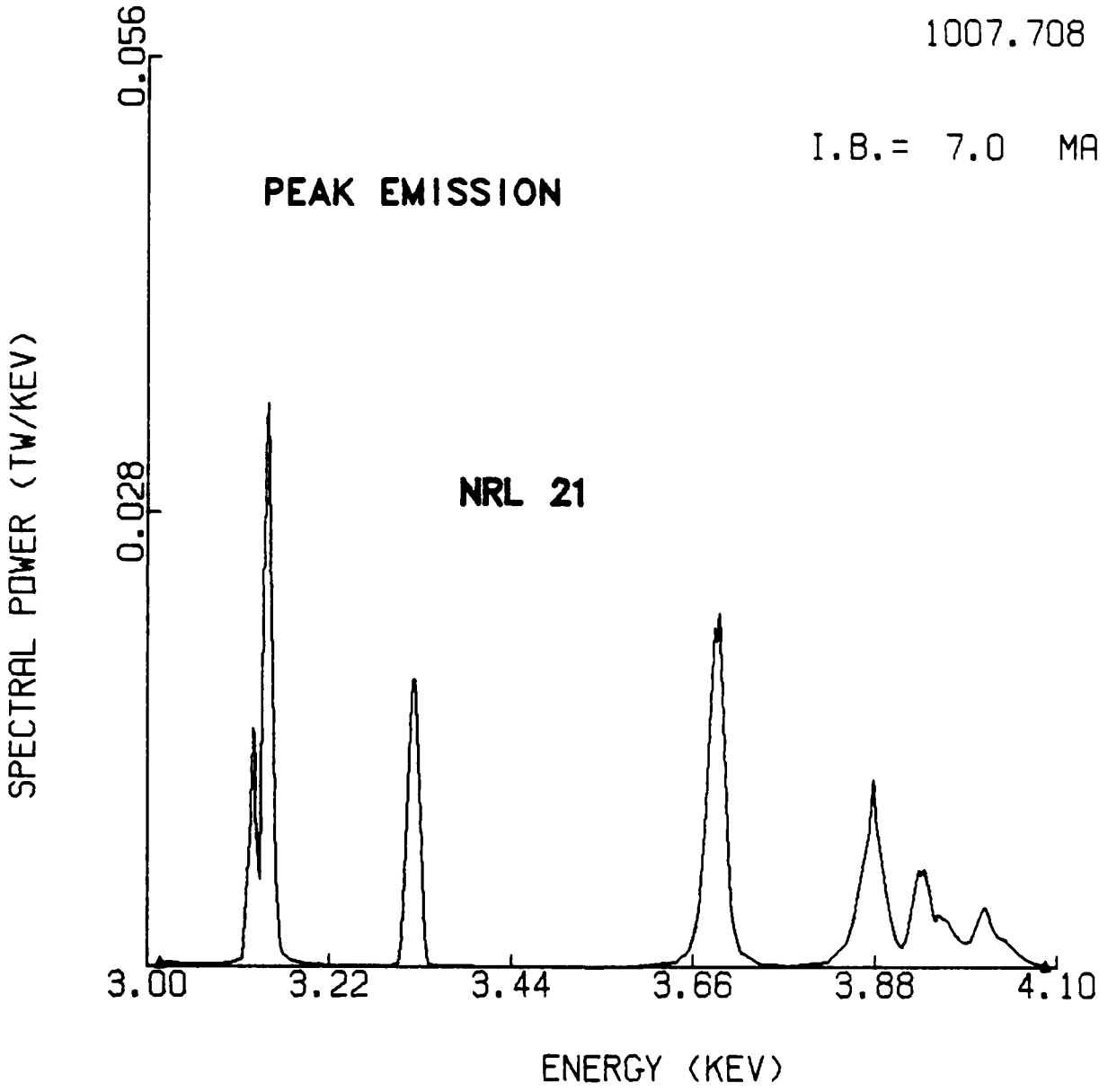


Fig. 8 Spectrum at time of peak emission including source broadening for NRL 21.

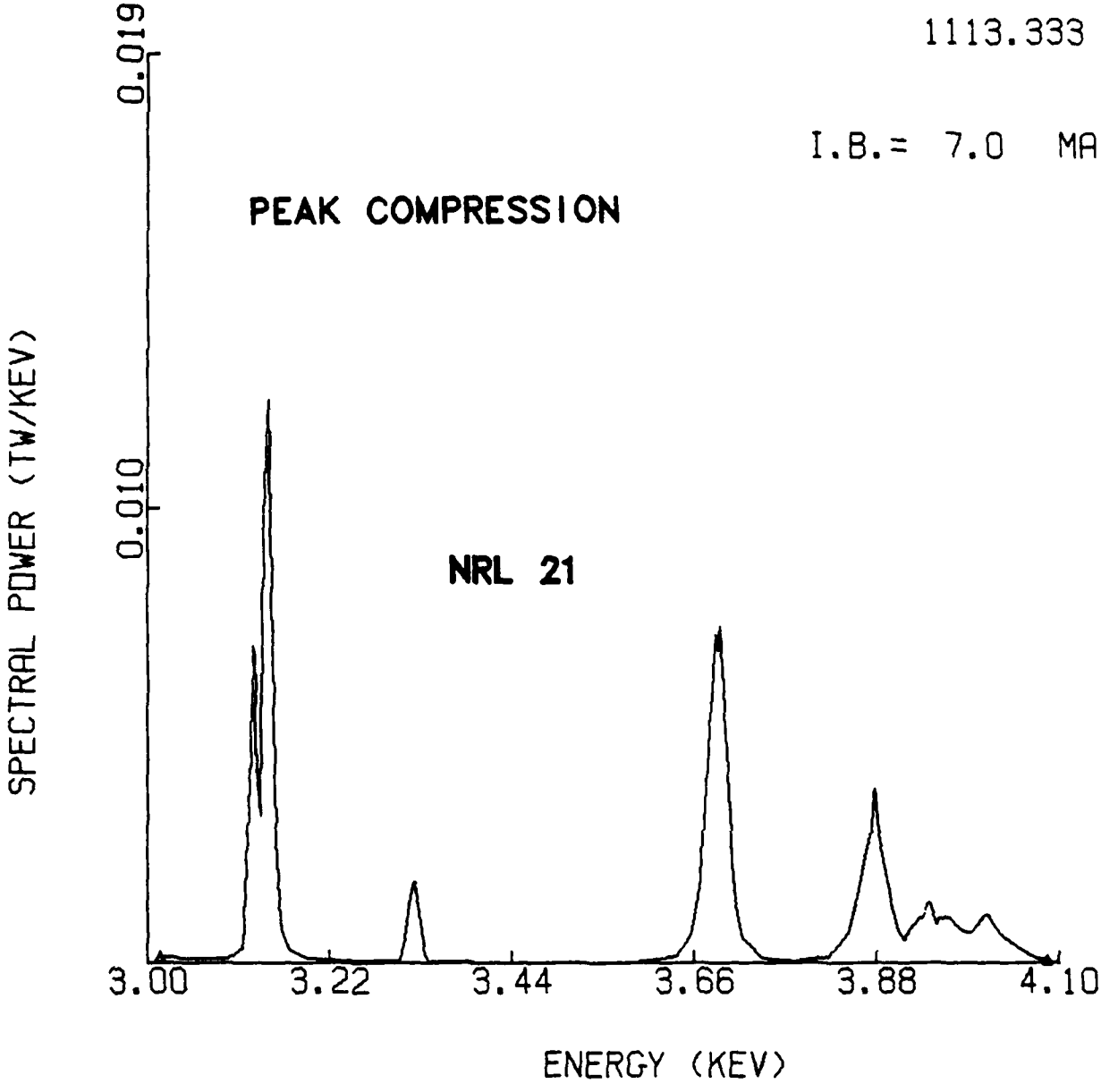


Fig. 9 Spectrum at time of peak compression including source broadening for NRL 21.

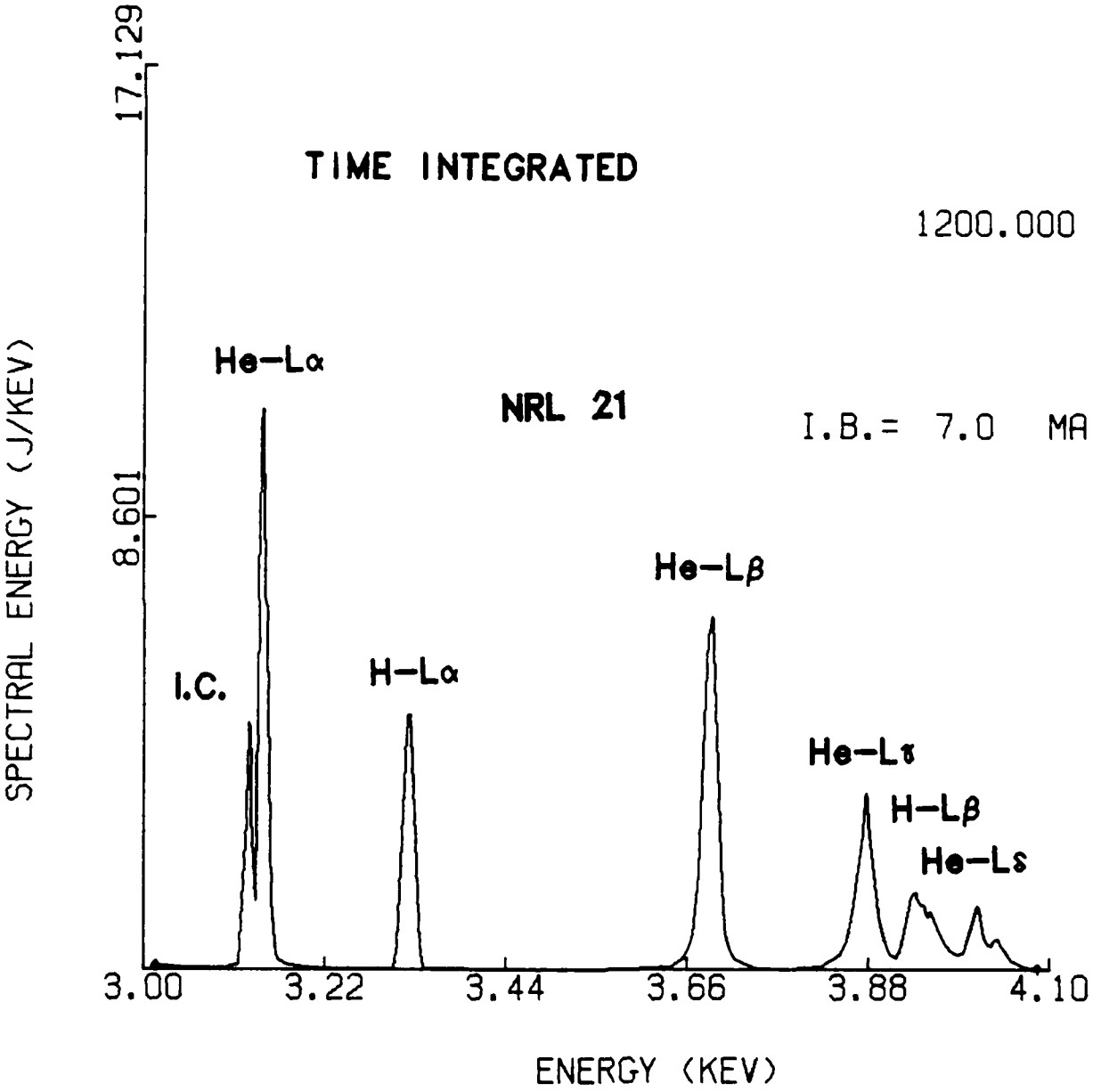


Fig. 10 Time integrated spectrum, including source broadening for NRL 21.

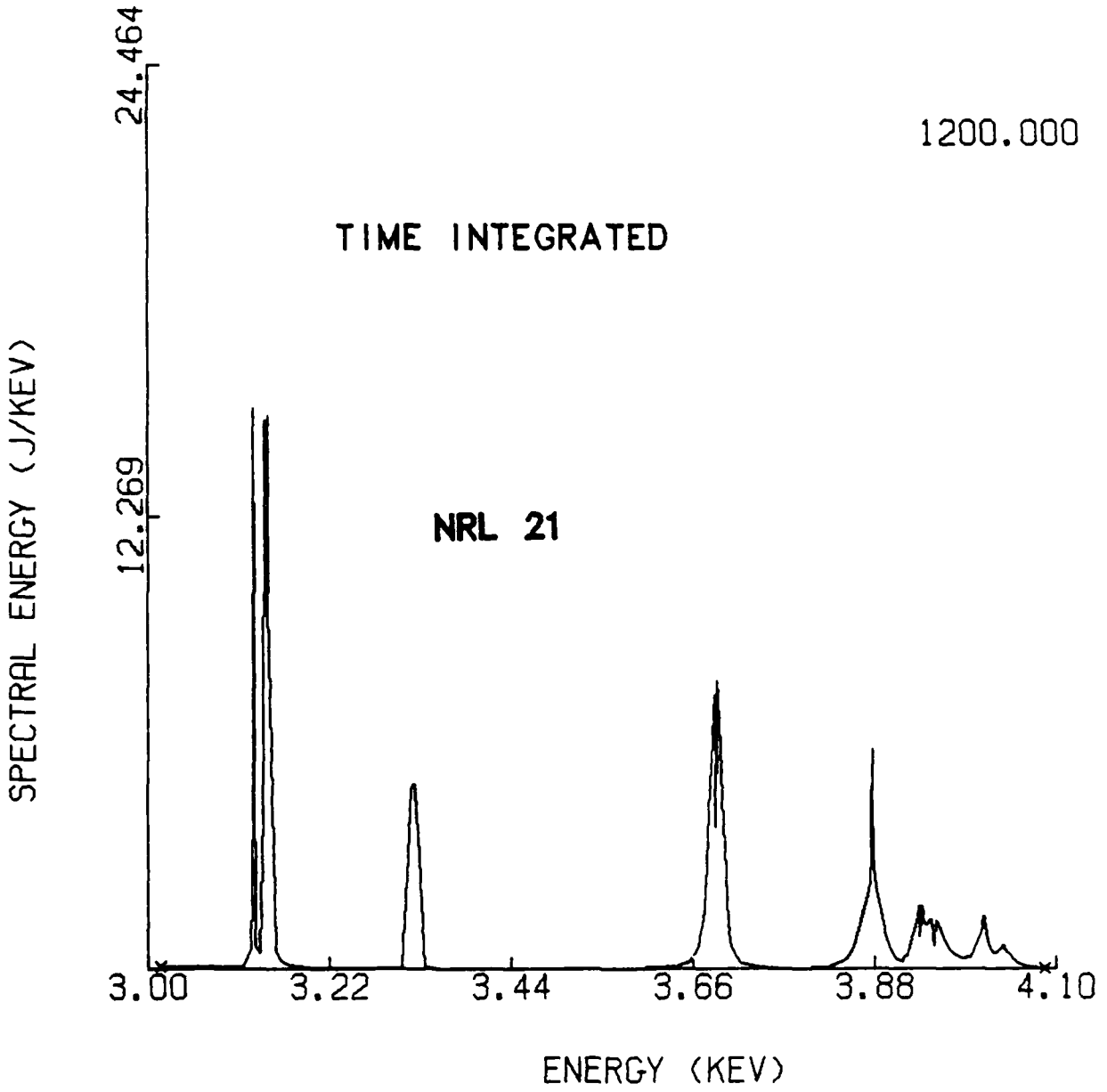


Fig. 11 Time integrated spectrum, not including source broadening for NRL 21.

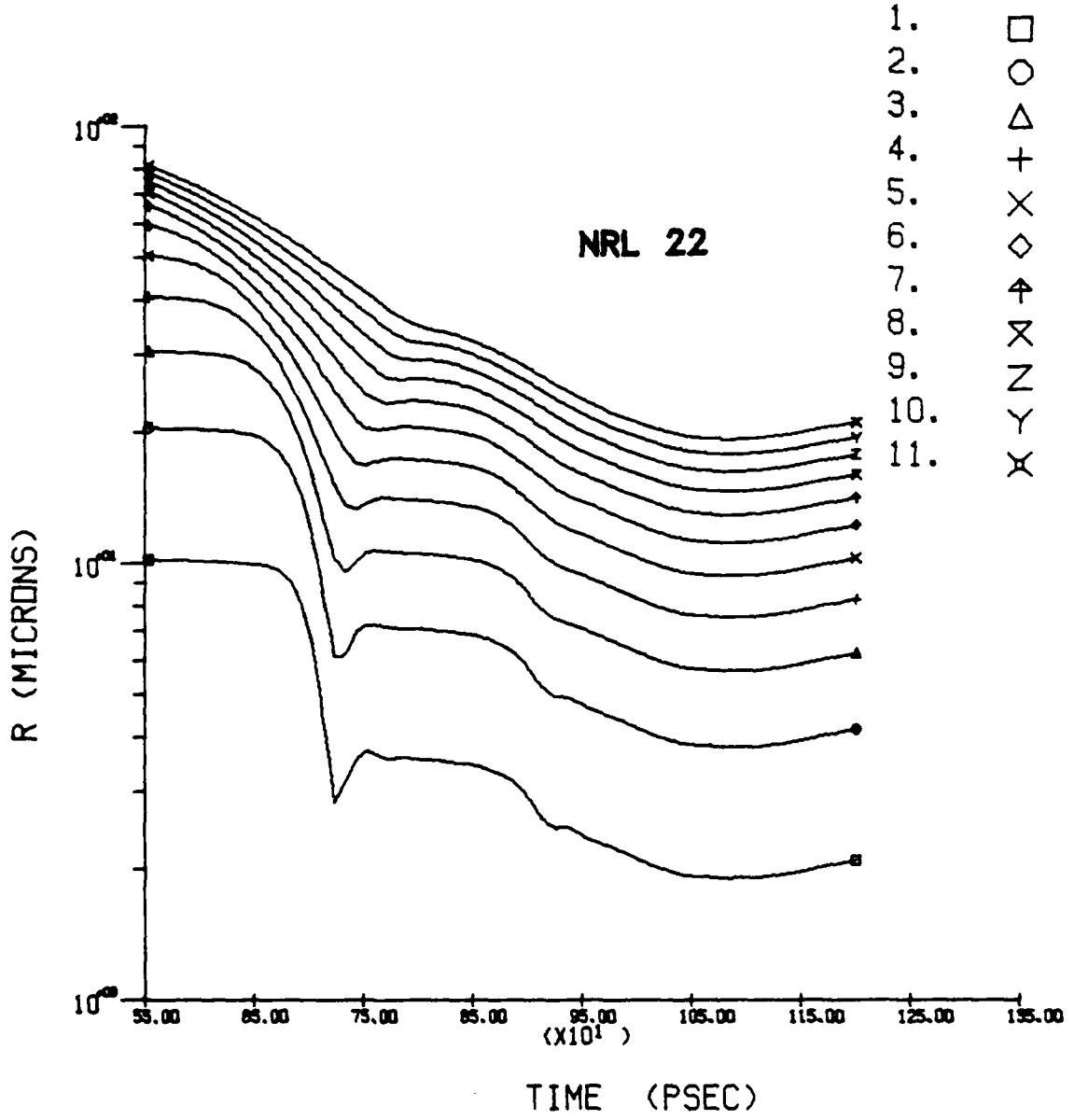


Fig. 12 Radius of cell centers vs time for NRL 22.

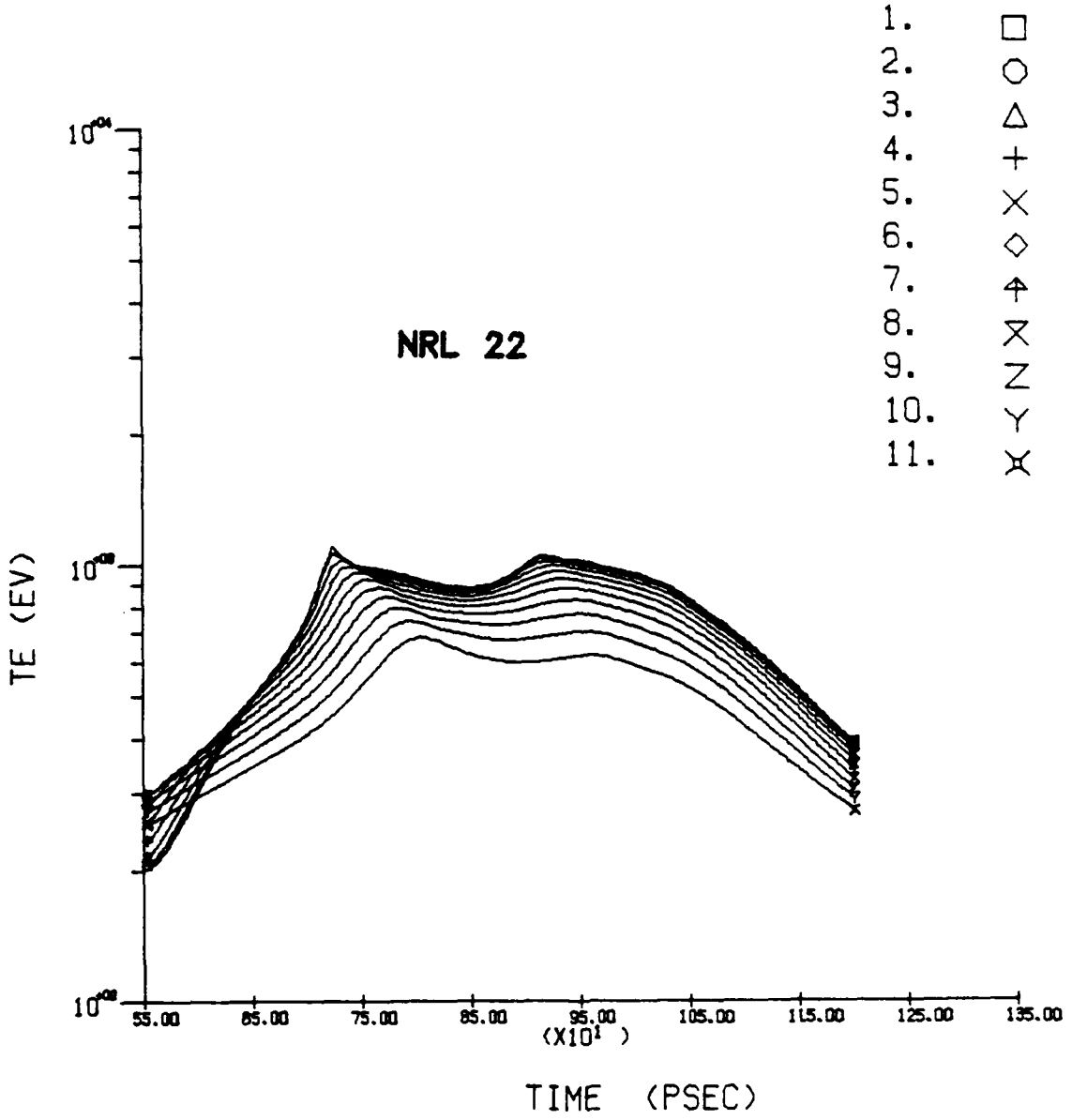


Fig. 13 Electron temperature vs time for NRL 22.

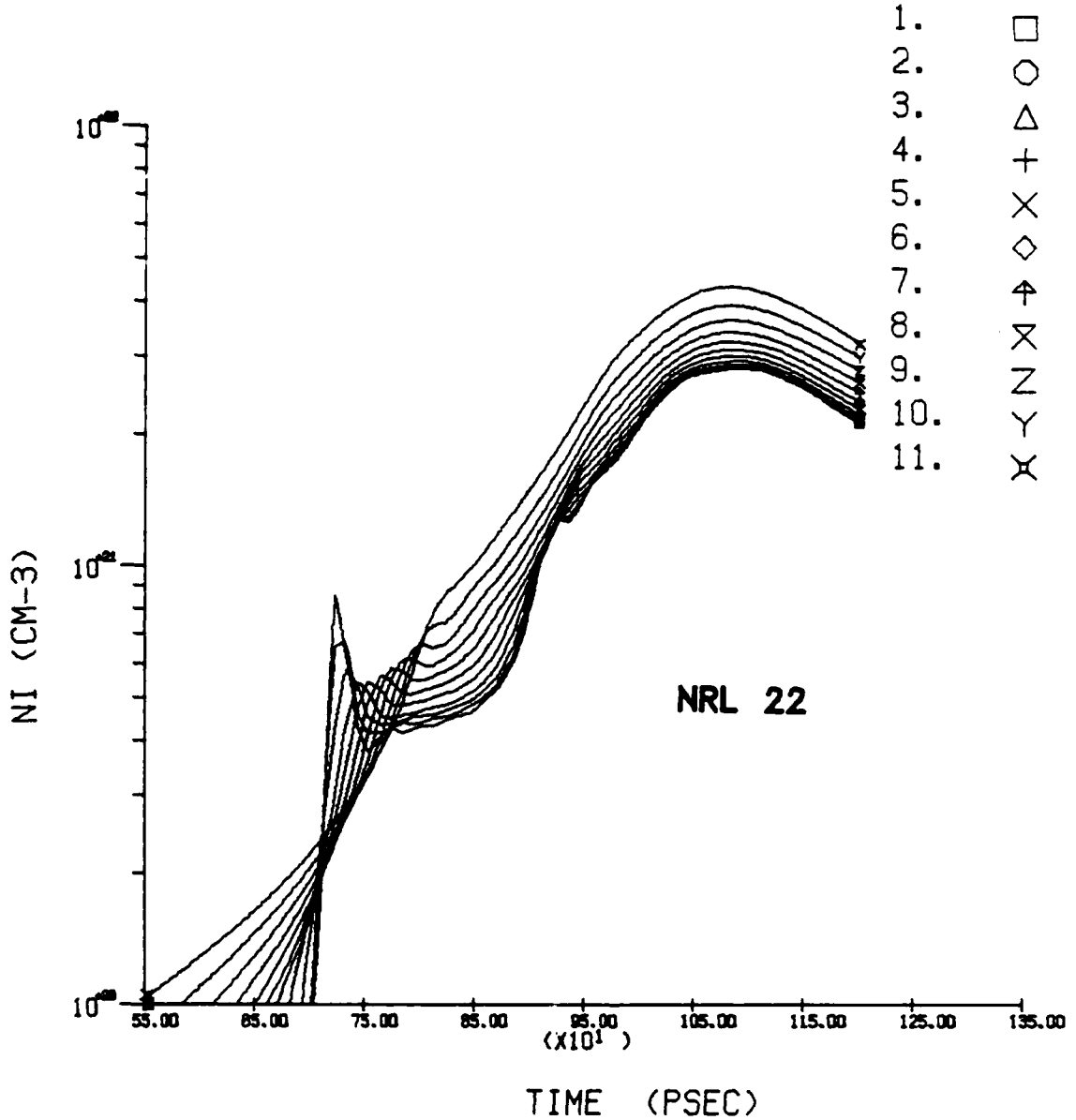


Fig. 14 Argon number density vs time for NRL 22.

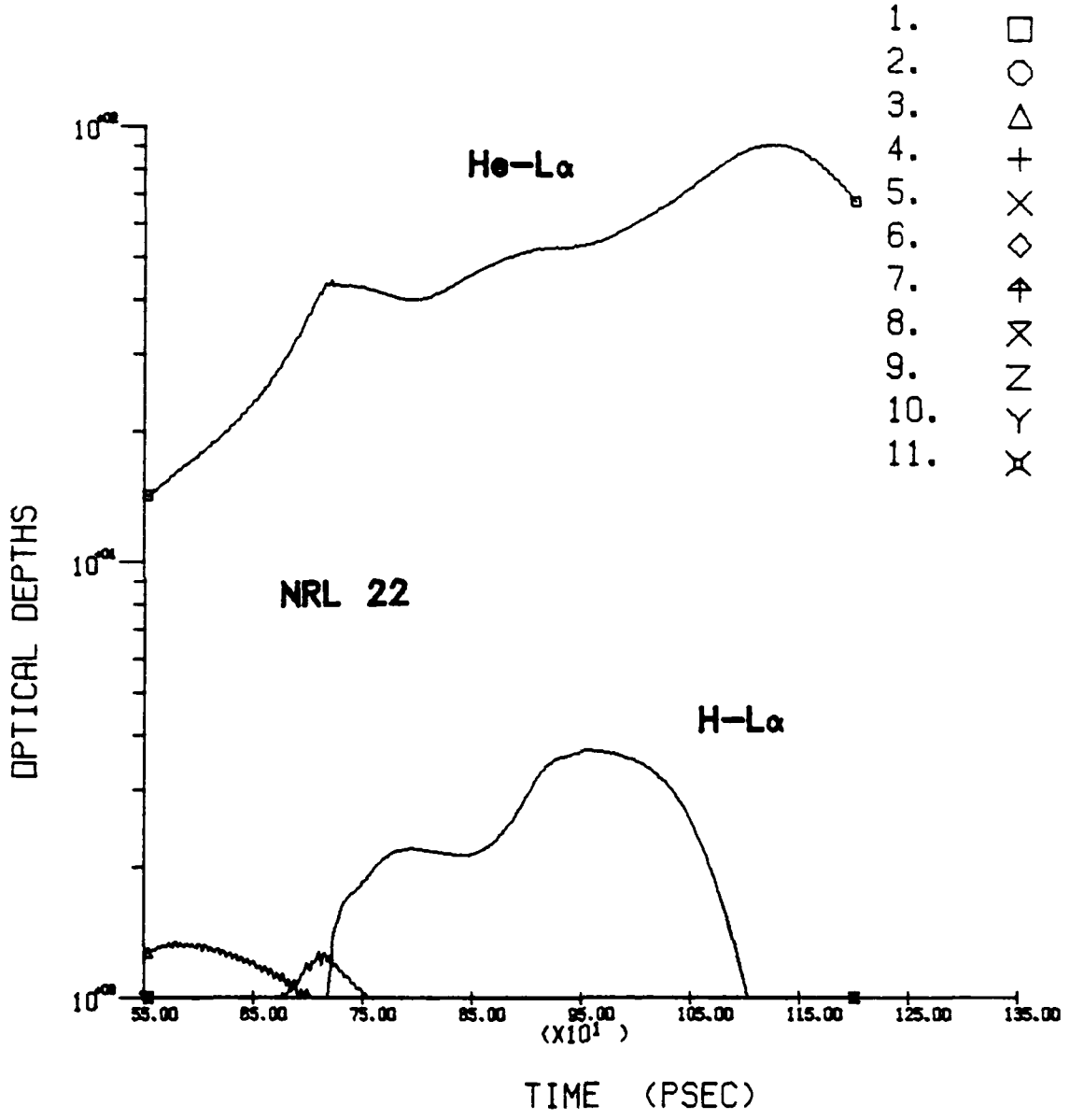


Fig. 15 Line opacity vs time for NRL 22.

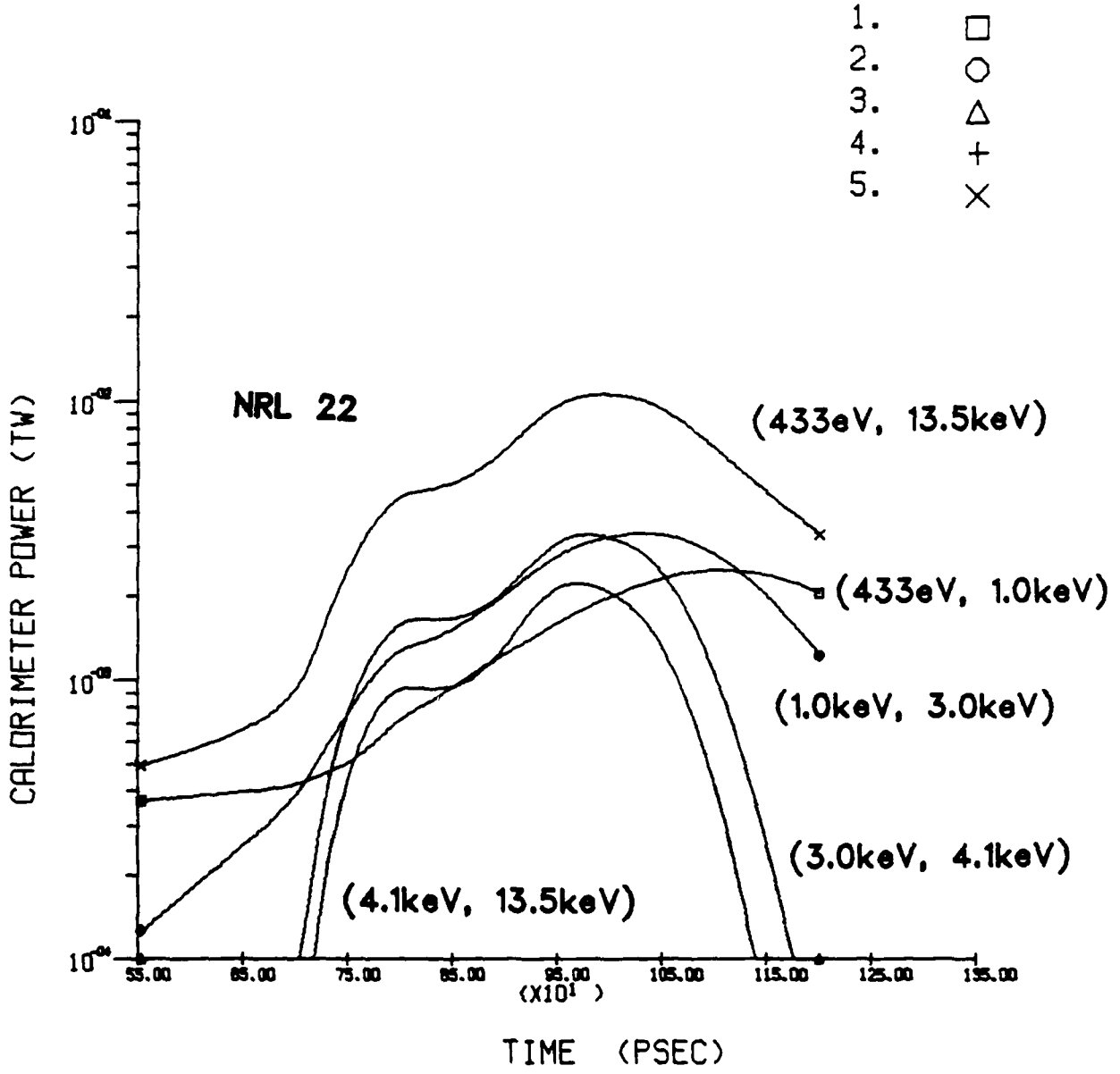


Fig. 16 Radiative energy in various spectral bands vs time for NRL 22.

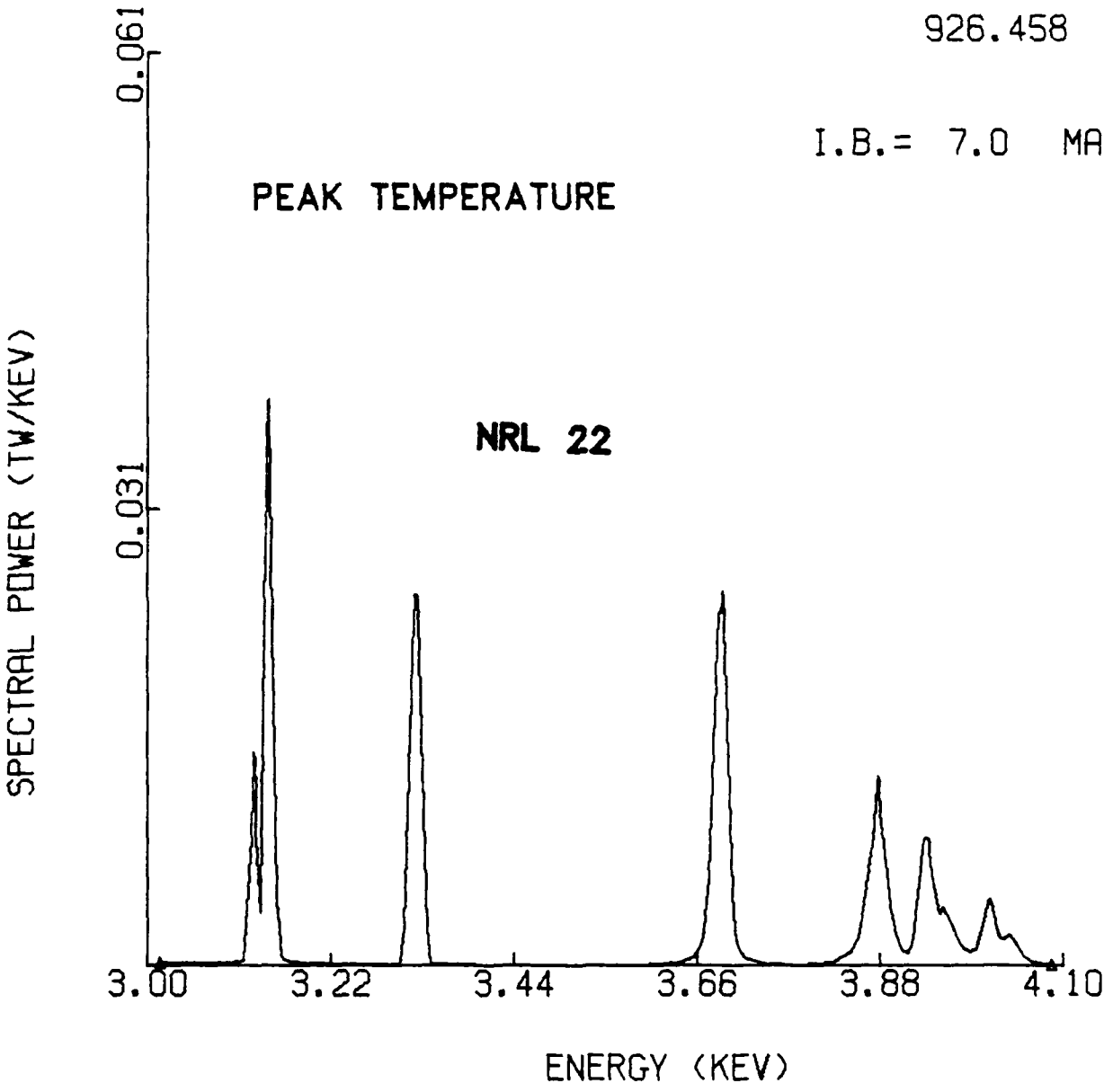


Fig. 17 Spectrum at time of peak temperature including source broadening for NRL 22.

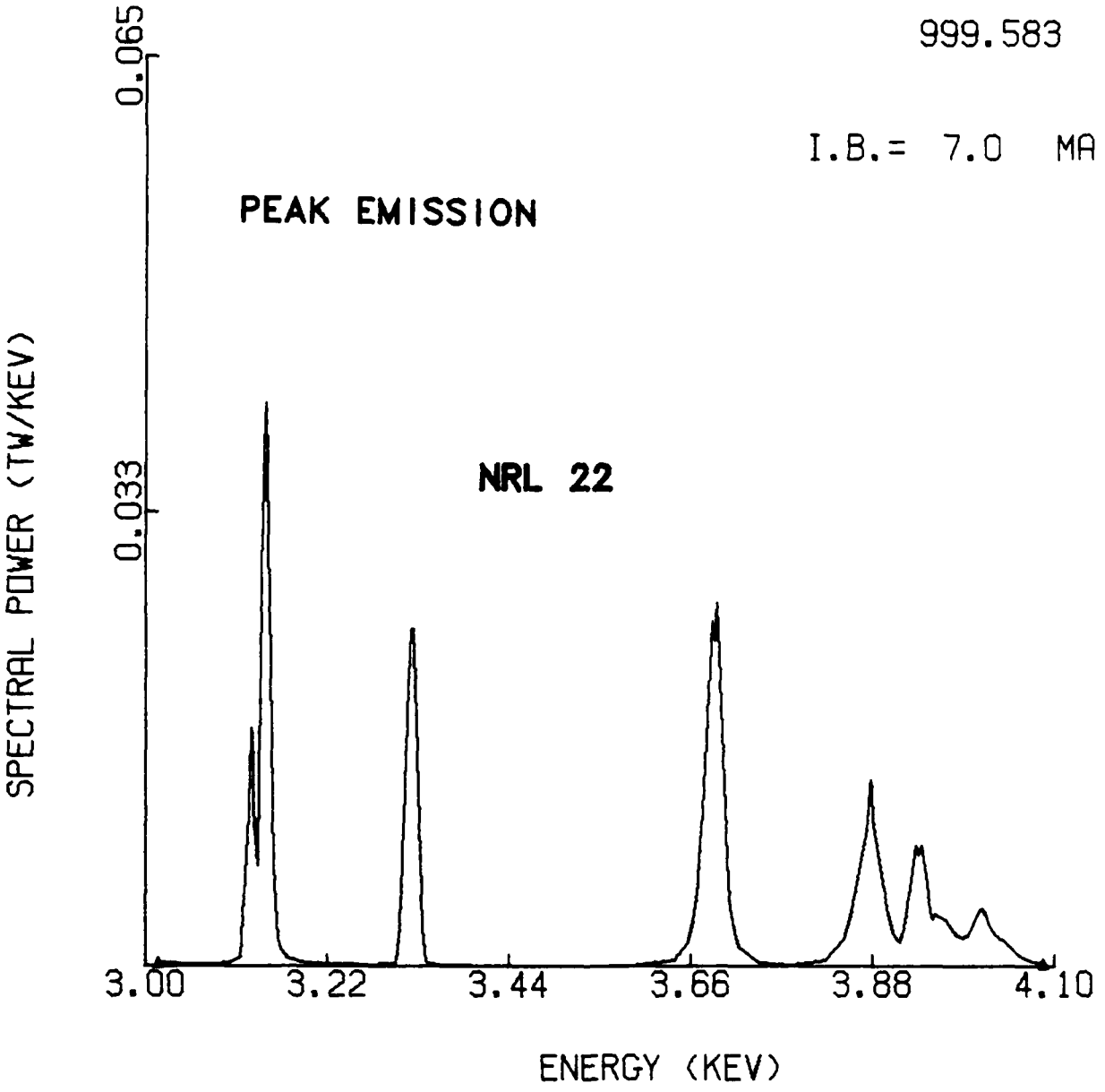


Fig. 18 Spectrum at time of peak emission including source broadening for NRL 22.

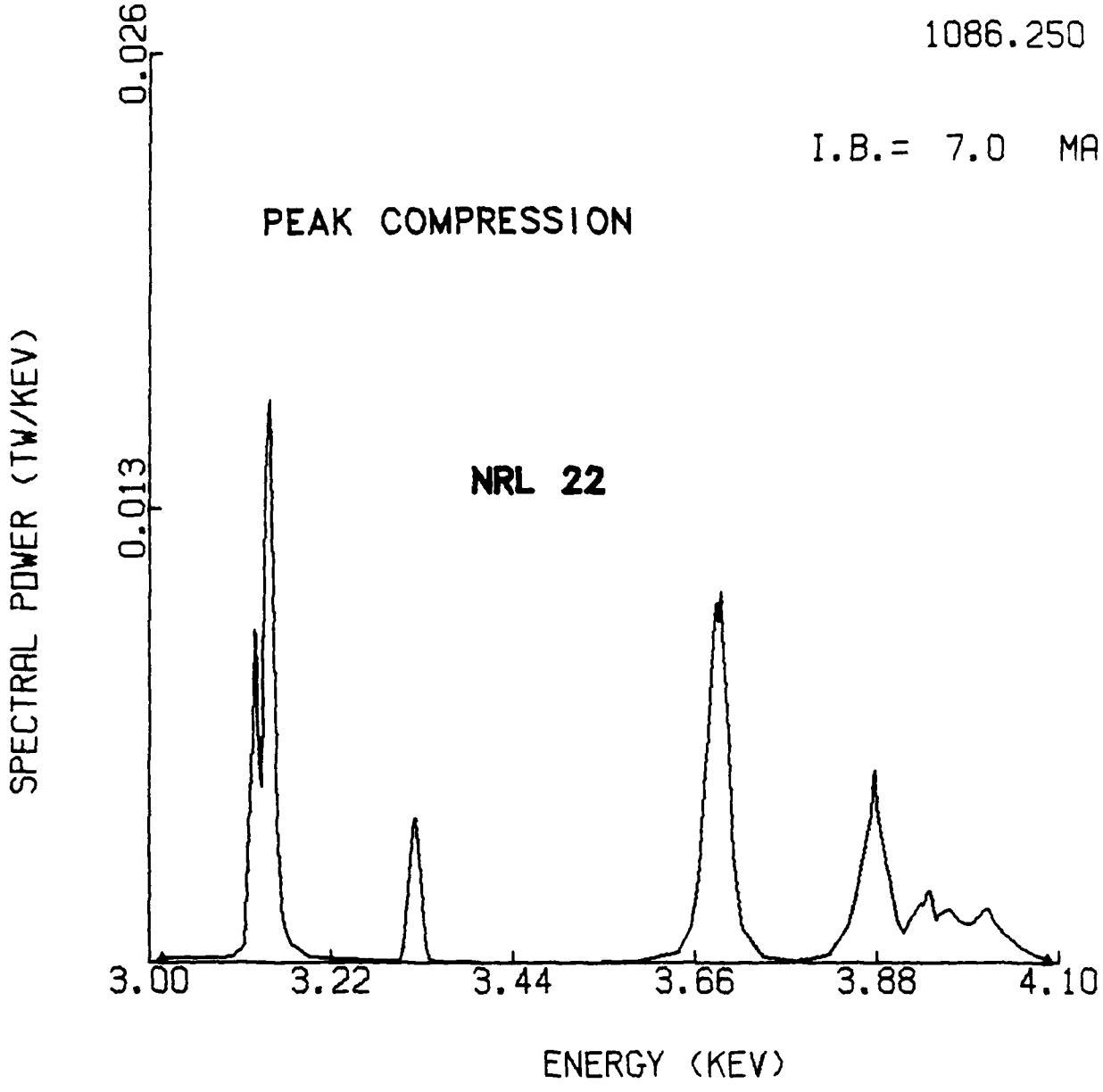


Fig. 19 Spectrum at time of peak compression including source broadening for NRL 22.

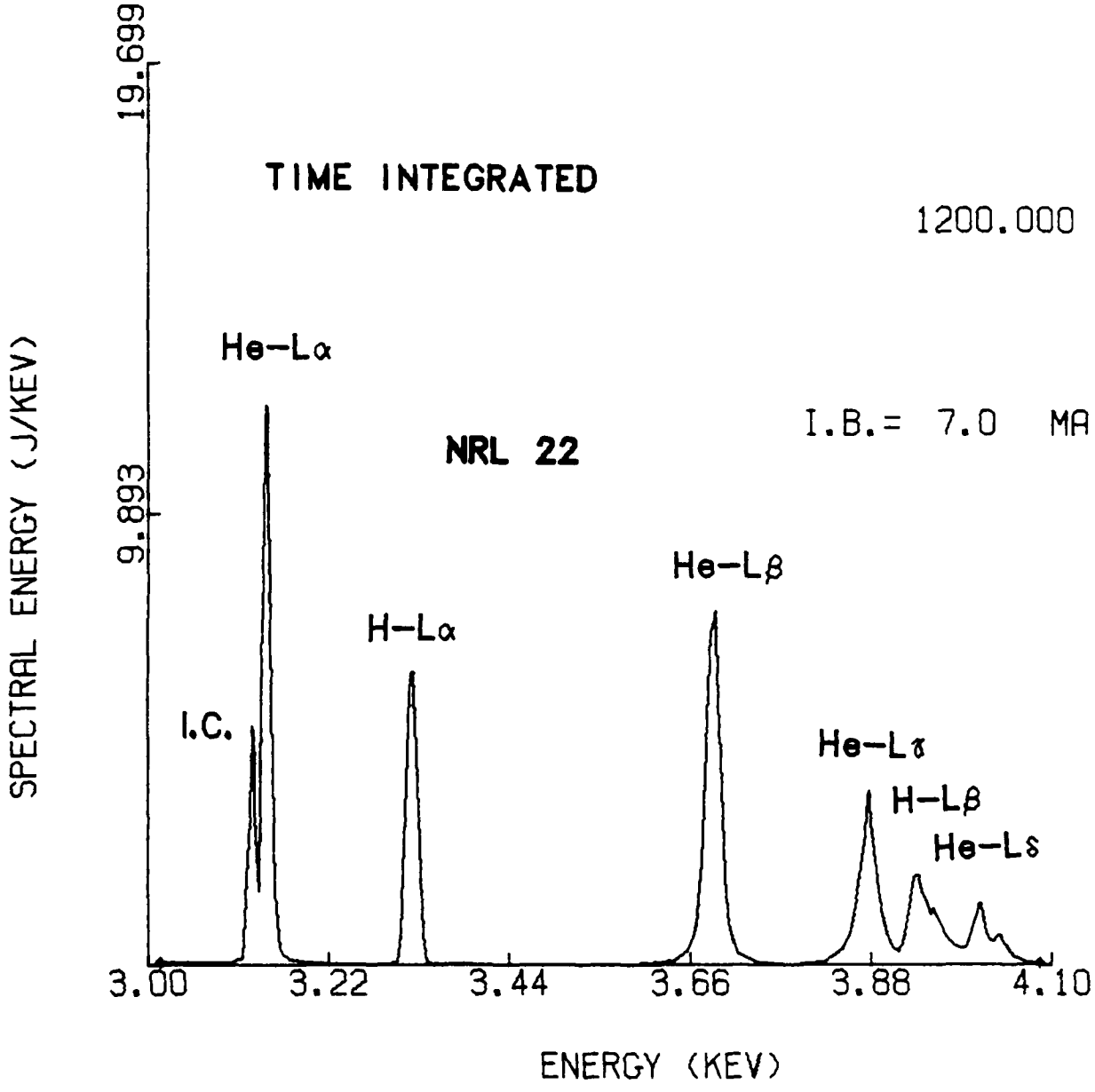


Fig. 20 Time integrated spectrum, including source broadening for NRL 22.

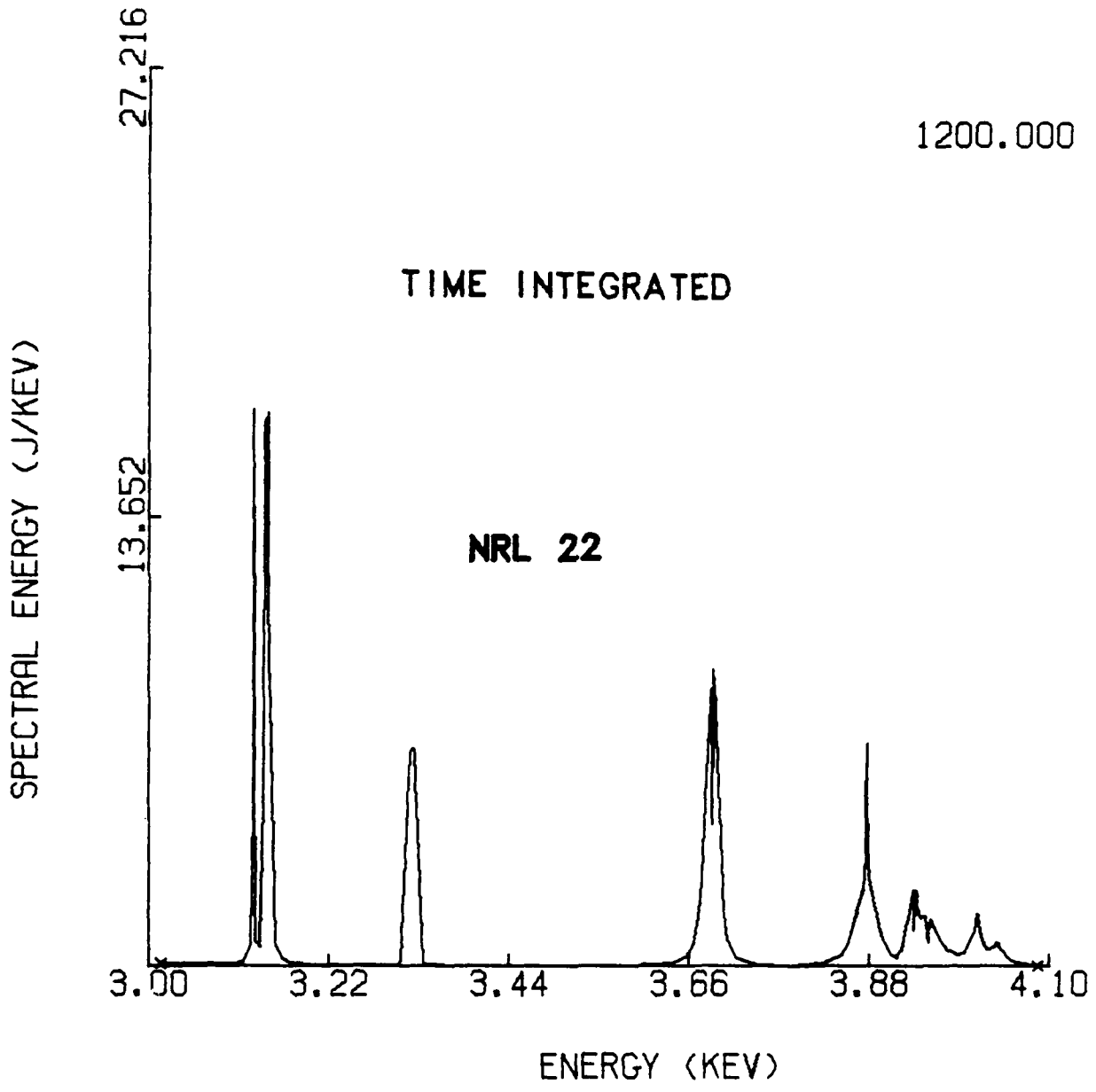


Fig. 21 Time integrated spectrum, not including source broadening for NRL 22.

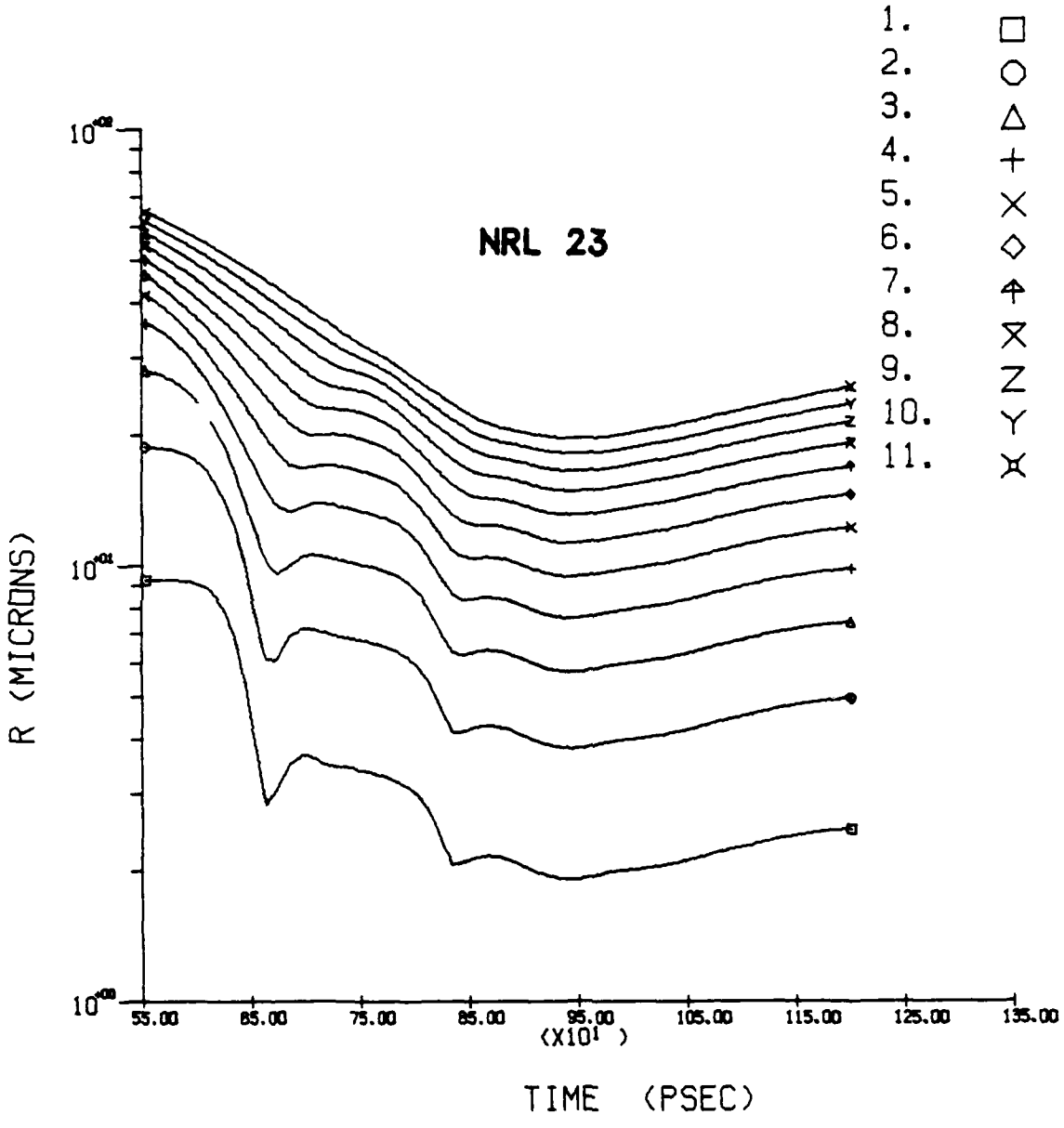


Fig. 22 Radius of cell centers vs time for NRL 23.

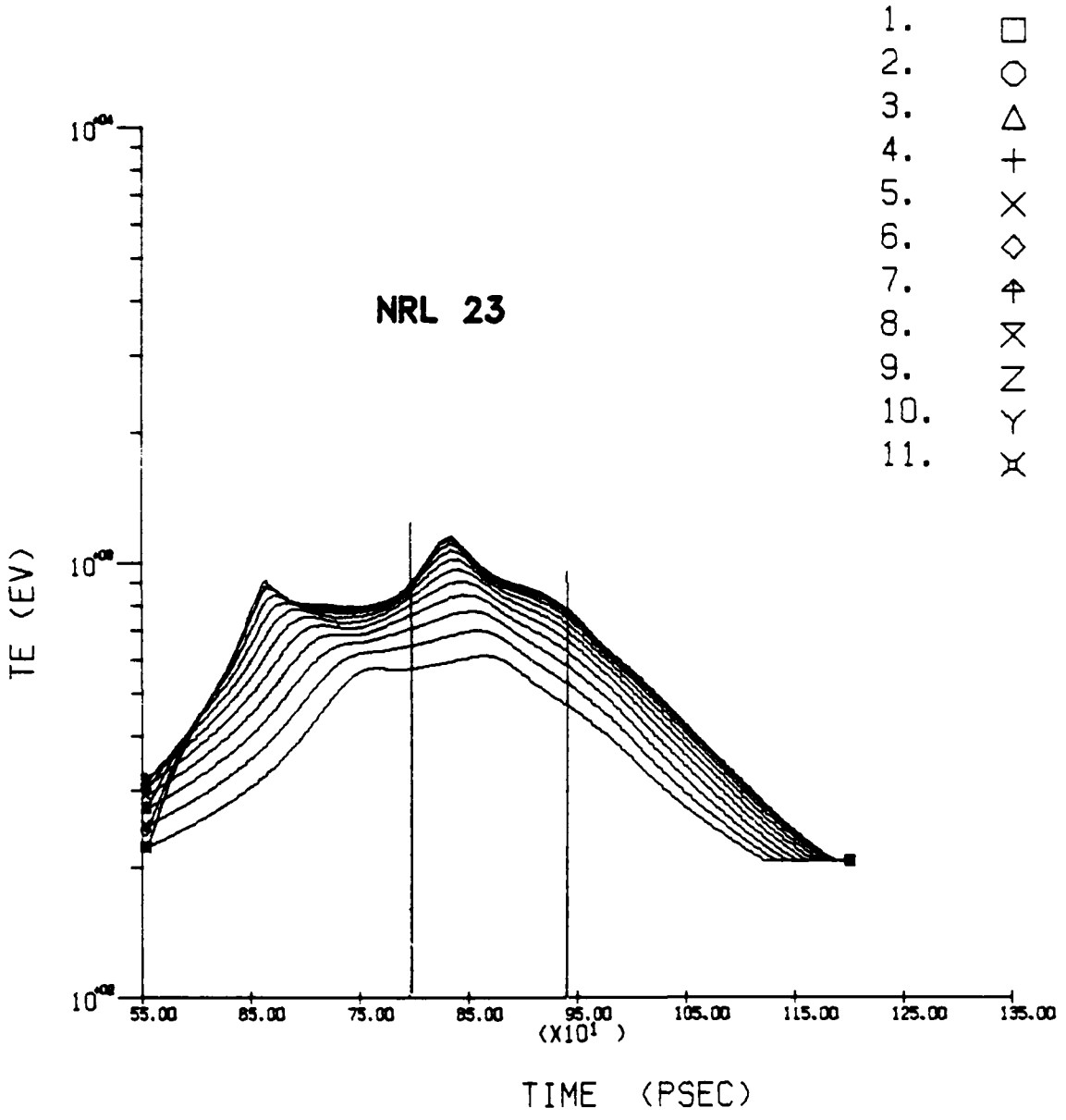


Fig. 23 Electron temperature vs time for NRL 23.

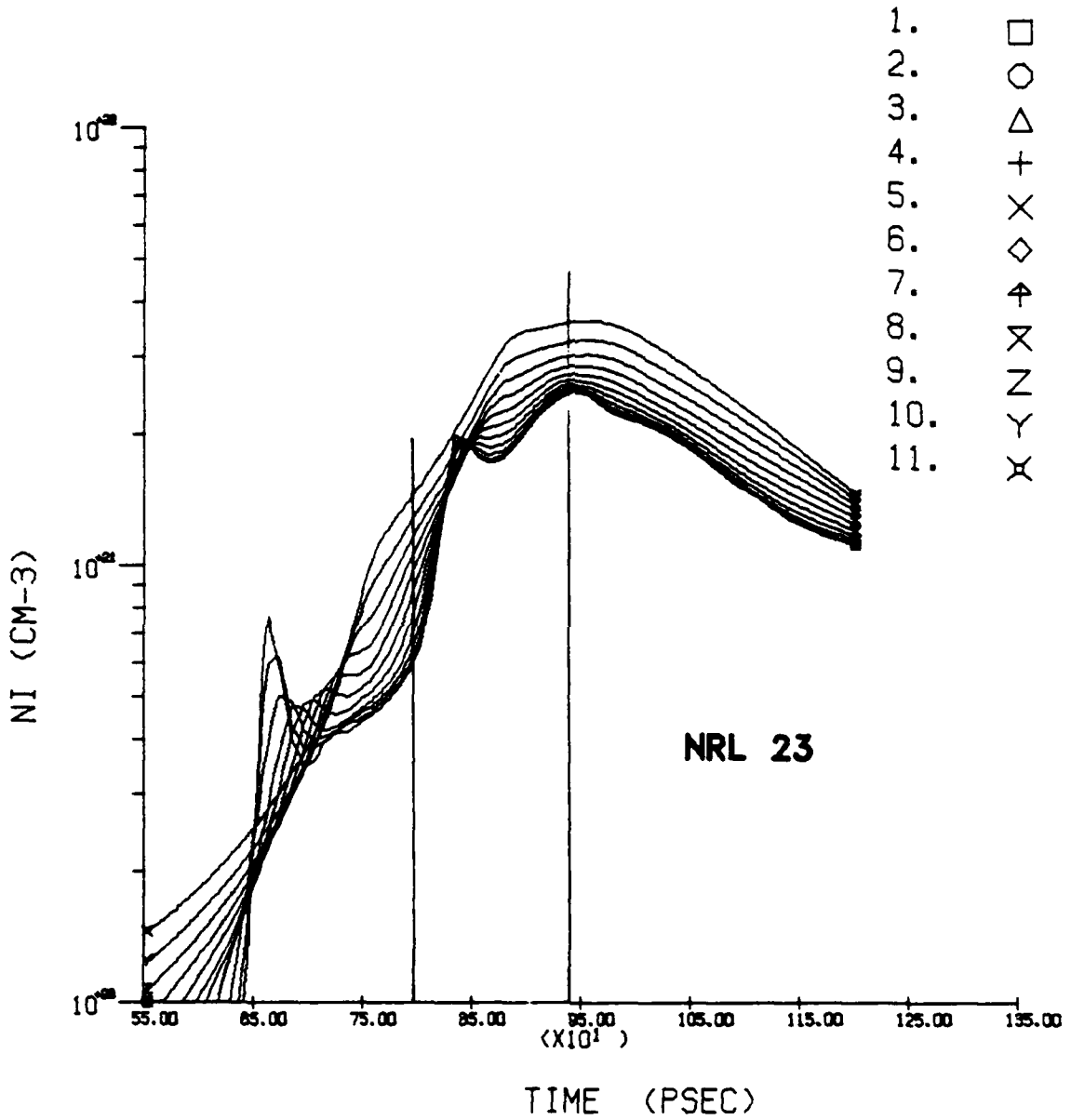


Fig. 24 Argon number density vs time for NRL 23.

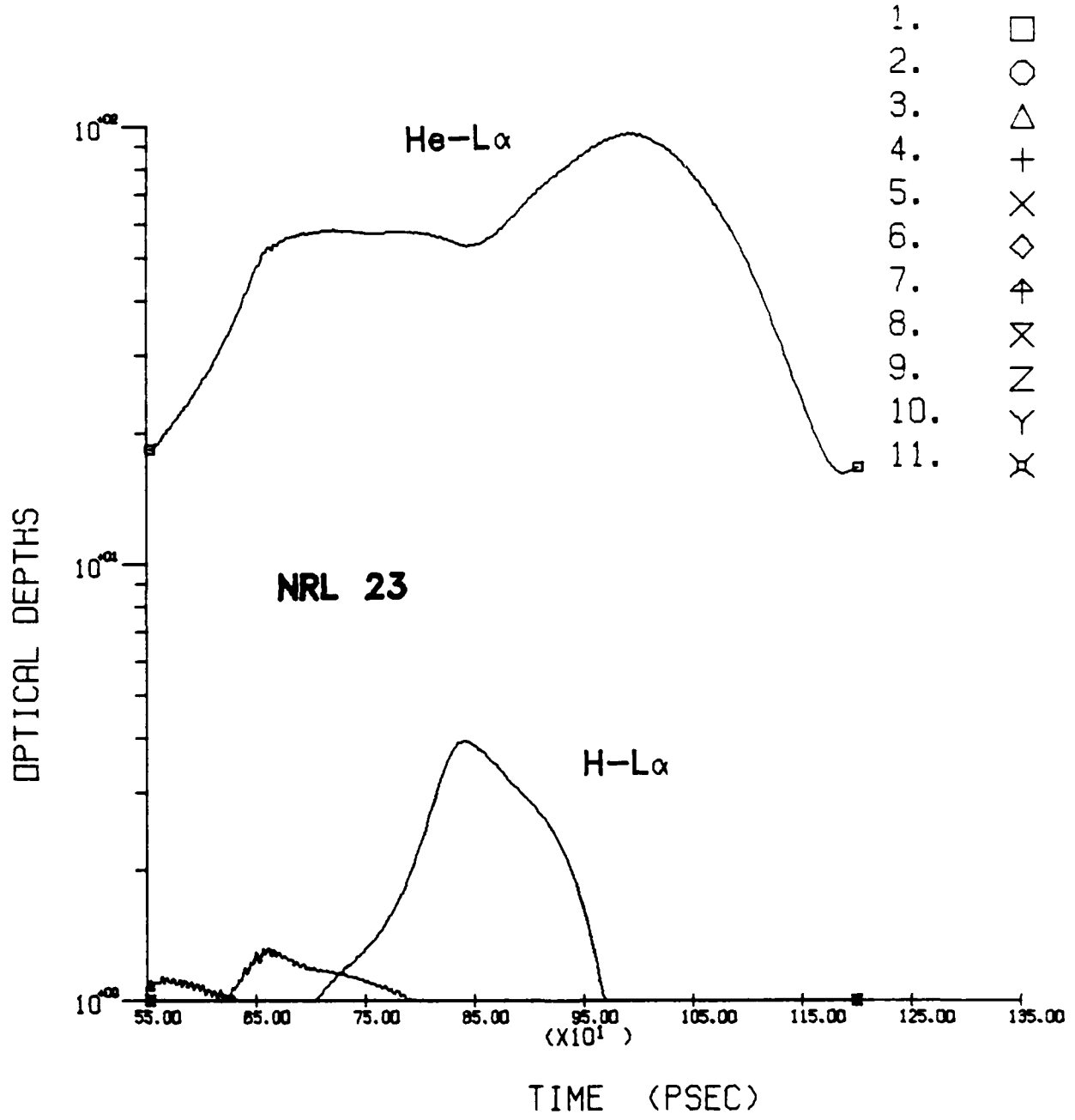


Fig. 25 Line opacity vs time for NRL 23.

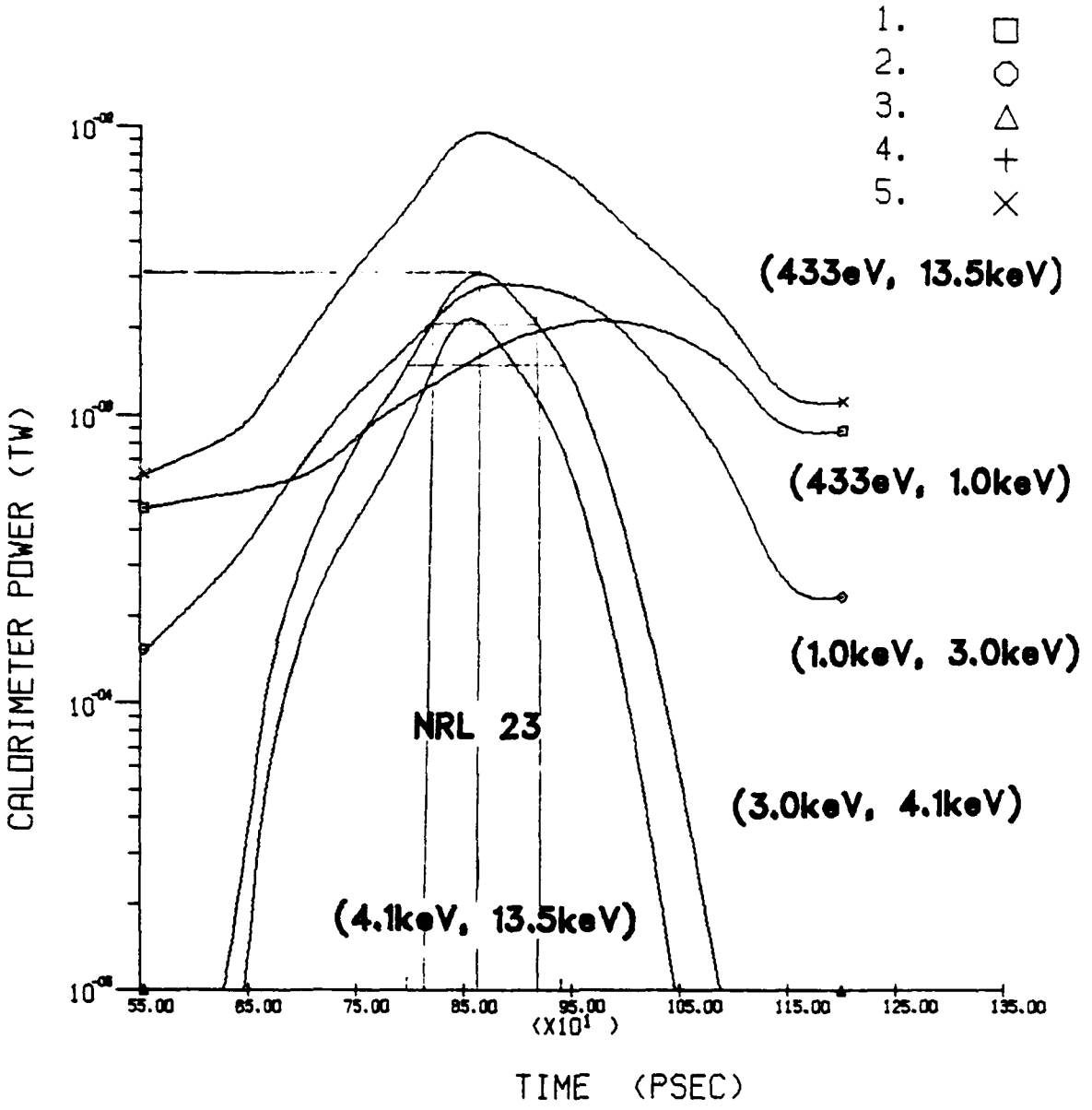


Fig. 26 Radiative energy in various spectral bands vs time for NRL 23.

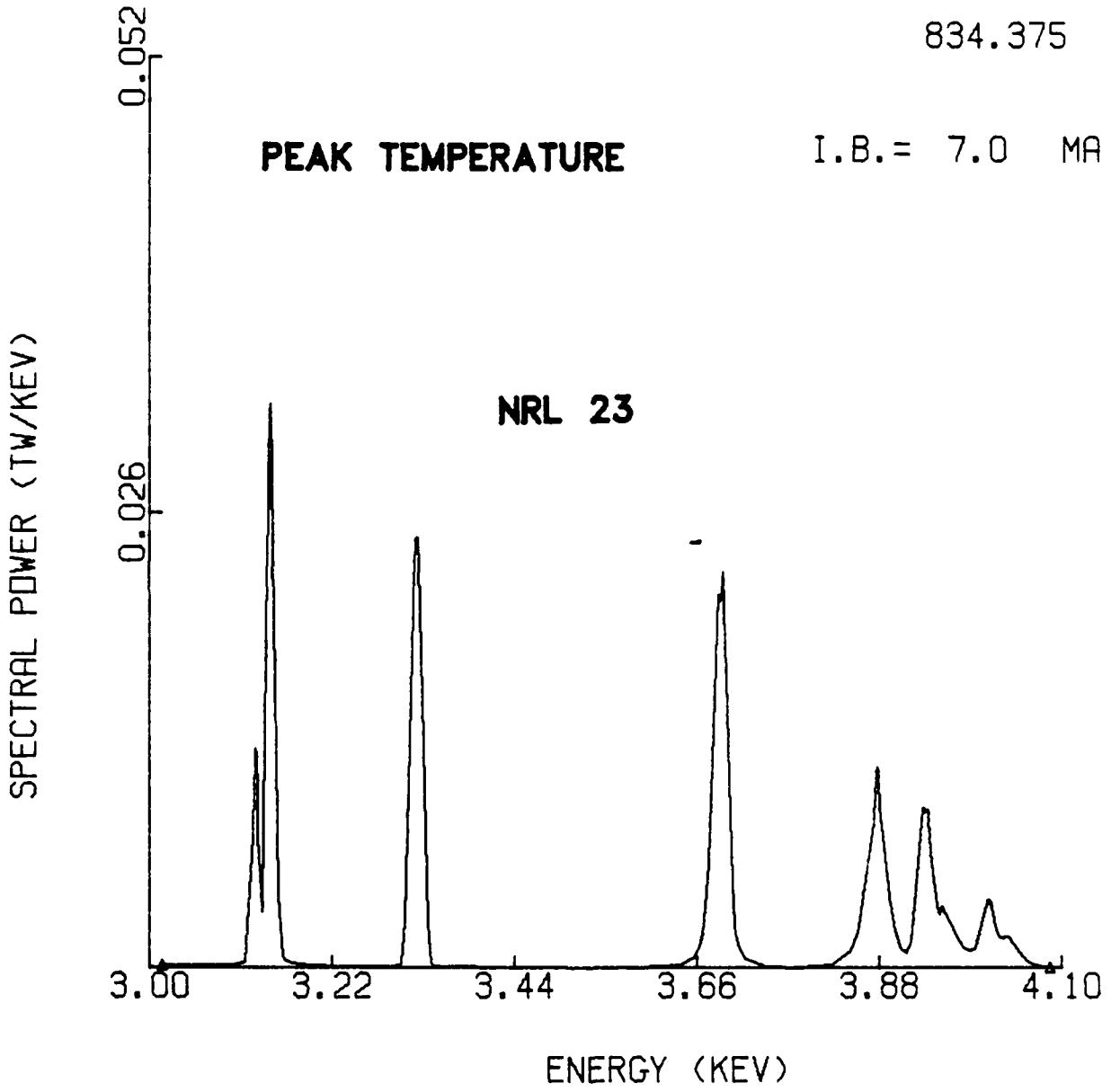


Fig. 27 Spectrum at time of peak temperature including source broadening for NRL 23.

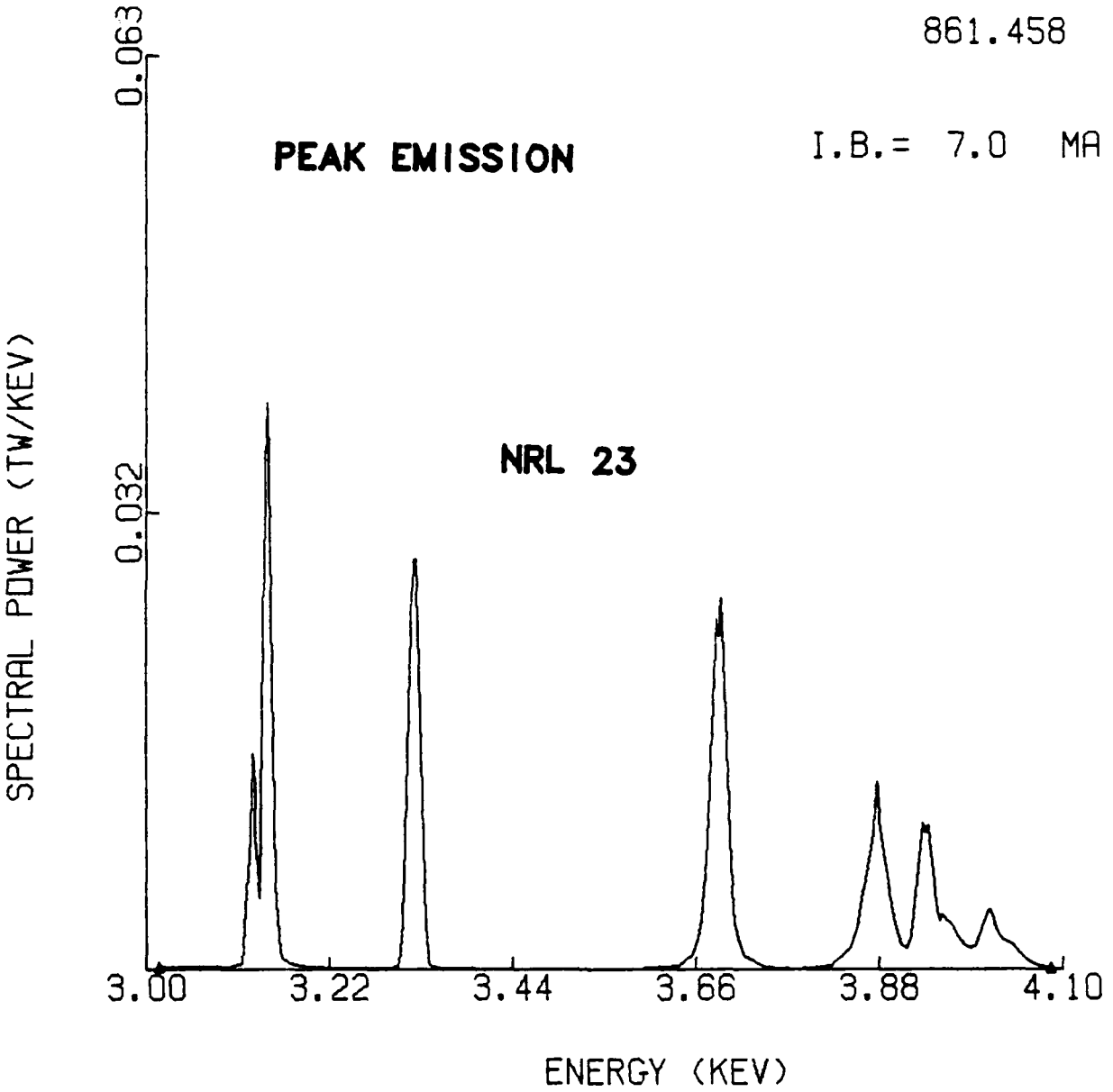


Fig. 28 Spectrum at time of peak emission including source broadening for NRL 23.

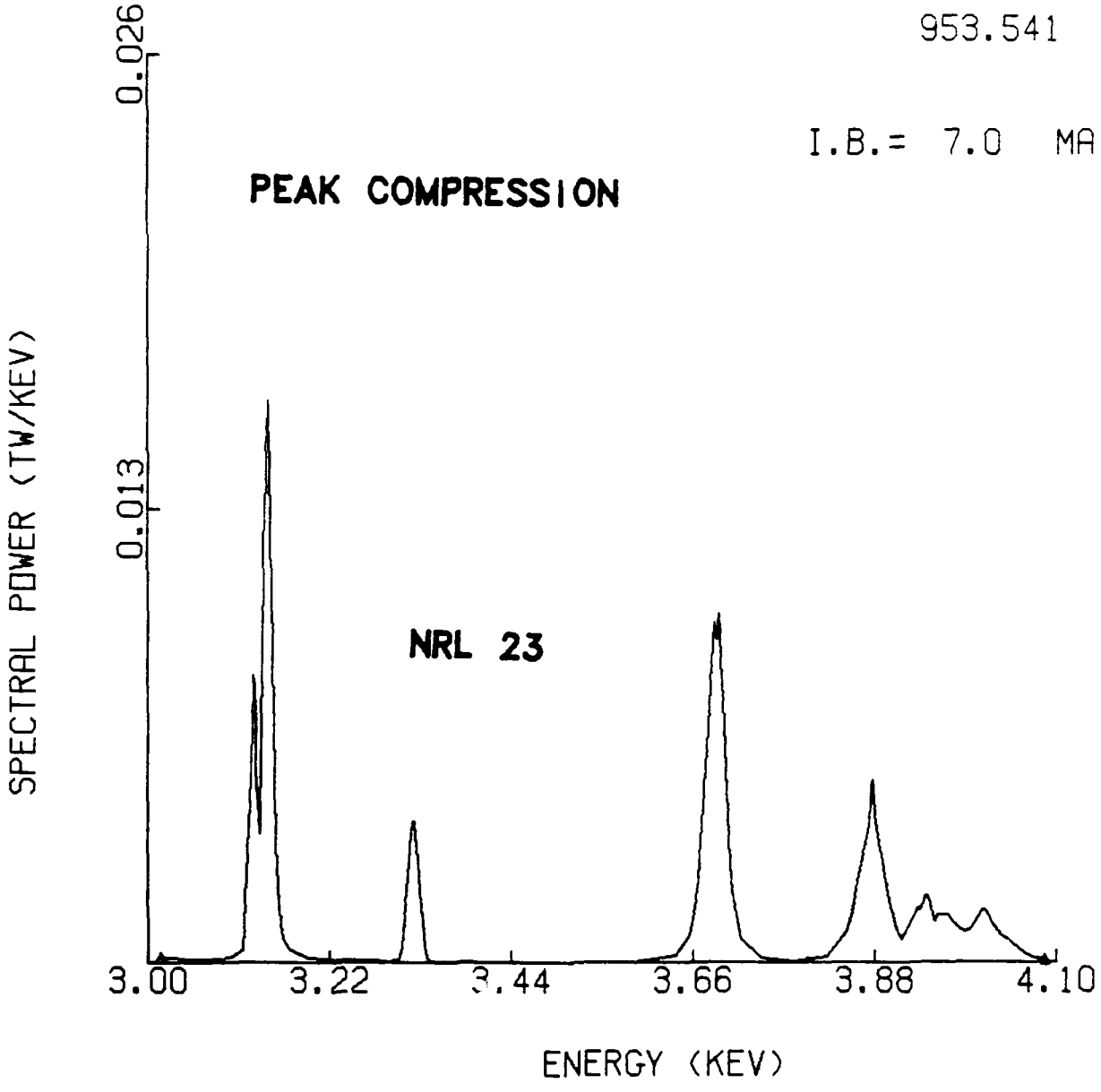


Fig. 29 Spectrum at time of peak compression including source broadening for NRL 23.

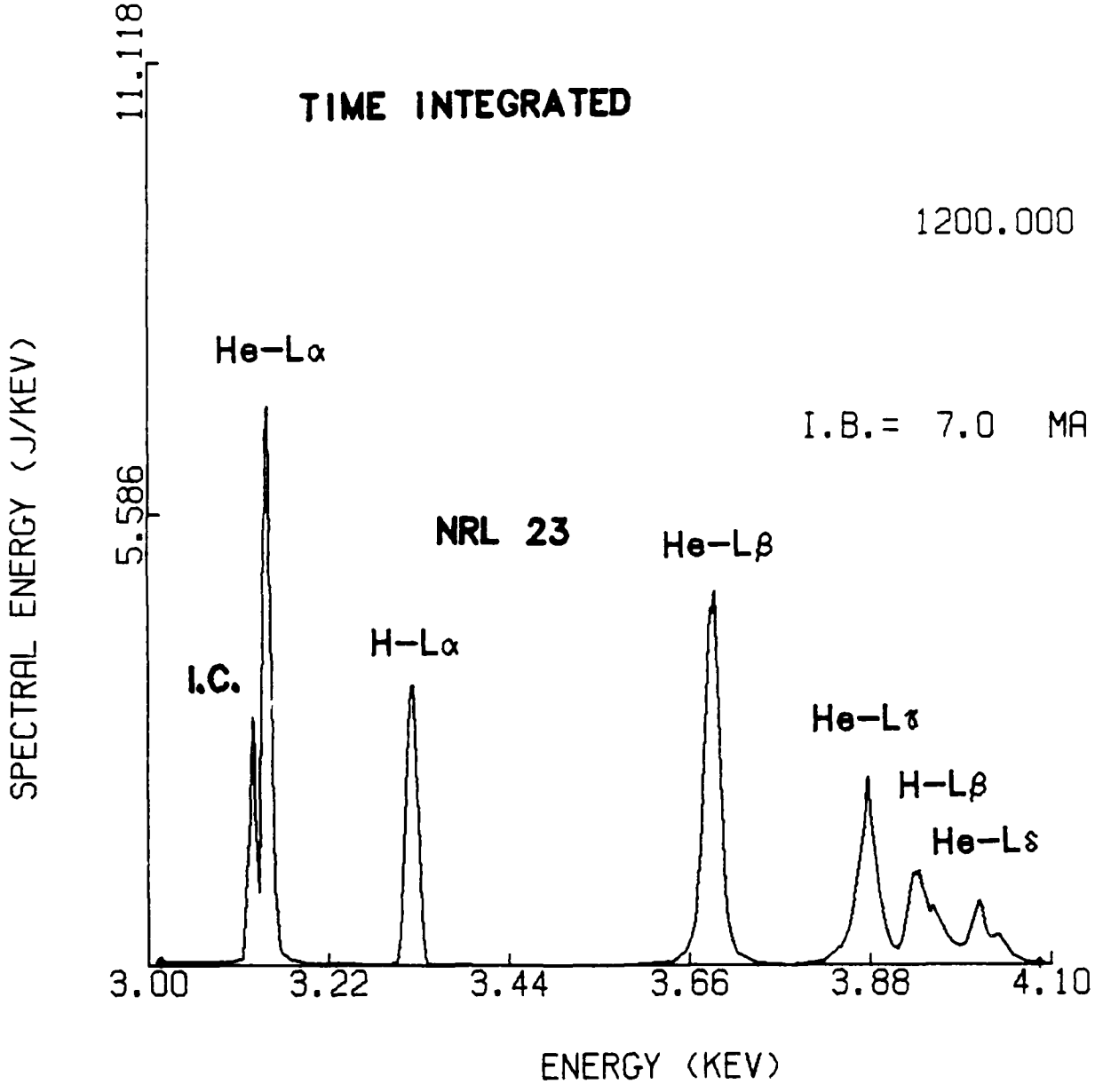


Fig. 30 Time integrated spectrum, including source broadening for NRL 23.

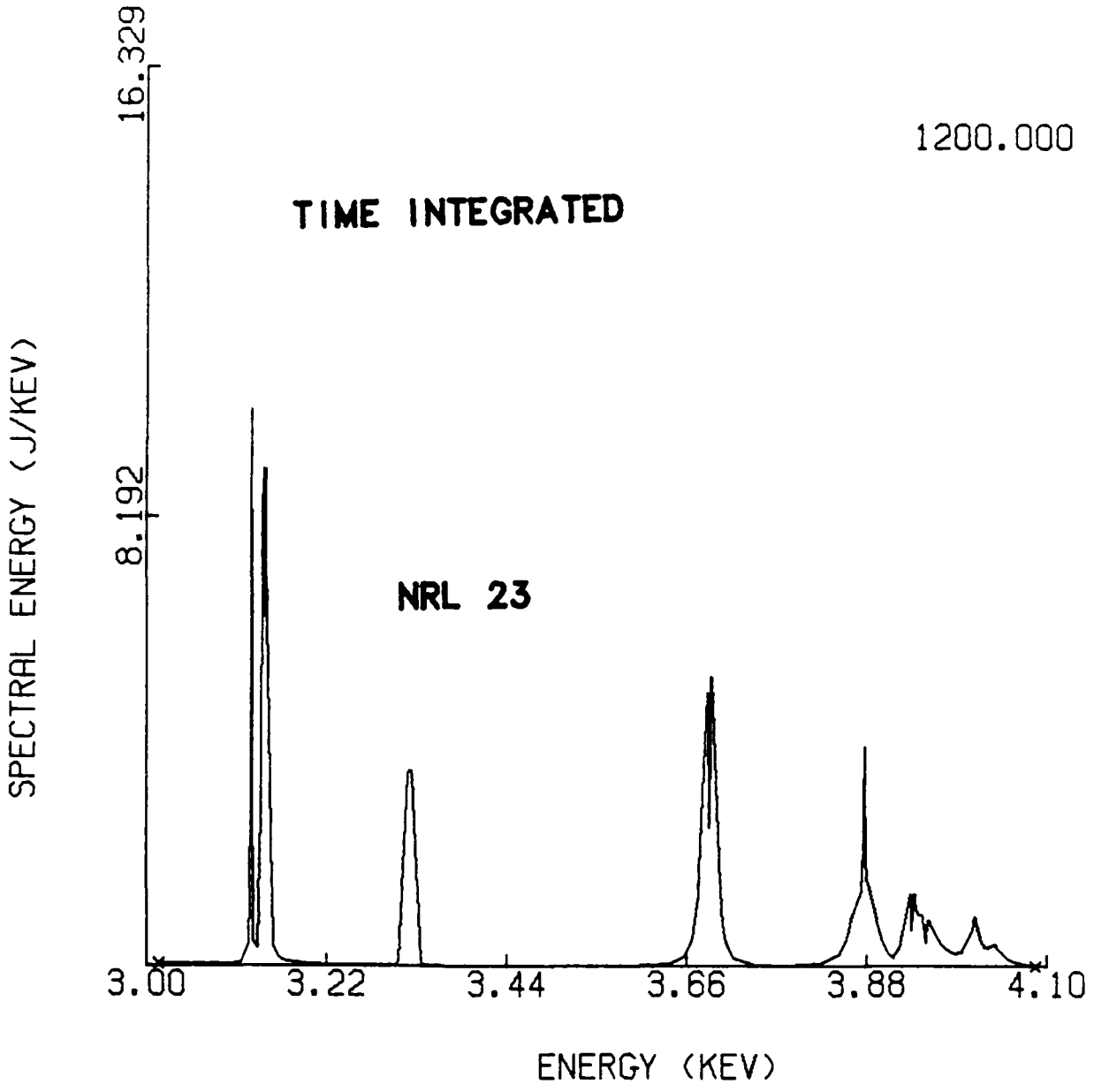


Fig. 31 Time integrated spectrum, not including source broadening for NRL 23.

861.458

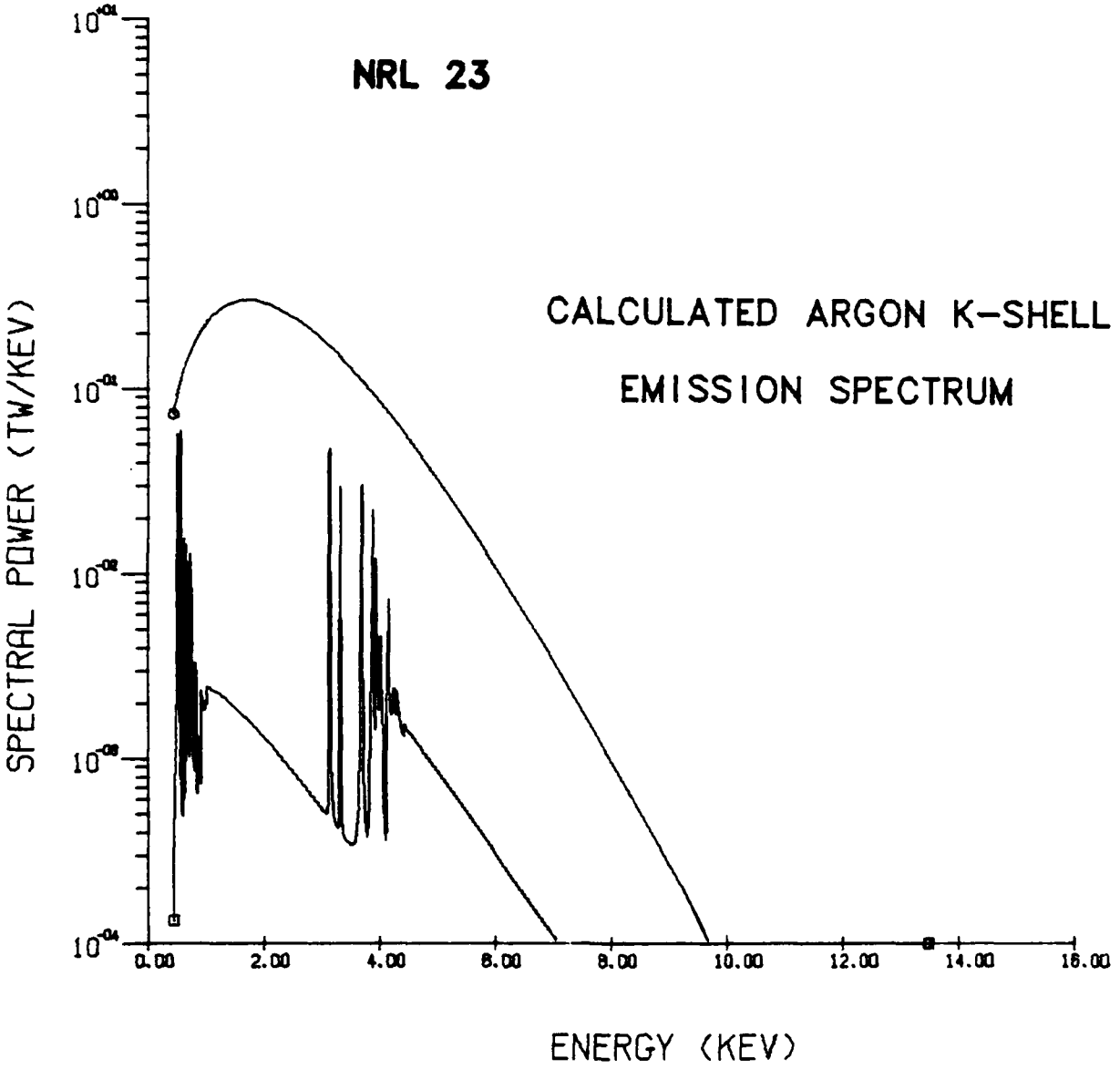


Fig. 32 Broadband spectrum for NRL 23 for the time of peak emittion. Also plotted is the blackbody spectrum corresponding to the temperature of the outside cell.

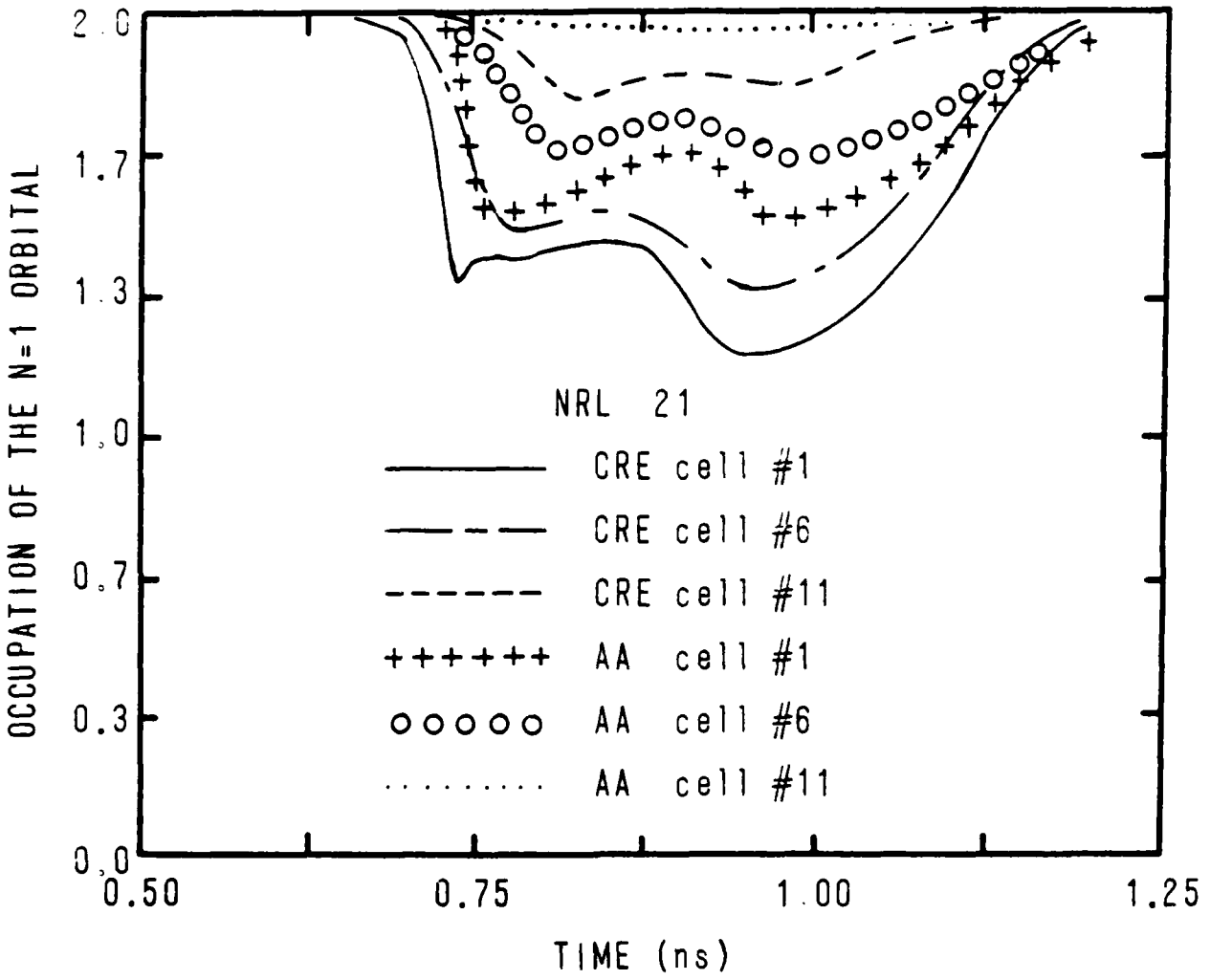


Fig. 33 Occupation of the n = 1 orbital vs time for NRL 21. The lines correspond to the values calculated by the Collisional-Radiative model, the points to values calculated by the Averge Atom model.

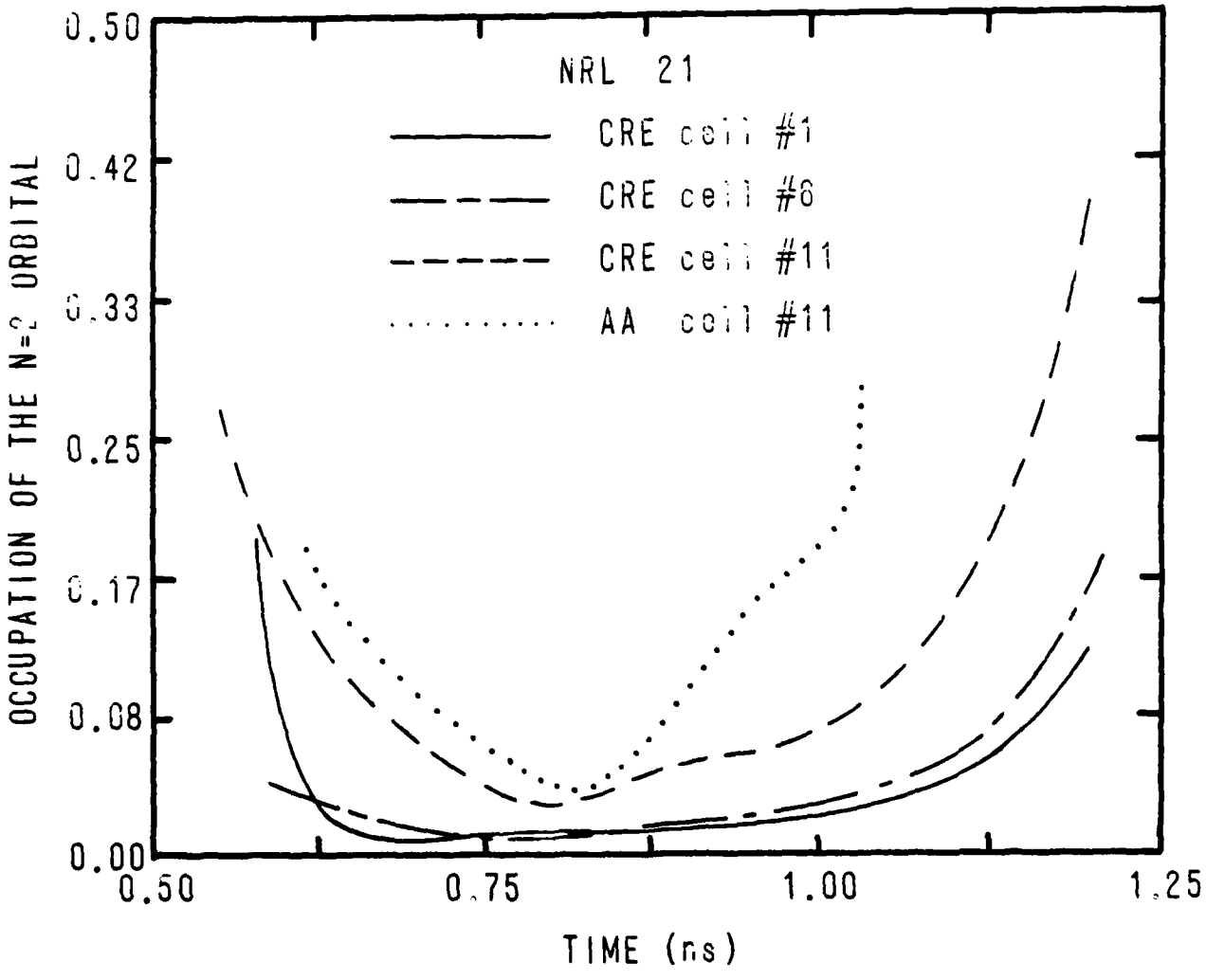


Fig. 34 Occupation of the n = 2 orbital vs time, for NRL 21. The lines correspond to the values calculated by the Collisional-Radiative model, the points to values calculated by the Average Atom model.

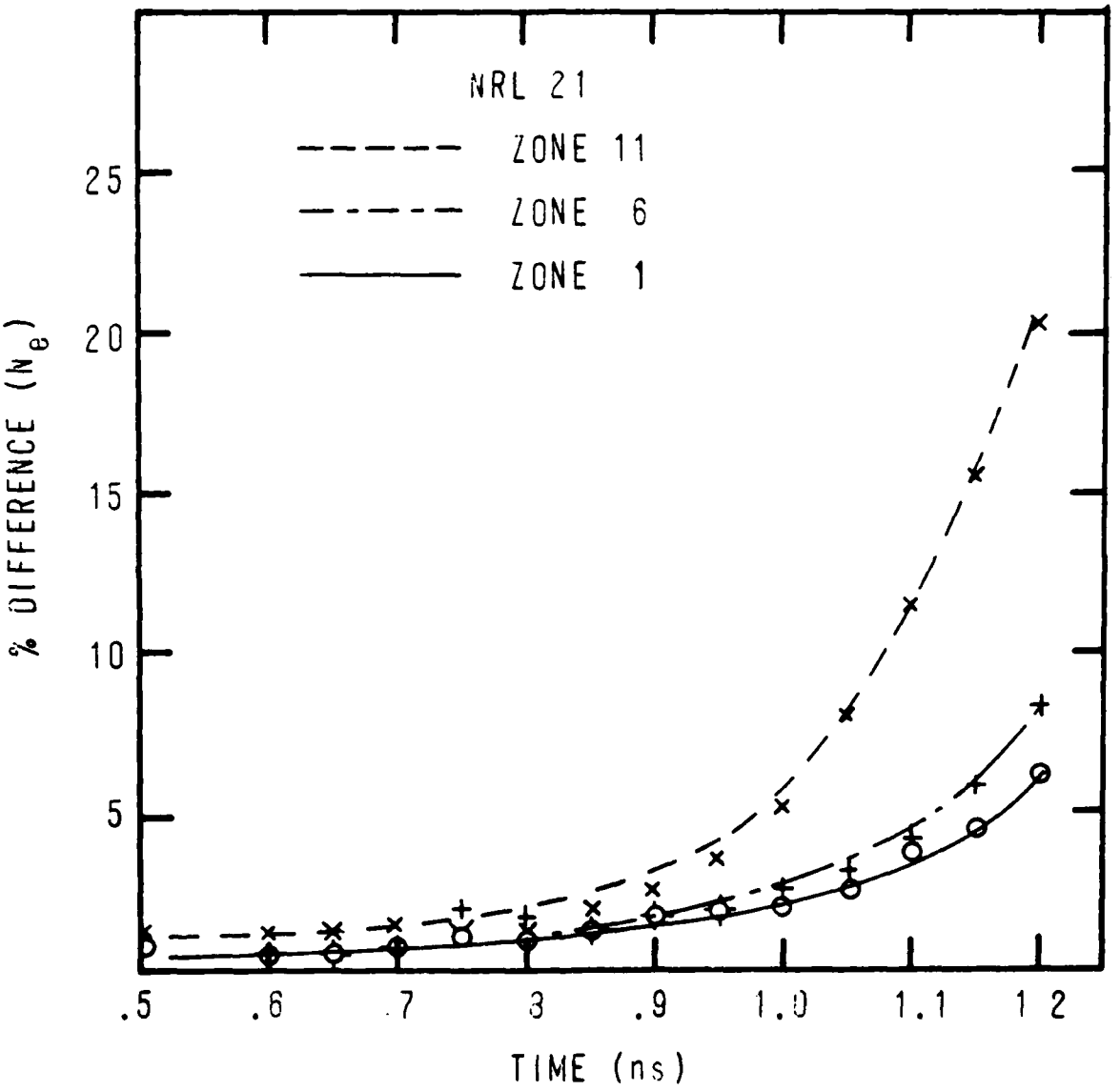


Fig. 35 Difference in the (Argon contribution to the) electron number density, for NRL 21, as calculated by the Collisional-Radiative and Average Atom models.

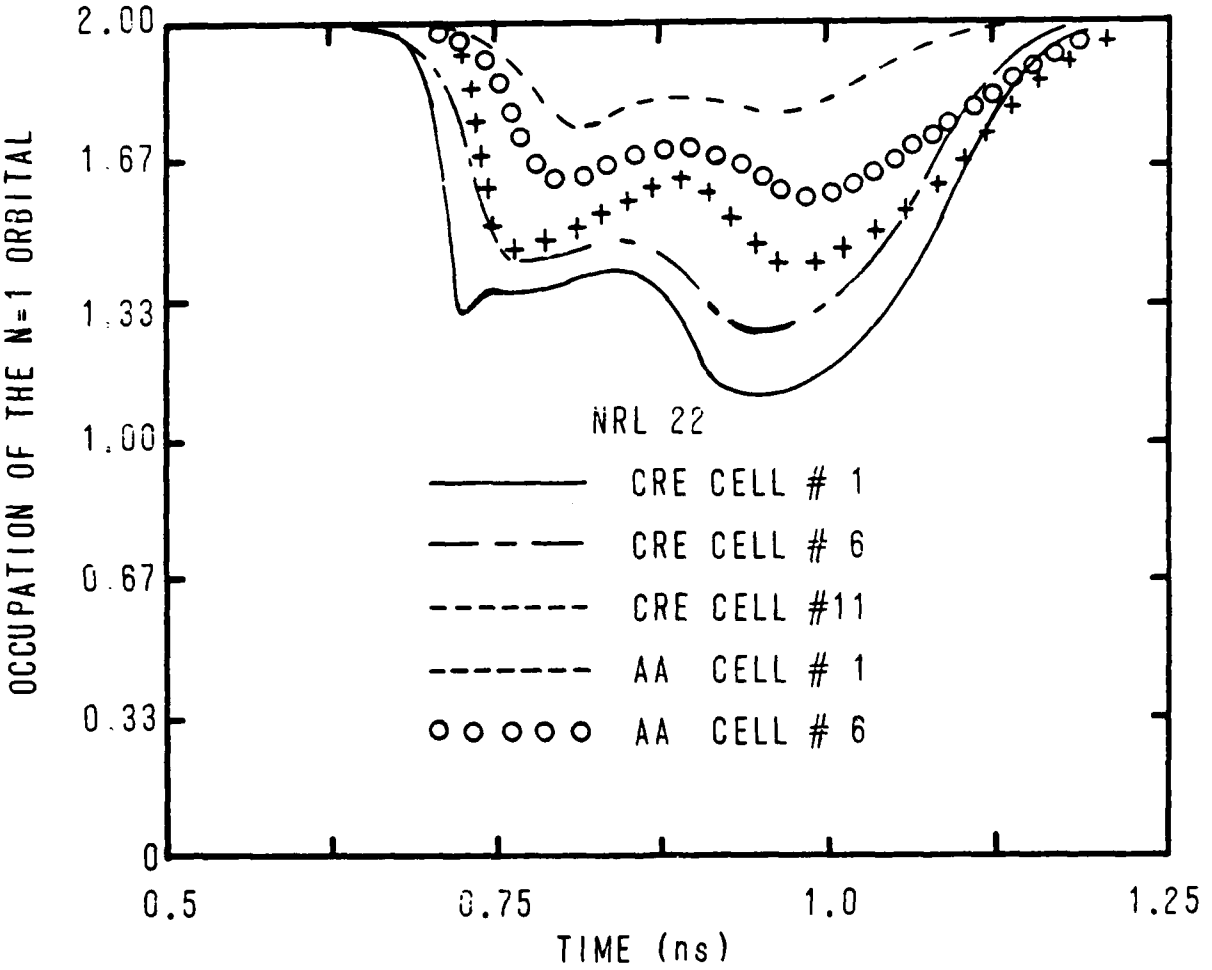


Fig. 36 Occupation of the n = 1 orbital vs time, for NRL 22. The lines correspond to the values calculated by the Collisional-Radiative model, the points to values calculated by the Average Atom model.

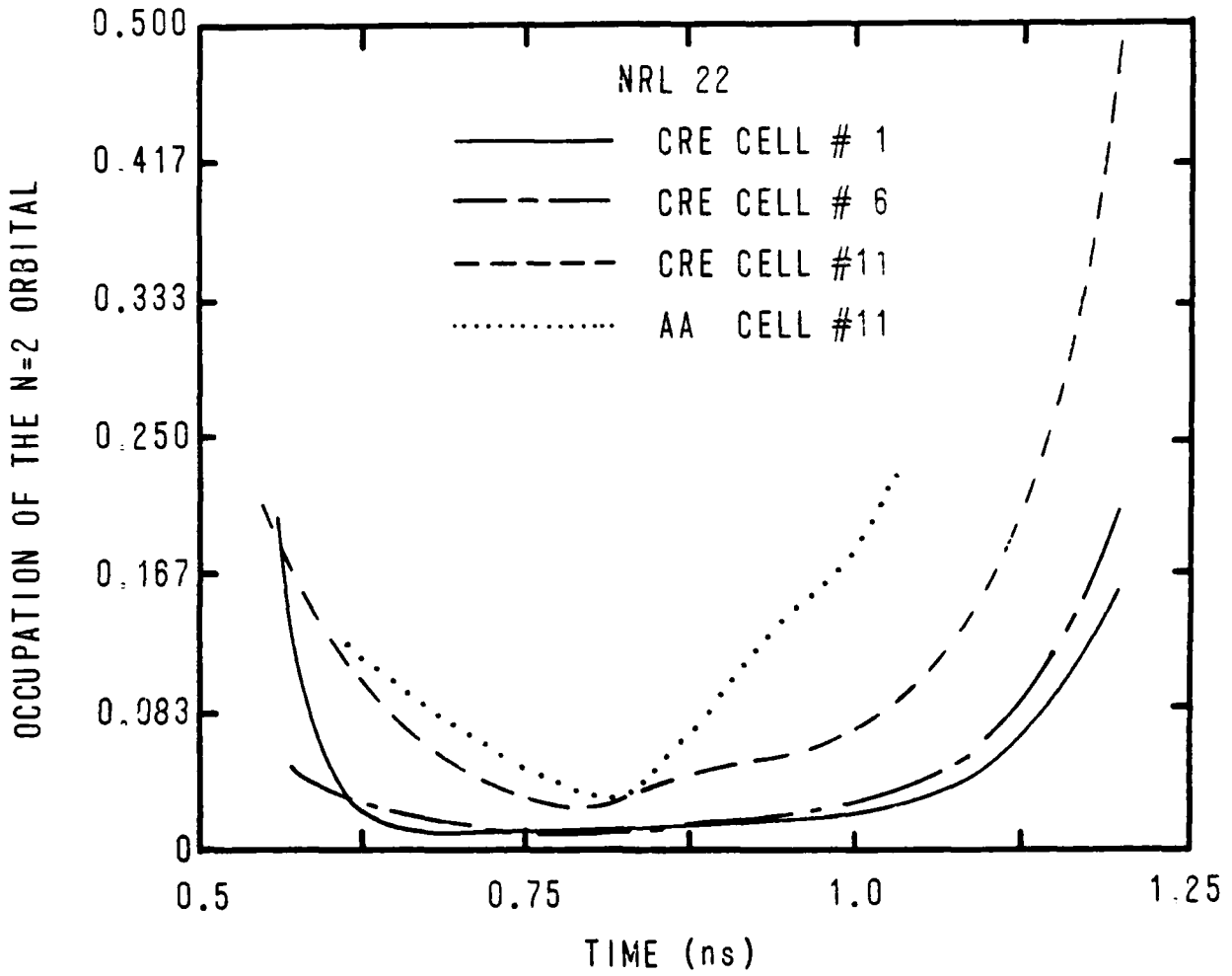


Fig. 37 Occupation of the n = 2 orbital vs time, for NRL 22. The lines correspond to the values calculated by the Collisional-Radiative model, the points to values calculated by the Average Atom model.

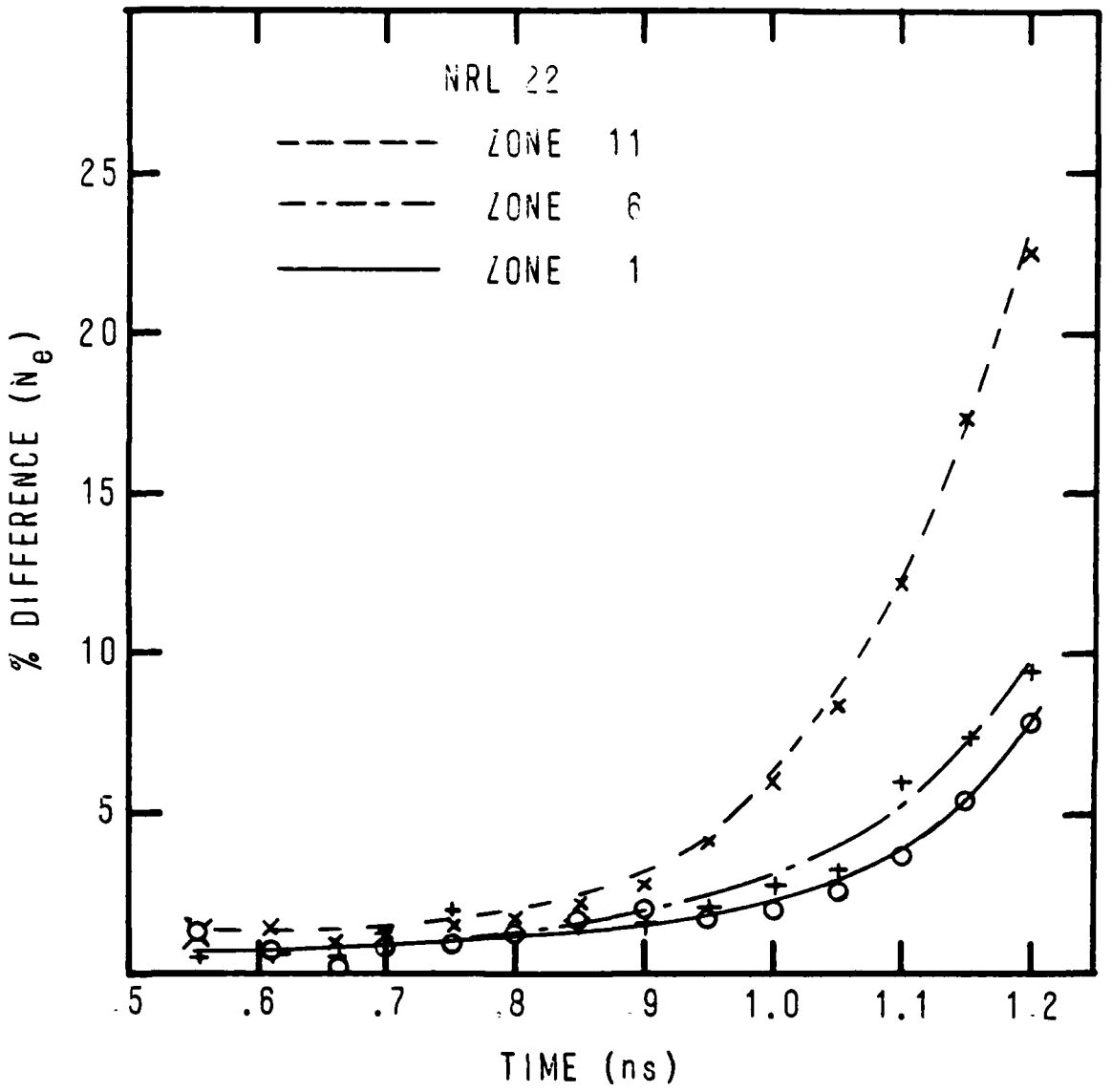


Fig. 38 Difference in the (Argon contribution to the) electron number density, for NRL 22, as calculated by the Collisional-Radiative and Average Atom models.

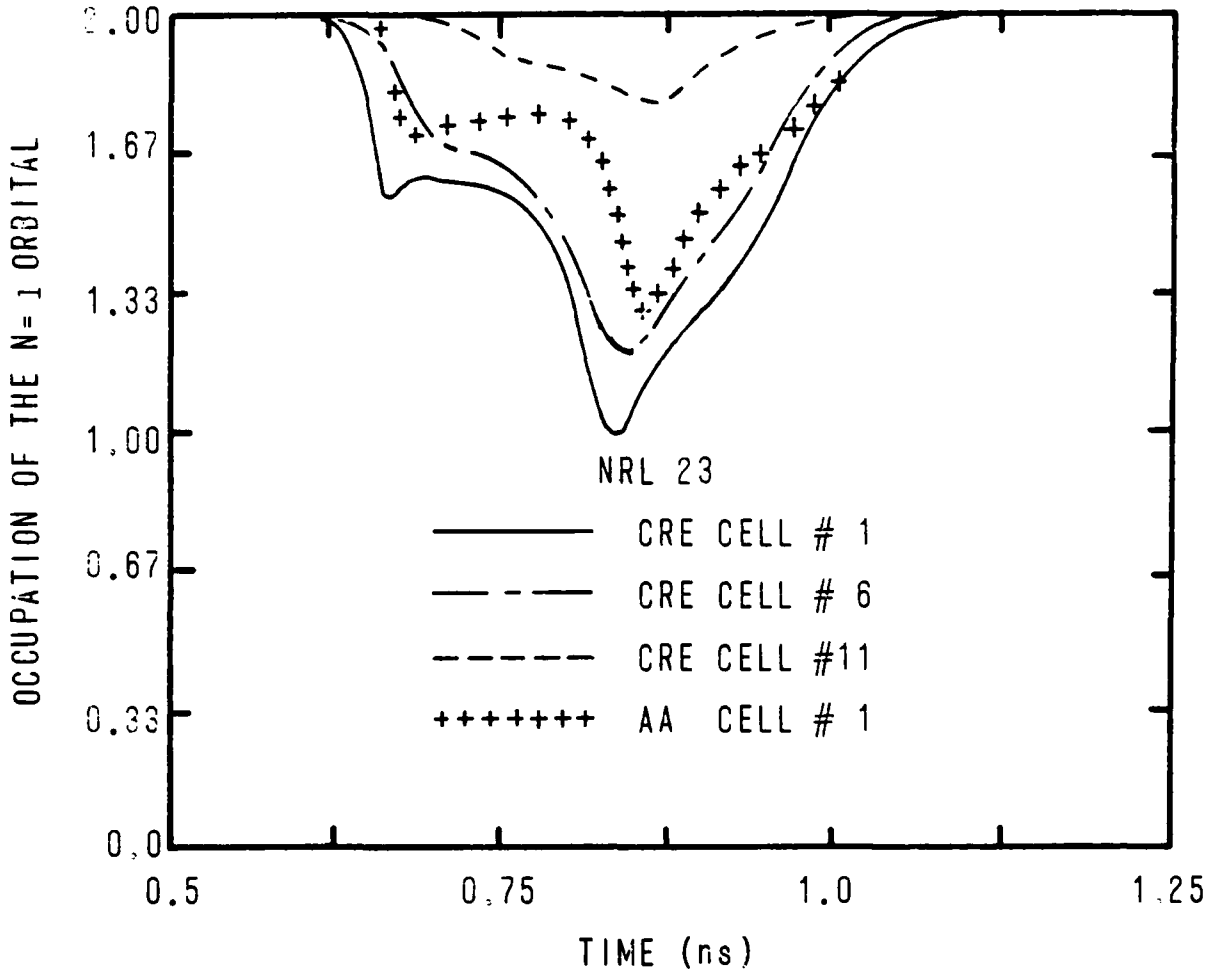


Fig. 39 Occupation of the n = 1 orbital time for NRL 23. The lines correspond to the values calculated by the Collisional-Radiative model, the points to values calculated by the Average Atom model.

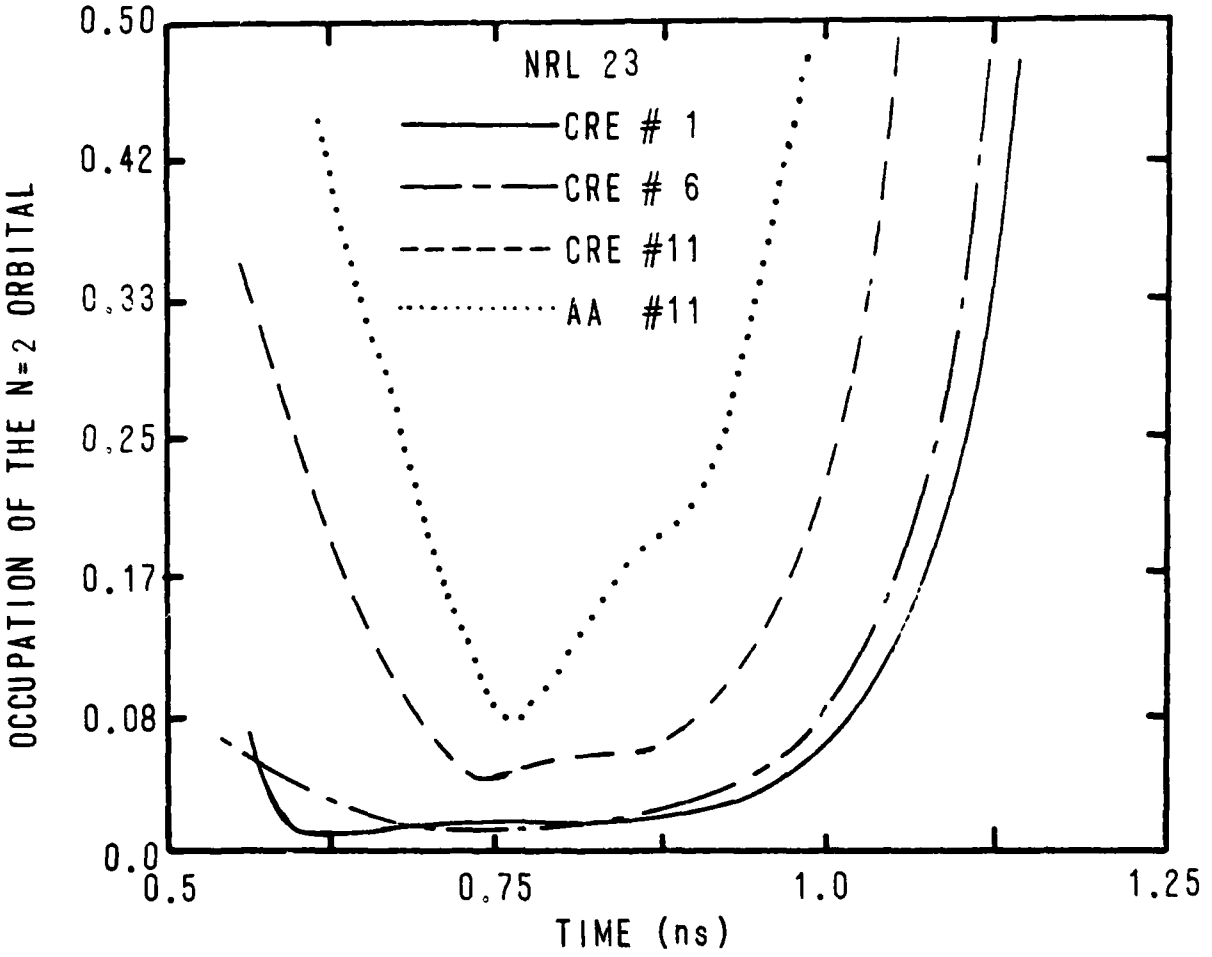


Fig. 40 Occupation of the n = 2 orbital vs time, for NRL 23. The lines correspond to the values calculated by the Collisional-Radiative model, the points to values calculated by the Average Atom Model.

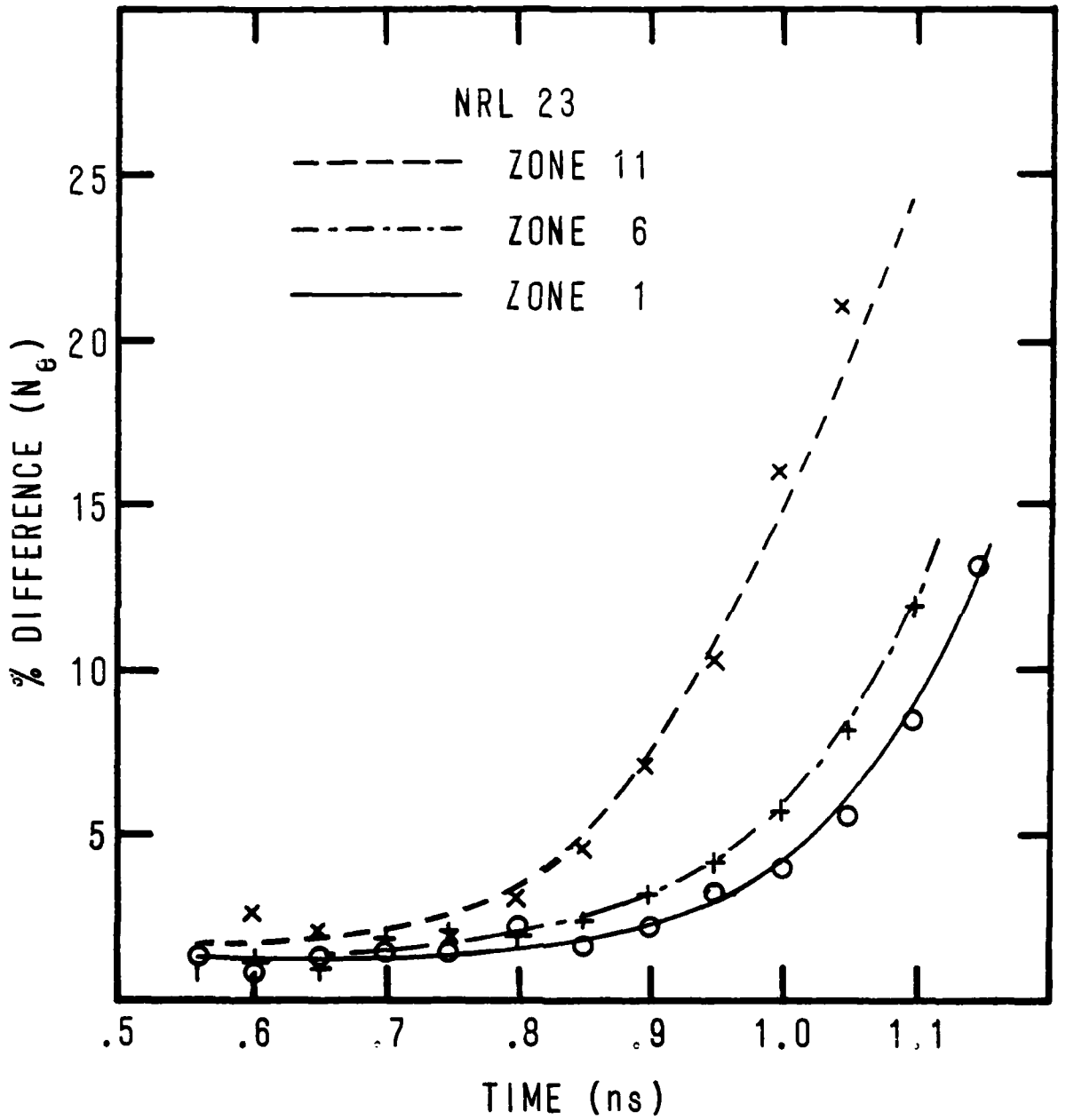


Fig. 41 Difference in the (Argon contribution to the) electron number density, for NRL 23, as calculated by the Collisional-Radiative and Average Atom models.

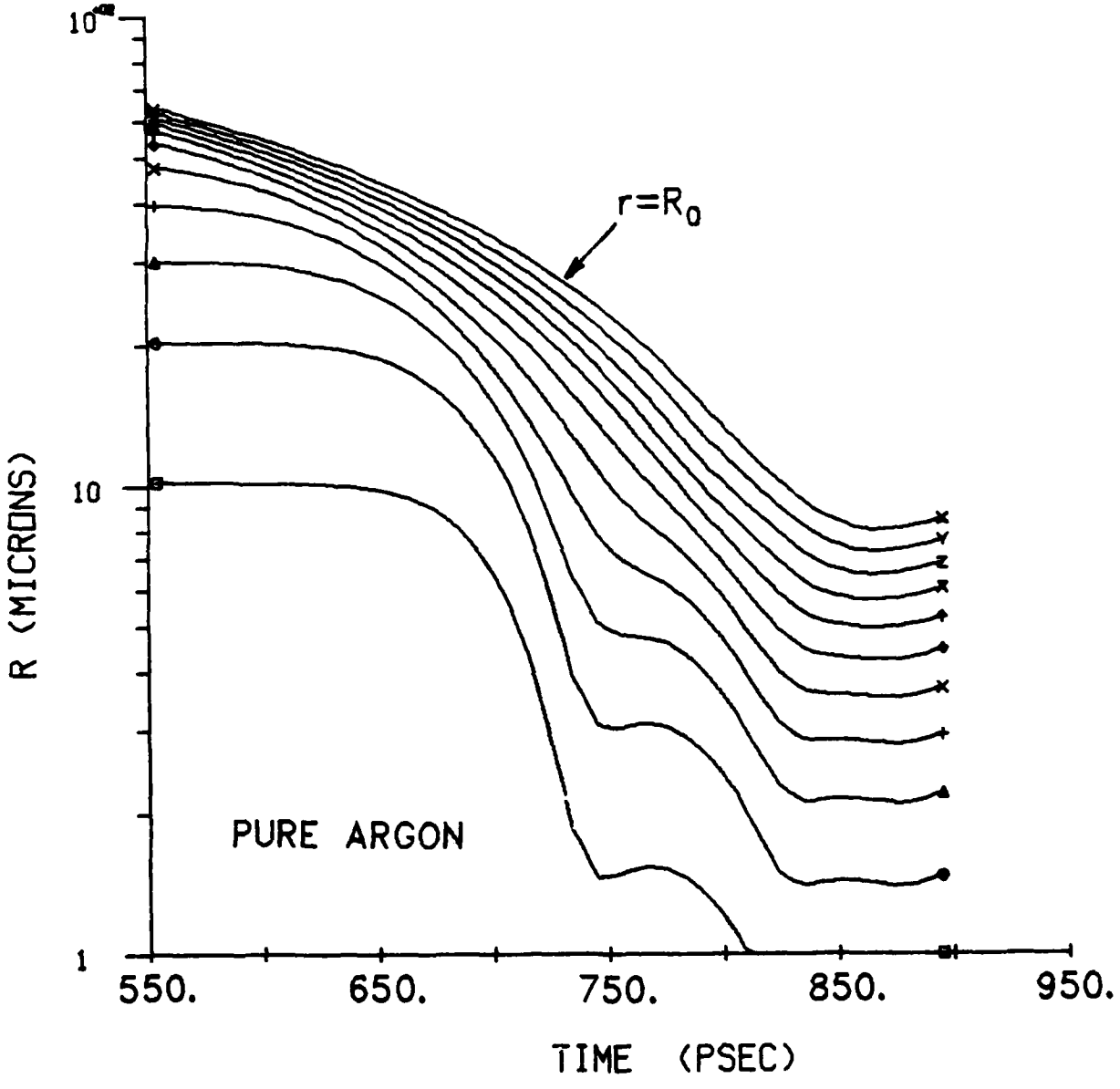


Fig. 42 Radius of cell centers vs time for pure argon LASNEX simulation.

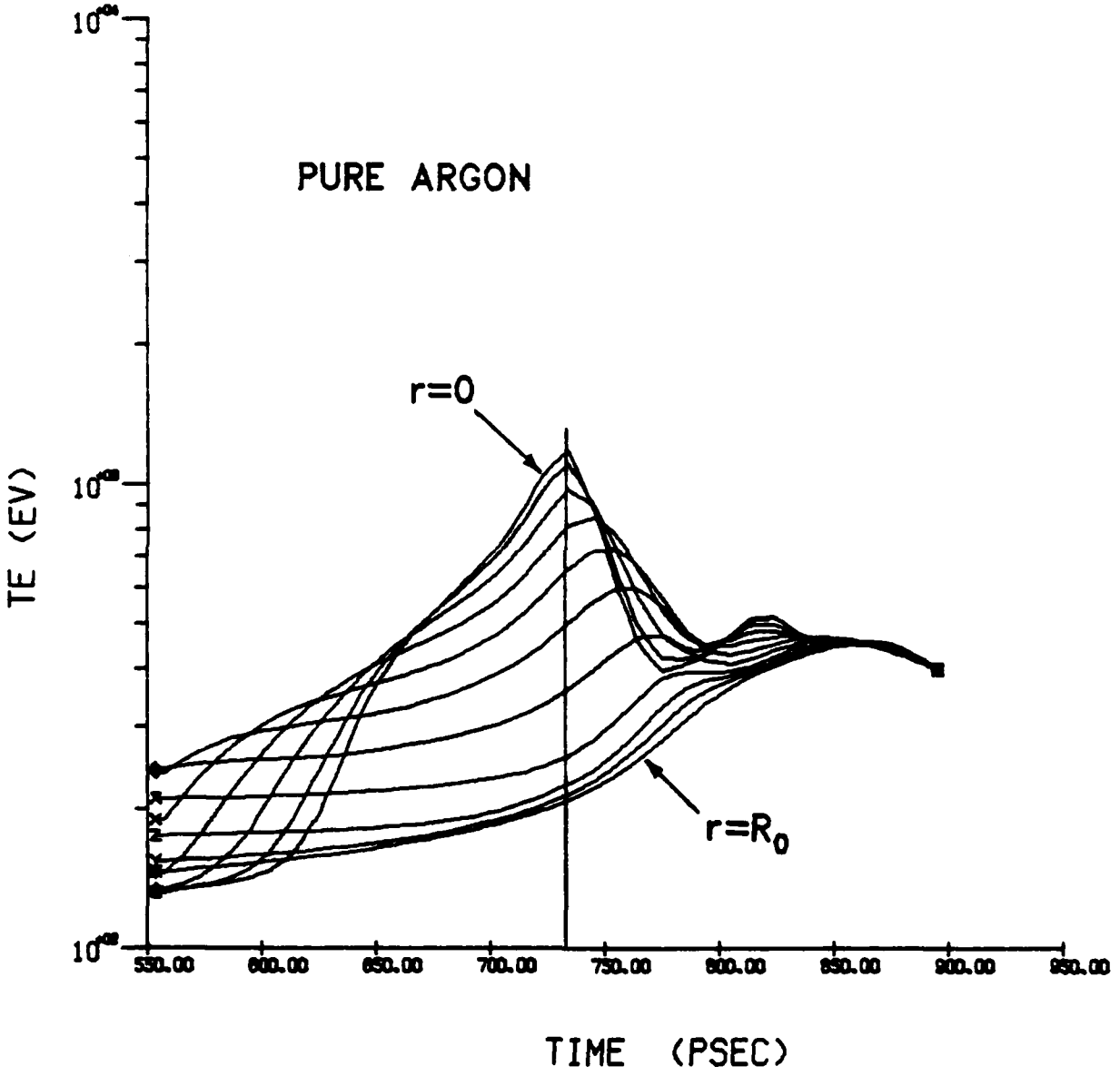


Fig. 43 Electron temperature vs time for pure argon LASNEX simulation.

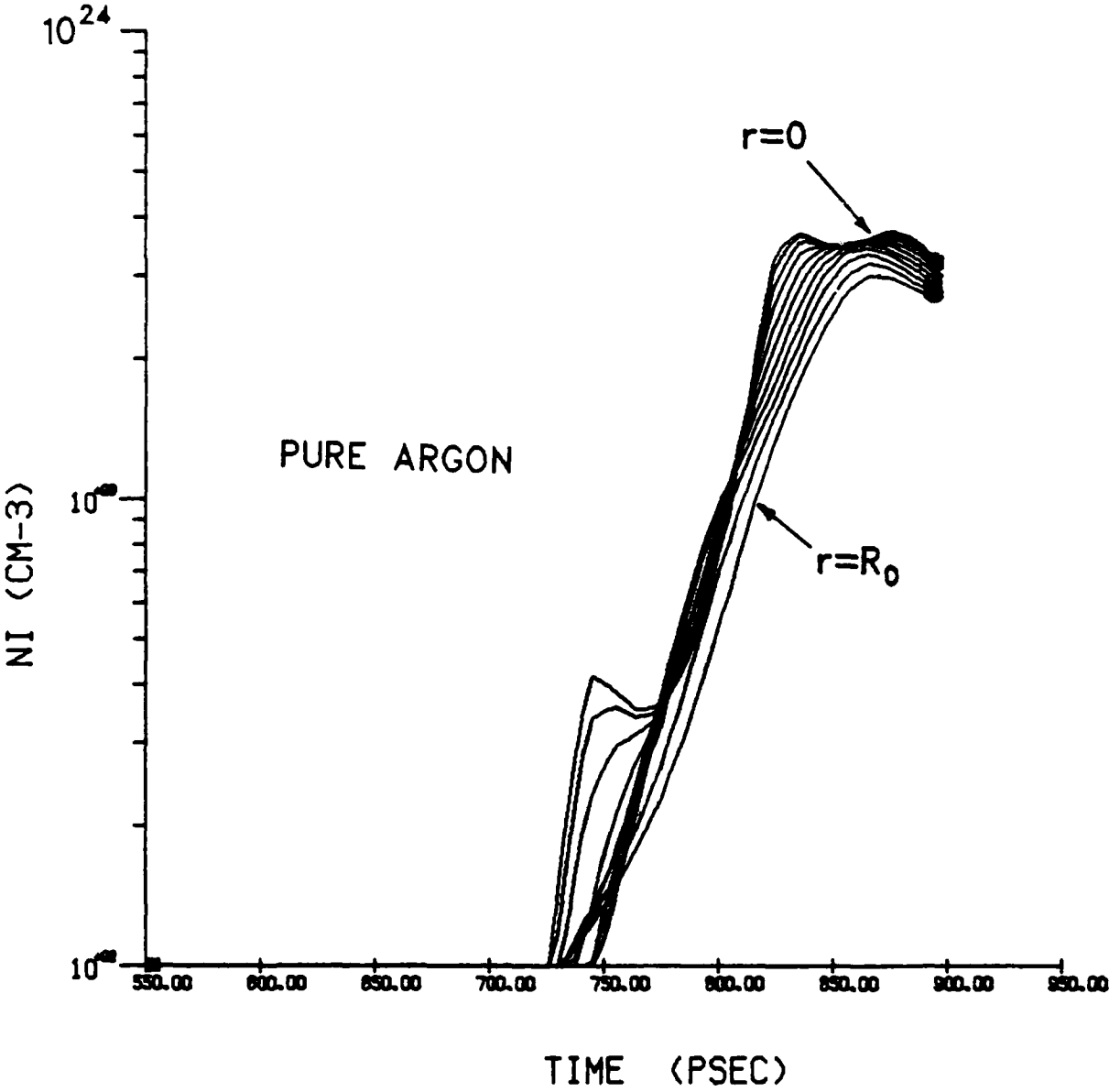


Fig. 44 Ion number density vs time for pure argon LASNEX simulation.

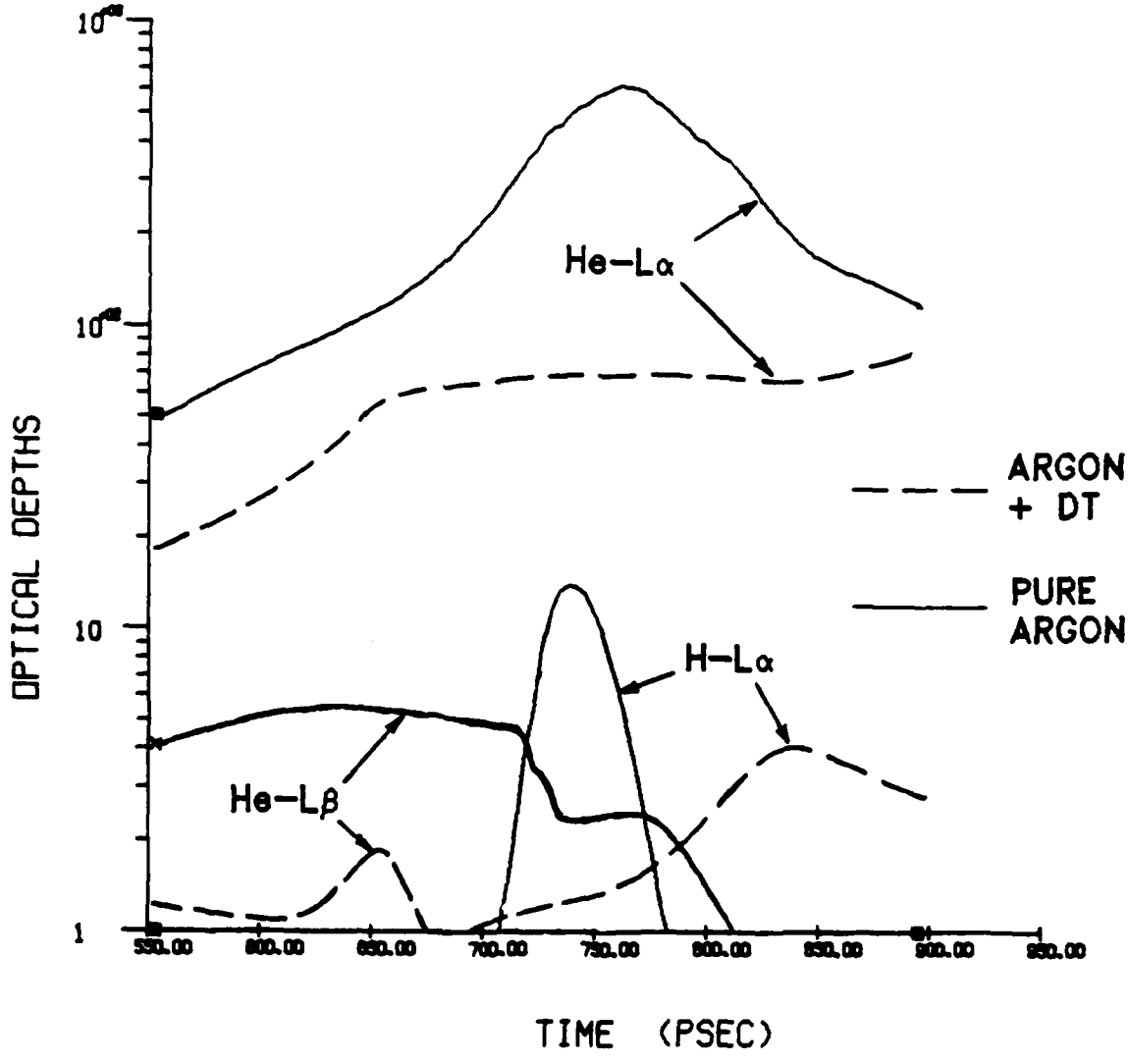


Fig. 45 Line opacities vs time for the pure argon calculation.

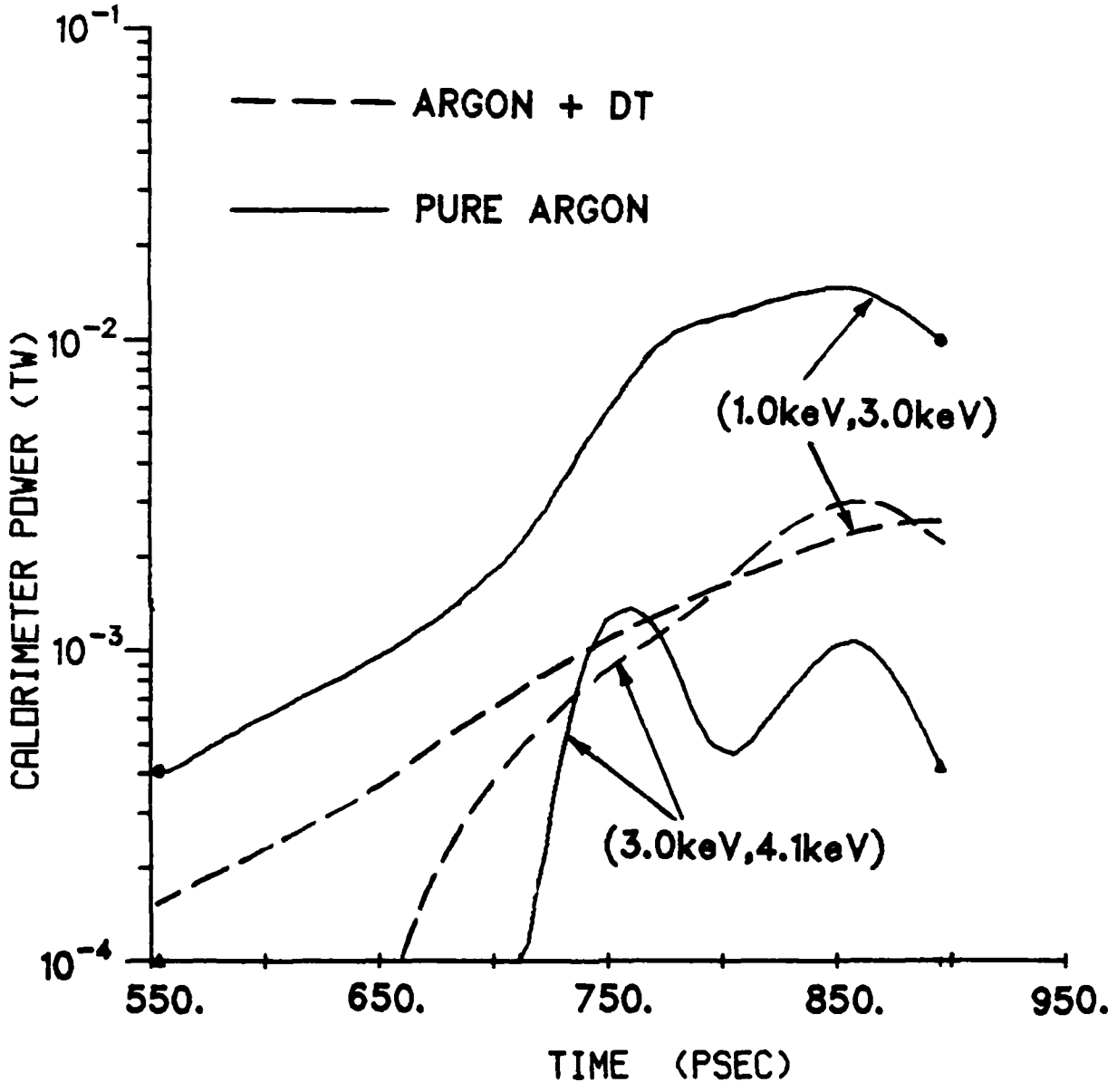


Fig. 46 Radiative energy in the 1-3 keV and 3-4 keV bands. Comparison between the pure argon case and NRL 23.

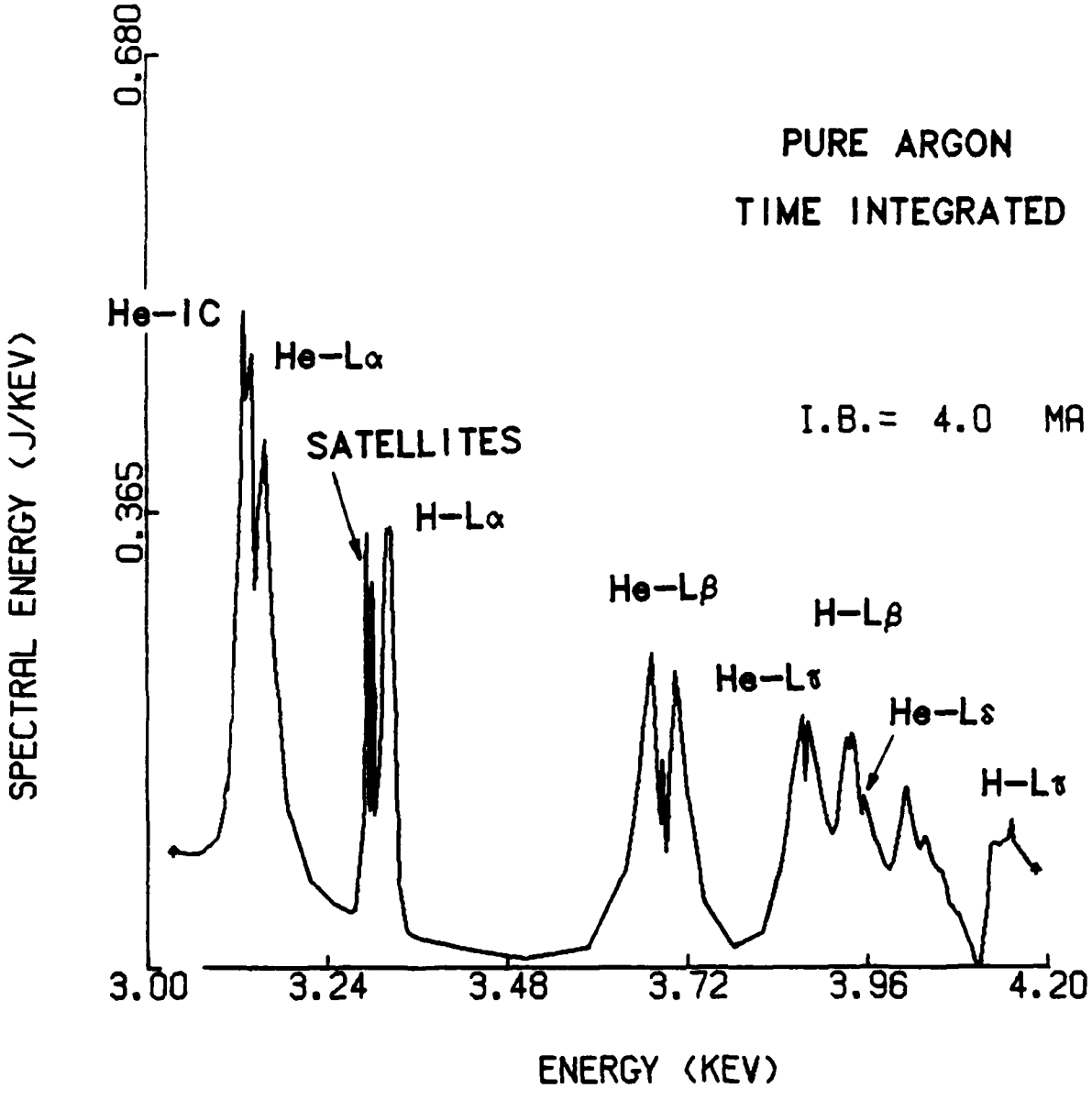


Fig. 47 Time integrated spectrum for the pure argon calculation.

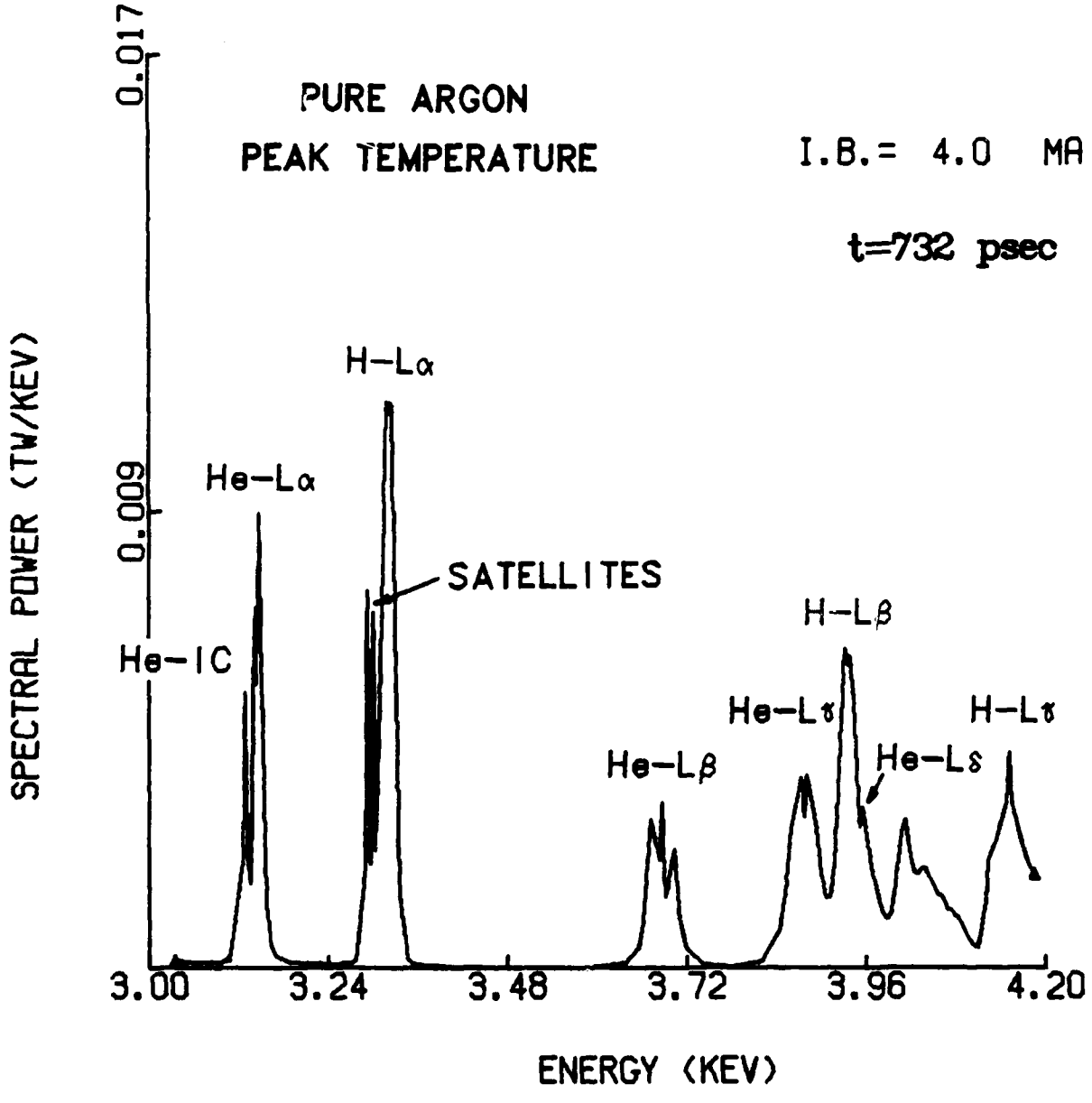


Fig. 48 Spectrum at 730 psec from the pure argon calculation.

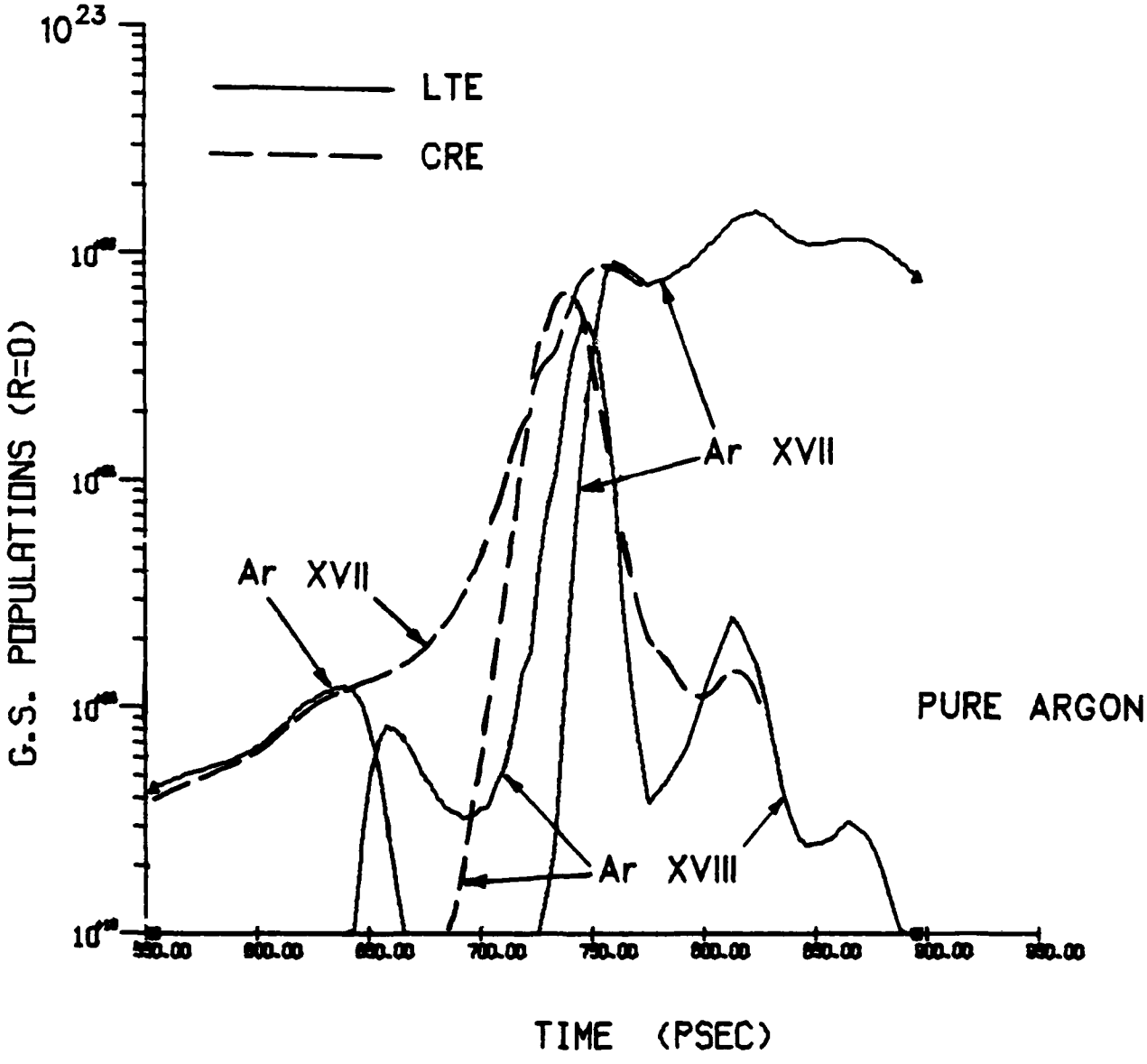


Fig. 49 Comparison of CRE to LTE ground state number densities vs time for the pure argon calculation in the inner cell.

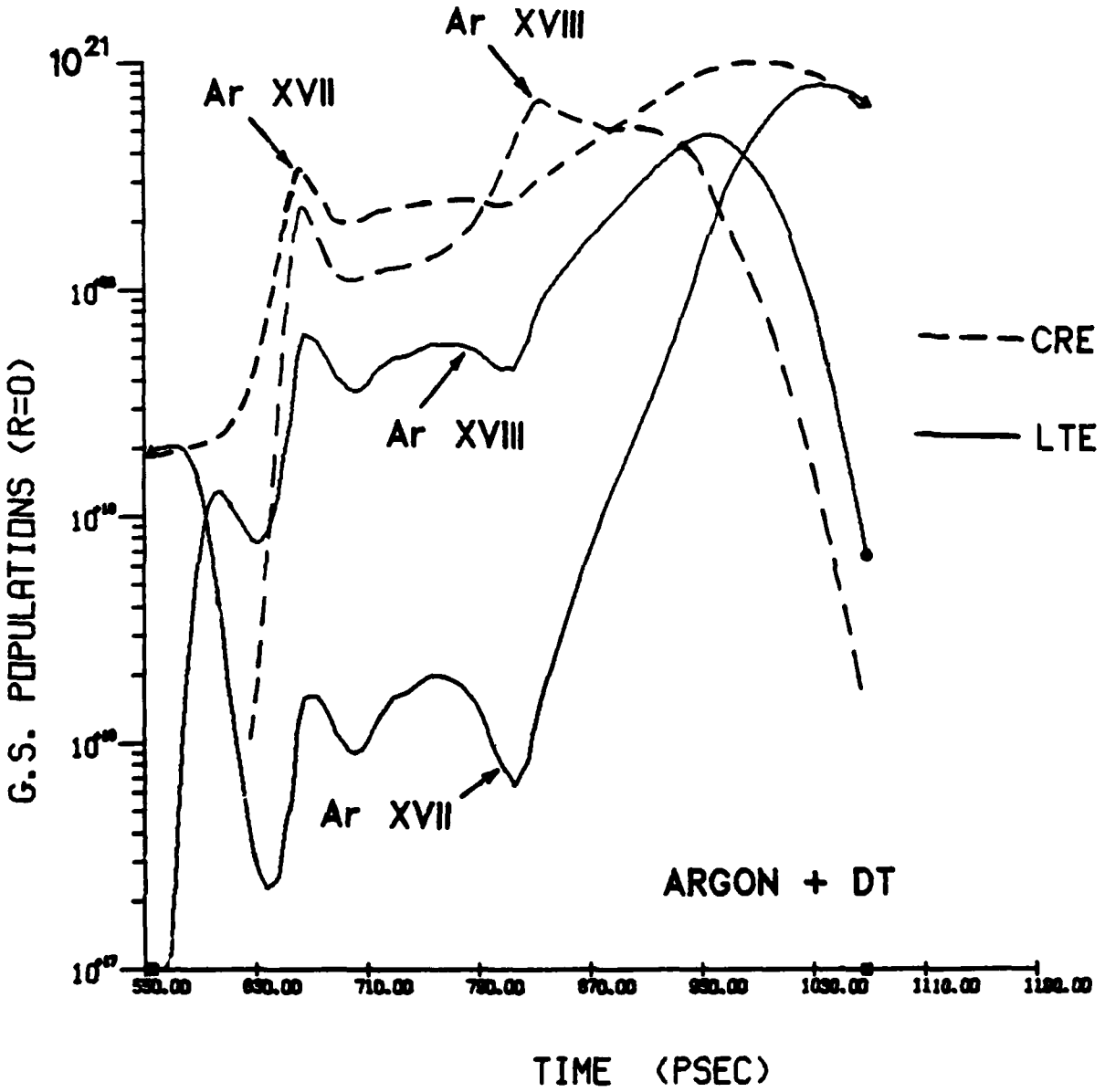


Fig. 50 Comparison of CRE to LTE ground state number densities vs time for NRL 23 in the inner cell.

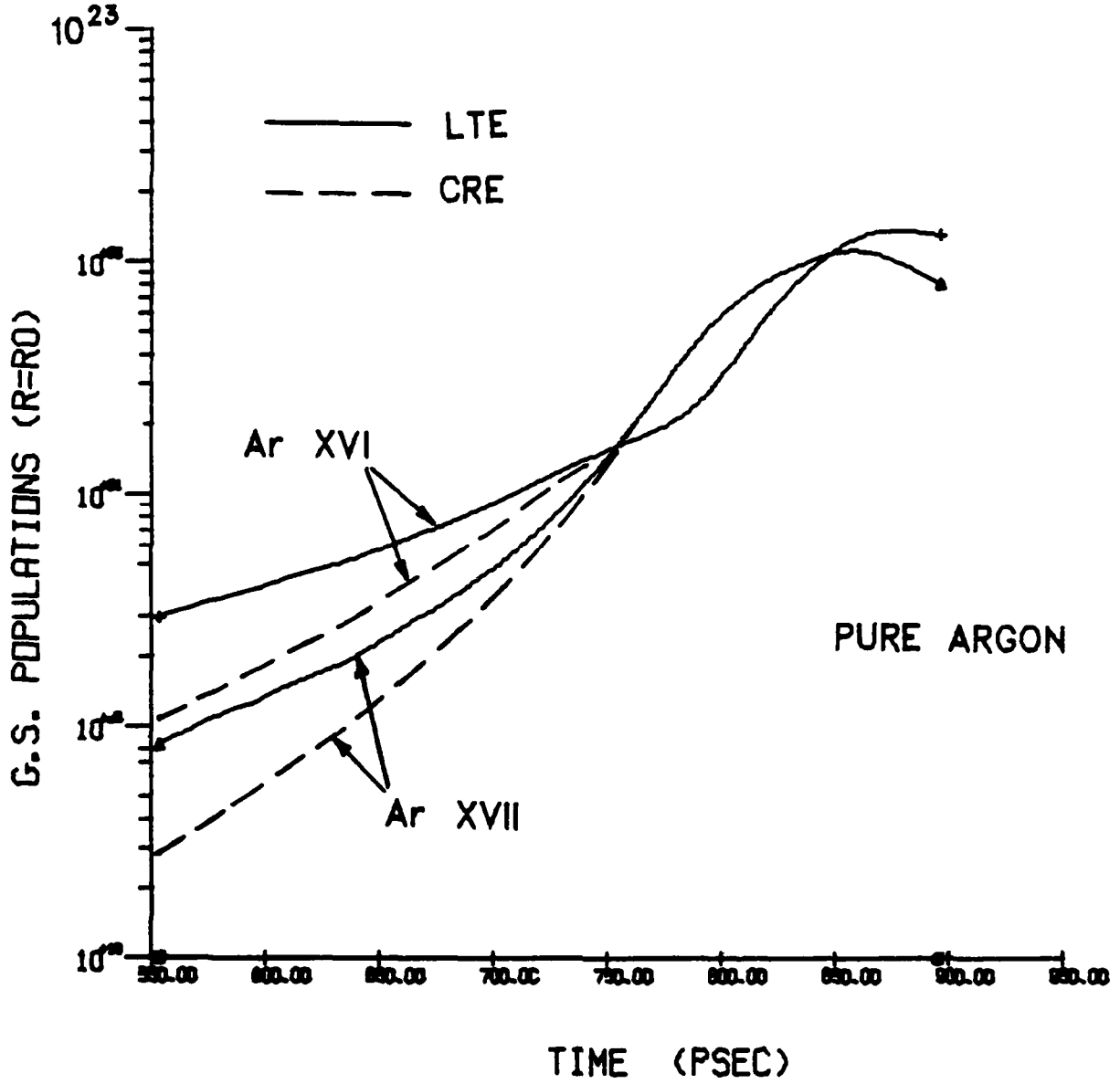


Fig. 51 Comparison of CRE to LTE ground state number densities vs time for the pure argon calculation in the outer cell.

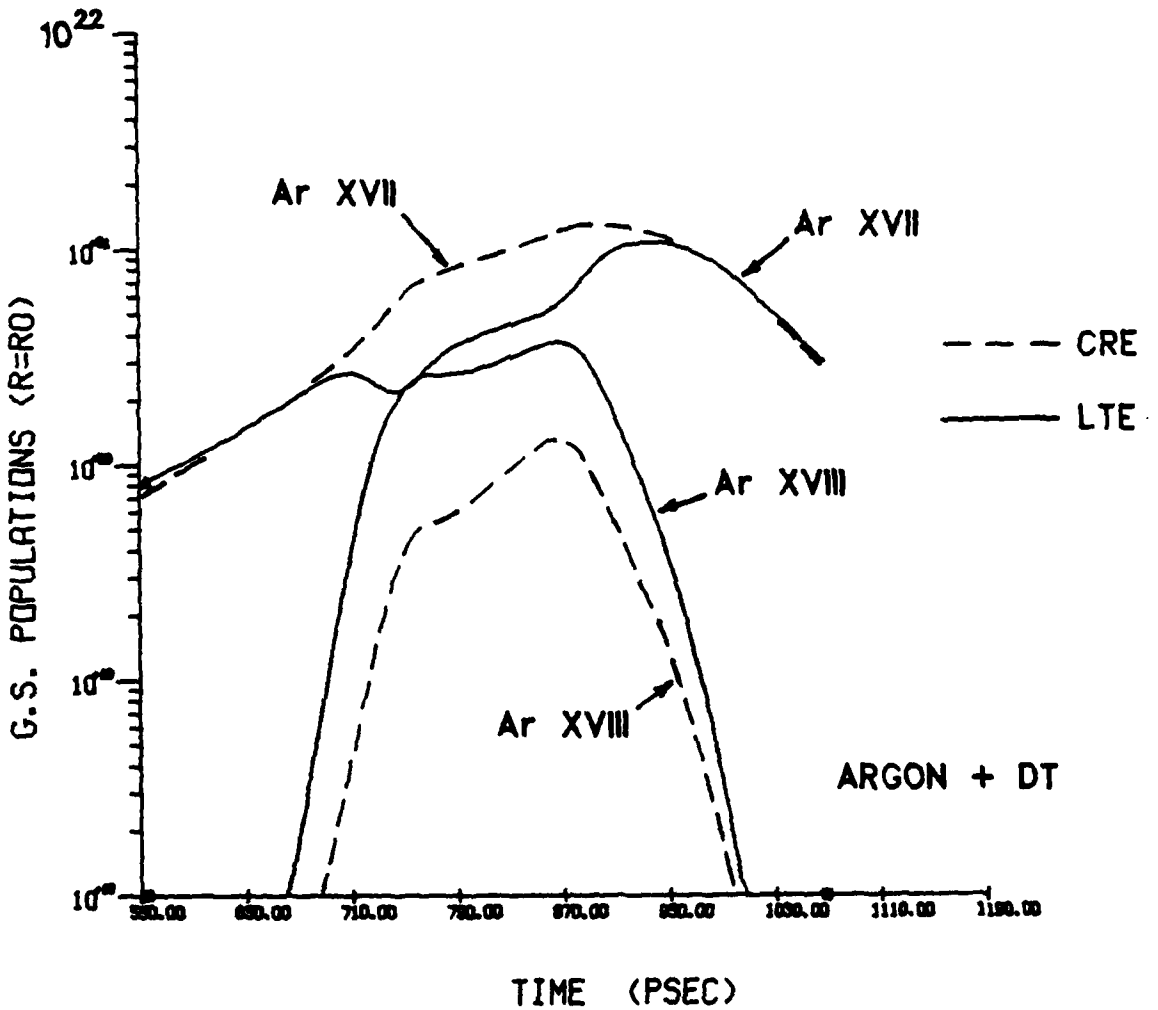


Fig. 52 Comparison of CRE to LTE ground state number densities versus time for NRL 23 in the outer cell.


ATE
ME